ROYAL SOCIETY OF CHEMISTRY

REVIEW

Check for updates

Challenges and design opportunities for high-energy-density aqueous zinc-ion batteries: from electrochemically active to functional components

Yubin Lee, Sangyeop Lee and Soojin Park [ID] *

Aqueous zinc-ion batteries (AZIBs) have garnered increasing attention as next-generation rechargeable batteries owing to their inherent safety, environmental friendliness, and cost-effectiveness, which was not fully provided by conventional lithium-ion batteries (LIBs). However, establishing AZIBs as viable alternatives to LIBs requires substantial improvements in energy density. While cathode design has traditionally been regarded as a primary factor, system-level enhancement requires not only increased operating voltage and charge storage capacity but also a reduction in electrochemically inactive components. In this review, we provide a comprehensive discussion of multi-faceted strategies for maximizing the energy density of AZIBs. From the cathode perspective, increasing areal capacity through high-mass-loading electrodes and developing cathode materials with both high voltage and large capacity are essential. Unfortunately, aqueous electrolytes remain constrained by the narrow electrochemical stability window, which prompts strategies to suppress water decomposition and enable high-voltage operation. On the anode side, metallic zinc (Zn) foil is typically employed and excess Zn is often required to ensure long-term stability, which further reduces practical energy density. Separators, despite being less emphasized, also play a significant role because conventional glass fiber separators are thick and heavy, impeding energy density optimization. Accordingly, developing advanced separators with reduced thickness and improved electrochemical properties becomes increasingly important. This review identifies key limitations that constrain the energy density of AZIBs and explores viable strategies and future design directions toward high-energy-density realization. We anticipate that a system-level perspective will offer valuable insight into the development of next-generation AZIBs and support their positioning as competitive alternatives to LIBs.

Broader context

Growing interest in environmentally benign and sustainable energy technologies has extended to the field of energy storage. However, conventional lithium-ion batteries (LIBs) face inherent limitations, and the exploration of alternative systems has become essential. Among them, aqueous zinc-ion batteries (AZIBs) have attracted considerable attention owing to their intrinsic safety, cost-effectiveness, and environmental compatibility. Despite these advantages, their relatively low energy density remains a critical obstacle to practical implementation. The insufficient energy density stems not only from cathode limitations but also from various system components, such as the anode, electrolyte, and separator. Therefore, improving energy density demands a holistic approach that goes beyond cathode optimization, incorporating strategies to minimize the negative-to-positive capacity ratio and reduce the fraction of electrochemically inactive constituents. In this context, we highlight recent progress in both material and system-level strategies for enhancing the energy density of AZIBs. Furthermore, by critically examining the limitations of each component, we aim to provide valuable insights into emerging opportunities. Consequently, continued advancement along these directions is expected to accelerate the practical realization of AZIBs for next-generation energy storage applications.

1. Introduction

In response to global concerns regarding environmental degradation, global momentum has been building toward carbon neutrality targets that aim to achieve net-zero emissions

Department of Chemistry, Pohang University of Science and Technology (POSTECH), 77 Cheongam-ro, Nam-gu, Pohang 37673, Republic of Korea.
E-mail: soojin.park@postech.ac.kr

between 2050 and 2060.[1,2] Realizing carbon neutrality requires the widespread adoption of renewable energy sources such as solar and wind power, but their intermittent and inherently variable nature imposes a fundamental constraint on maintaining a stable and continuous energy supply.[3,4] As a result, the development of grid-scale energy storage systems is essential for the reliable integration of renewable energy into modern power infrastructures.[5–7] Beyond grid applications, energy storage technologies also provide a crucial bridge to

other sectors critical for decarbonization. The electrification of transportation, which accounts for another foundational pillar in efforts to combat climate change, necessitates energy storage systems that can replace internal combustion engines with dependable and efficient alternatives.[8–10] In this context, rechargeable batteries that efficiently store energy and deliver it on demand are regarded as indispensable for realizing a sustainable future.

Lithium-ion batteries (LIBs) have emerged as the prevailing rechargeable battery across a broad range of applications due to their high energy density, low self-discharge rate, and lightweight design.[11–13] However, key components in LIBs face challenges stemming from low crustal abundance and geopolitical issues, and the accelerating deployment of LIBs has intensified concerns regarding raw material depletion and long-term supply security.[14] Moreover, the extreme sensitivity of LIBs to moisture requires dry-room environments, which substantially increase manufacturing expenditure.[15,16] The use of flammable organic electrolytes also introduces inherent safety hazards and exacerbates environmental concerns.[17,18] Taken together, these limitations have collectively prompted growing interest in the development of safe and sustainable alternatives to LIBs. Aqueous zinc-ion batteries (AZIBs) have gained considerable attention as promising post-LIB candidates, as they utilize Earth-abundant and cost-effective zinc (Zn) metal as the anode and employ intrinsically safe water-based electrolytes.[19–23] In addition, AZIBs benefit from stable and accessible raw material supply chains, contributing to lower system-level costs.[24,25] For instance, the market price of MnO_2 cathode material for AZIBs (~2.3 USD per kg) is more than an order of magnitude lower than that of the widely adopted lithium nickel cobalt manganese oxide ($LiNi_{0.6}Co_{0.2}Mn_{0.2}O_2$, NCM622) cathode used in LIBs (~25 USD per kg).[26] Furthermore, Zn is extensively utilized in industrial fields and is supported by mature recycling infrastructures, providing greater resilience to resource volatility compared with lithium-based systems.[27] Electrochemically, Zn anodes exhibit a low redox potential (−0.76 V *vs.* standard hydrogen electrode) and enable multivalent charge transfer, leading to a high volumetric capacity of 5855 mAh cm^{-3}.[28,29] Moreover, water-based electrolytes enhance the environmental compatibility of AZIBs while offering higher ionic conductivity (up to 1 S cm^{-1}) than organic solvent-based electrolytes (<10 mS cm^{-1}) and facilitating fabrication under ambient conditions, which further underscores the practical advantages of AZIBs.[30–32]

However, AZIBs still face several critical challenges that should be addressed to enable practical deployment. One of the key limitations lies in the low reversibility of the Zn anode and the chemical/electrochemical instability of the aqueous electrolyte.[33,34] Ideally, Zn should dissolve and deposit reversibly across the electrode surface during cycling, but in practice, nonuniform electric field distribution and ionic concentration gradients often promote localized metal growth, resulting in the formation of Zn dendrites.[35,36] The induced dendritic morphology can cause internal short circuits and intensify parasitic reactions at the interface between the Zn anode and the

electrolyte, thereby degrading electrochemical performance.[37,38] Additionally, mild acidic aqueous electrolytes (pH 4–6) can accelerate Zn corrosion, while other detrimental reactions, such as the hydrogen evolution reaction (HER) and the formation of insulating surface layers, further contribute to electrolyte depletion and electrode deterioration.[39–41] Consequently, these cumulative effects increase internal resistance and compromise long-term cycling stability, which poses an obstacle to the practical viability of AZIBs. However, these reversibility-related issues are not the sole factor limiting the commercial viability of AZIBs. In fact, overcoming the inherently low energy density of AZIB systems is equally or more important for ensuring their practical applicability. Furthermore, meeting energy density requirements necessitates advancements not only in the development of electrode materials but also in the design of all battery components, encompassing both electrochemically active and inactive parts.

2. Fundamentals and challenges of energy density in AZIBs

While recent efforts have primarily focused on improving the reversibility and lifespan of the Zn anode, the issue of low energy density in AZIB systems remains underappreciated. However, this often-overlooked drawback also plays a significantly decisive role in hindering the real-world applicability of AZIBs, particularly in energy-intensive applications. Although AZIBs offer lower production costs per unit energy (~100 USD per kWh) compared with LIBs (~130 USD per kWh), their relatively inferior energy densities impose significant spatial and weight constraints, particularly in applications where compact and lightweight configurations are required.[42] Furthermore, despite the theoretically high capacity of the Zn anode, the practical energy density of AZIBs falls short due to the cumulative contributions of other cell components and architectural limitations. The severity of the energy density gap is evident even when benchmarked against lithium iron phosphate (LFP, $LiFePO_4$), a cathode known for its lower cost and moderate energy density.[43] As a result, overcoming these issues is essential for enabling practical deployment of AZIBs, as they are unlikely to function as a comprehensive replacement for established LIB technologies without resolving such constraints.

Notably, the persistent gap underscores a critical limitation that cannot be addressed through cathode material optimization alone but rather requires system-level strategies to fully unlock the potential of AZIBs. Energy density, defined as the amount of energy stored per unit volume or mass of a battery system, can be expressed as: energy density (Wh g^{-1} or Wh cm^{-3}) = cell capacity (mAh) × working voltage (V) × (mass or volume)$^{-1}$ (g^{-1} or cm^{-3}).[44] Strategically, energy density has typically been improved through the development of advanced active materials that increase cell capacity or through the use of high-working-voltage electrode pairs that elevate the operating potential. For AZIBs, in which Zn^{2+} serves as the charge

transfer cation and metallic Zn functions directly as the anode active material, the redox potential of the cathode becomes the dominant determinant of the overall cell voltage. In addition, given the electrochemical constraints on the areal capacity of Zn anodes, developing or redesigning the cathode is also essential for increasing the total capacity of the full cell. Although improvements in active material-level properties have garnered considerable attention, attaining practically high energy density in AZIBs demands a broader set of design considerations.

Inherently, AZIBs are limited by a narrow electrochemical stability window (ESW) governed by water decomposition, which restricts the use of high-voltage cathode materials and places a fundamental constraint on cathode design.[45] To overcome this intrinsic limitation, expanding the ESW through electrolyte optimization has emerged as a crucial strategy, enabling stabilization of redox reactions at higher voltages. This, in turn, allows for the practical pairing of aqueous electrolytes with high-voltage cathode materials, which were previously inaccessible under conventional aqueous conditions. Tailoring cathode structure and composition to enhance specific capacity also represents a key avenue for increasing the intrinsic energy storage capability of the cathode, thereby contributing to overall energy density. Moreover, it is critical to reduce the volume and mass of electrochemically inactive components at the cell level to maximize practical energy density. For instance, since Zn anodes store energy through surface reactions, an increase in Zn volume that remains unexposed to the electrolyte leads to a greater proportion of electrochemically inactive material, which reduces the energy density in turn.[46] Therefore, constructing Zn anodes that can remain stable under high depth-of-discharge (DOD) conditions is essential. On the cathode side, increasing areal capacity through the adoption of thick electrodes is a promising approach for developing a high-energy-density cell, as it can minimize the overall proportion of electrochemically inactive components like current collectors.[47,48] However, conventional fluoropolymer-based binders such as poly(vinylidene fluoride) (PVDF) and poly(tetra fluoroethylene) (PTFE) are incompatible with thick-electrode configurations because they exhibit poor wettability toward aqueous electrolytes and insufficient structural integrity.[49–51] Meanwhile, commercial thin polyolefin-based separators commonly employed in LIB systems suffer from poor wettability with aqueous electrolytes owing to their hydrocarbon backbones, rendering them unsuitable for aqueous cells.[52,53] In response, glass fiber (GF) separators with excellent water compatibility have been adopted in AZIBs, but their considerable thickness and mass remain a structural obstacle that must be surmounted. Taken together, the above limitations highlight the need for a system-wide redesign that considers not only the electrochemical capability of each component but also its structural and functional compatibility within battery architectures. As a result, coordinated refinement of major cell elements is required by replacing widely used yet suboptimal materials with functionally tailored alternatives, thereby ensuring both electrochemical stability and practical performance.

To date, several outstanding reviews have addressed strategies for raising the energy density of AZIBs, with a particular focus on the development of high-voltage electrolytes, diverse cathode materials, and their associated mechanisms, which have reported significant progress toward achieving high-performance AZIBs and offered valuable insights for future research.[54–60] However, for practical deployment, enhancing the energy density of AZIBs requires an integrated understanding that surpasses individual components and considers all elements involved in the cell system. Fig. 1 illustrates representative bottlenecks for each AZIB component and introduces
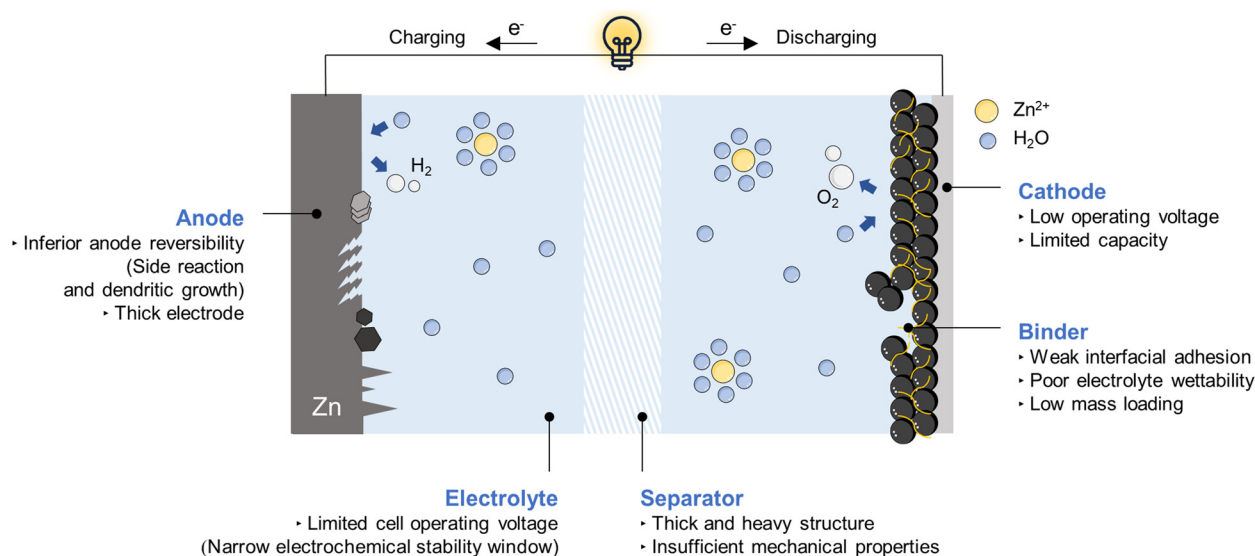

Fig. 1 Schematic illustration of critical factors preventing high-energy-density AZIBs. Key limitations across various components, including the anode, cathode, electrolyte, and separator, are highlighted to identify critical bottlenecks.

key strategies proposed to advance battery performance. In this review, we systematically discuss the strategies to realize high-energy-density AZIBs, extending beyond electrolyte and cathode development to encompass high-DOD anodes, engineering strategies for high-loading cathodes, and separators. First, approaches for electrolyte design aimed at expanding the ESW are examined, including strategies such as high-concentration composition and functional additives. Next, studies employing thin Zn metal anodes are reviewed, with a focus on increasing DOD while maintaining long-term cycling stability. Then, cathode development is introduced in terms of two aspects that involve increasing specific capacity and elevating operating voltage. In addition, recent efforts to develop appropriate binders and ancillary components for thick electrodes in high-energy-density applications are presented. Thereafter, the necessity of next-generation separators specified for aqueous systems is discussed, with particular emphasis on structural and chemical/electrochemical optimization. Finally, the review concludes by summarizing the above strategies and suggesting perspectives on the remaining challenges in realizing practically viable high-energy-density AZIBs.

3. Electrochemical window tuning *via* molecular-level electrolyte design

According to frontier orbital theory, the ESW of an electrolyte is governed by the relative position of its highest occupied molecular orbital (HOMO) and lowest unoccupied molecular orbital (LUMO).[61] When the electrode potential exceeds this HOMO–LUMO gap, parasitic redox reactions may occur.[62] Specifically, electrolyte oxidation can occur at the cathode and electrolyte reduction at the anode, which leads to the formation of interphase layers on both electrodes in organic systems.[63] In aqueous systems, on the other hand, such reactions trigger the OER at the cathode and the HER at the anode.[64] These parasitic processes cause water decomposition and lower overall energy efficiency.[65] Although various strategies have been proposed to enhance the energy density of AZIBs, one of the most critical approaches is to broaden the ESW of the electrolyte, thereby enabling a broader operating voltage range. While the ESW of aqueous electrolytes can slightly exceed that of pure water, it remains fundamentally constrained by the intrinsic ESW of water itself, which is only about 1.23 V.[56] Notably, the Zn/Zn^{2+} redox couple has a potential of −0.76 V, which lies well below the onset of the HER.[66] As a result, improving the low-voltage stability is a crucial requirement for suppressing gas evolution, preventing electrolyte decomposition, and enhancing anode reliability.[67] However, since the Zn^{2+} reduction reaction represents the lowest electrochemical potential available among Zn-related redox processes, expanding the upper voltage boundary is more essential for the development of high-voltage AZIBs. Accordingly, the maximum achievable cell voltage is constrained by the onset of the OER. In this context, efforts to pair the Zn/Zn^{2+} redox couple with high-voltage cathodes face

similar limitations, as the OER tends to occur either before or simultaneously with the redox processes of the cathode. This parasitic reaction not only competes with the desired electrochemical processes but also accelerates gas evolution and interfacial degradation, leading to poor cycling stability. As a result, suppressing the OER and extending the cathodic redox limit have become a key focus in the development of high-voltage and high-energy-density AZIBs.

Several criteria must be considered when modifying the aqueous electrolyte. In addition to suppressing the OER and HER, the electrolyte should also promote Zn anode stability, inhibit dendrite growth, and retain the inherently high ionic conductivity.[68] To achieve these goals, a variety of electrolyte modification strategies have been developed including highly concentrated salt formulations, introduction of co-solvents or deep-eutectic solvent (DES), functional additives, or employment of a gel polymer electrolyte (GPE).[69–73] Each approach contributes through distinct mechanisms, such as reducing water activity, immobilizing free water, or altering the Zn^{2+} solvation structure, helping to suppress water decomposition and broaden the ESW. In this section, representative studies employing electrolyte modification strategies are introduced, with a focus on elucidating the underlying mechanisms by which each approach contributes to expanding the ESW.

3.1 Suppressing water activity by superconcentrated electrolytes

Following the study by Ji's group on water-in-salt (WiS) electrolytes, a wave of research has explored WiS systems as a promising strategy to suppress parasitic water reactions in AZIBs.[74–76] The core concept involves using high concentrations of Zn salt to reduce water activity and alter the solvation structure, which results in improved high-voltage stability and significant suppression of the HER and OER compared with conventional aqueous electrolytes. However, the reliance on large quantities of salt limits the practical potential of WiS systems by increasing cost and reducing the environmental sustainability of AZIBs, particularly for grid-scale applications.[40] To address the limitations of conventional WiS systems, extensive research has been conducted on alternative strategies, including lean-water electrolytes that offer similar solvation characteristics with reduced salt concentrations. The following section introduces a representative example of this emerging strategy.

3.2 Co-solvent strategies for AZIBs

Co-solvents refer to secondary solvents that are introduced alongside water in aqueous electrolytes to tailor the physicochemical and electrochemical properties of the system.[77] Typically organic in nature, co-solvents are partially or fully miscible with water and serve to modulate key parameters such as solvation structure. They can weaken the solvation sheath of Zn^{2+} ions, facilitating faster desolvation kinetics at the electrode surface and enhancing Zn deposition reversibility.[78] Some co-solvents also contribute to interfacial stabilization by promoting the formation of robust SEI layers on Zn anodes or cathodes.[79] One of the primary roles of co-solvents,

however, is to expand the ESW by lowering the water activity and suppressing parasitic reactions.[80] By reducing the activity of free water molecules, co-solvents mitigate water decomposition and allow for more stable operation at both anodic and cathodic limits. Some co-solvents also contribute to interfacial stabilization by promoting the formation of robust SEI layers on Zn anodes or cathode electrolyte interphase layers on cathodes.[81] Notable examples include ethylene glycol and tetraglyme, which have been widely explored for their ability to synergistically coordinate with water and reshape the electrolyte properties.[82,83] The design of water/co-solvent systems thus represents a promising direction to overcome the inherent limitations of conventional aqueous electrolytes, especially in the pursuit of high-voltage and long-cycle-life AZIBs.

Building upon these fundamental principles, recent efforts have sought to rationally tailor solvation environments and interfacial chemistry using functionalized co-solvents. For instance, Li et al. introduced a co-solvent strategy for AZIBs by incorporating tetramethylene glycol (TG4), a water-miscible organic solvent with abundant polar functional groups and hydrogen bond acceptors, to regulate interfacial ion behavior and solvation structure.[84] Specifically, an electrolyte composed of 1 m $Zn(OTf)_2$ with 50 vol% TG4 was formulated and employed. Molecular dynamics (MD) simulations revealed that TG4 molecules actively participated in the primary solvation sheath of Zn^{2+}, partially displacing H_2O (Fig. 2a and b). Additionally, Raman spectroscopy confirmed that the addition of TG4 resulted in enhanced weak hydrogen bonding near 3500 cm^{-1} and a concurrent decrease in strong hydrogen-bonding interactions. This spectral transition implies that increasing the amount of co-solvent effectively suppressed water activity (Fig. 2c). As a result, this reduction in water activity effectively suppresses both the HER and OER, as evidenced by the diminished gas evolution current observed in Fig. 2d. Such solvation modulation contributes directly to the mitigation of H_2O-derived parasitic reactions and enables stabilized Zn^{2+} transport and nucleation. As a result, not only was water activity effectively reduced, but also the Zn anode benefited from reinforced interfacial stability and reversibility. Zn||Zn symmetric cells exhibited long-term cycling stability for over 7000 hours at a current density of 1 mA cm^{-2}.

Similar to the aforementioned strategy that directly modulates the primary solvation structure of Zn^{2+} via co-solvent incorporation, some studies have proposed alternative approaches. Recently, Chen's group reported a new solvation structure induced by the co-solvent, where the primary solvation shell remains unaltered, while the co-solvent participates in the secondary solvation layer and constructs capsule-like solvation nanoclusters through an anion-bridging mechanism.[85] This co-solvent strategy introduces hexafluoro isopropanol (HFIP) as a recessive solvent that assists in reorganizing the solvation environment. Although HFIP alone cannot dissolve Zn salts, it is activated in the presence of hydrogen bonding interactions and polar anions (e.g., OTf^-) to form a

ternary bridging structure with water, resulting in a nested "HFIP–anion–H_2O" solvation shell (Fig. 2e). This architecture not only weakens the coordination strength of H_2O but also promotes favorable desolvation kinetics of Zn^{2+} at the interface (Fig. 2f). Importantly, during Zn plating, HFIP positioned at the outer interface of the solvation capsule and characterized by a lower LUMO energy level is preferentially reduced. This reduction initiates the in situ formation of a hydrophobic interfacial layer, which acts as a physical barrier to water molecules. By decreasing the local water activity at the electrode surface, the interfacial layer contributes to improved Zn^{2+} nucleation behavior and stabilized interfacial behavior. Moreover, the hydrated solvation structure is thermodynamically stabilized by HFIP and provides augmented resistance against electrochemical decomposition with an expanded ESW of 2.8 V. Accordingly, HFIP-containing nano-capsule electrolyte allows for broader voltage operation without noticeable gas evolution or cathodic passivation, offering a promising pathway conducive to delivering a high energy density of 57.1 Wh kg^{-1} in AZIBs.

Unlike previous approaches using single-component co-solvents, some studies have explored alternative approaches. For example, Wang et al. used a dual co-solvent strategy that leverages dimethyl acetamide (DMAC) and trimethyl phosphate (TMP) to suppress water reactivity in AZIBs.[86] DMAC and TMP were selected for their strong polarity and electron-rich C=O and P=O groups, which can interact with both solvated and free water molecules to restructure the solvation environment and restrict the activity of water. [1]H nuclear magnetic resonance (NMR) spectroscopy in Fig. 2g revealed an upfield shift in the water proton signal (3.52 ppm) in the hybrid electrolyte (HE), compared with aqueous Zn electrolytes (AE). This shift indicates that the co-solvents induce electron donation to water protons, enhancing shielding and reducing the tendency for H^+ dissociation. Density functional theory (DFT) calculations further confirmed that the deprotonation energy of H_2O in the Zn^{2+} solvation shell increases from −4.94 eV in the aqueous system to −2.43 eV in HE, making proton loss less favorable (Fig. 2h). The modified solvation chemistry leads to a widened ESW of 2.11 V and suppresses parasitic reactions, which underscores how tailored dipole interactions from multiple co-solvents can synergistically regulate solvation chemistry and interfacial behavior in AZIBs. Comprehensively, co-solvent strategies demonstrate significant potential by effectively suppressing the OER, offering a major advantage in widening the ESW. Beyond OER mitigation, the suggested system has also achieved stabilized Zn anode performance and demonstrates feasibility in high-capacity pouch cell configurations, highlighting their practical applicability.

3.3 DES-mediated electrolyte structuring through hydrogen bonds

Both co-solvent and eutectic electrolytes are formulated by incorporating organic components into water-based systems. However, they differ fundamentally in how the components
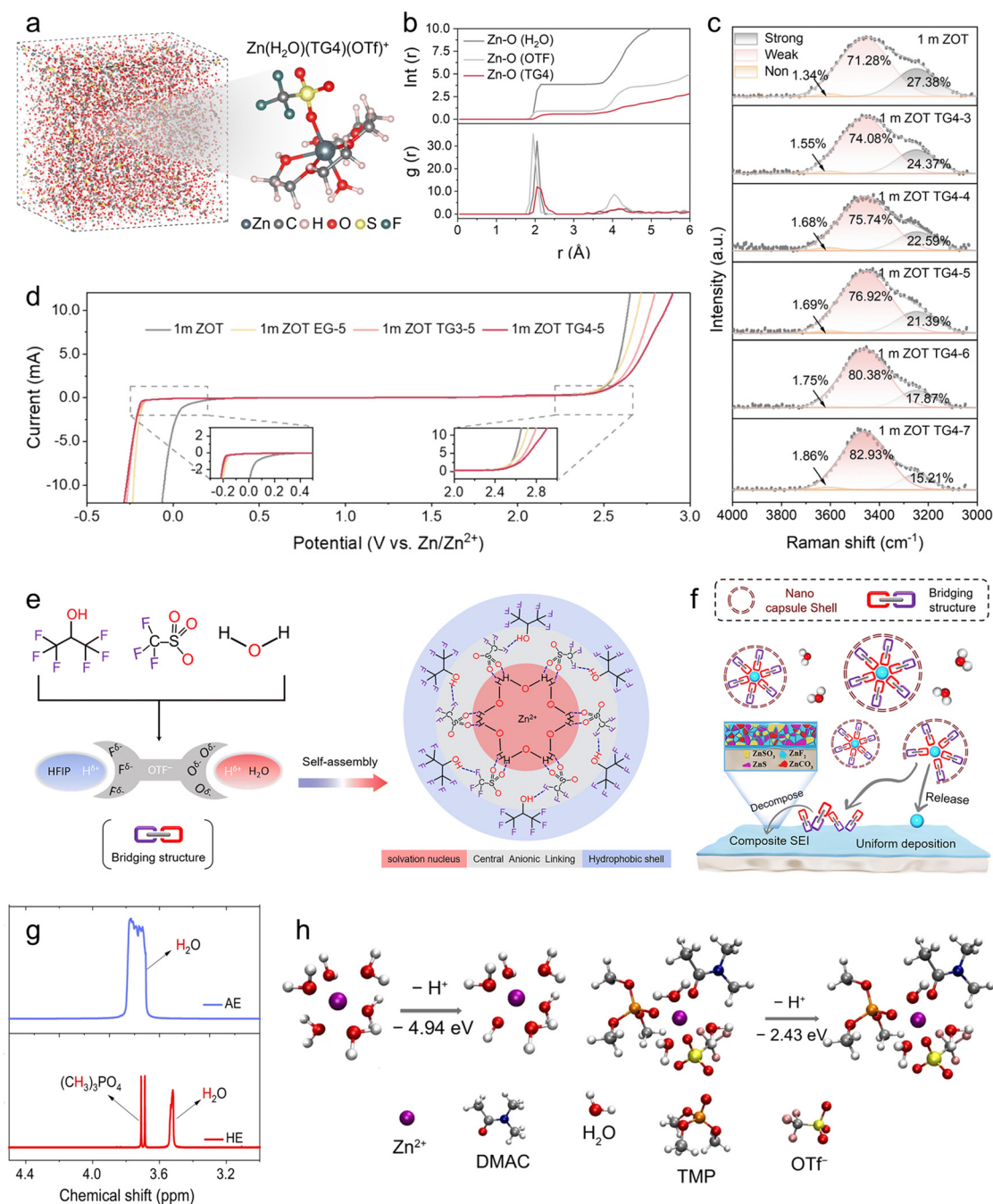
Fig. 2 Co-solvent-mediated strategies for electrolyte stability enhancement. (a) 3D snapshots of the MD simulations and schematics of the Zn^{2+} solvent sheath revealing the structural influence of TG4 as a co-solvent. (b) RDFs and corresponding coordination numbers of Zn^{2+} in 1 M ZOT TG4−5 electrolyte. (c) Raman spectra of TG4/H_2O co-solvent electrolytes with varying TG4 content. (d) LSV curves for various electrolytes tested with Zn‖Ti cells. Reproduced with permission from ref. 84. Copyright 2025, The Royal Society of Chemistry. (e) Schematic illustration of activating recessive solvents *via* the bridging structure and constructing a nano-capsule solvation structure. (f) The Zn plating process in nano-capsule electrolytes. Reproduced with permission from ref. 85. Copyright 2025, The Royal Society of Chemistry. (g) ^1H NMR spectra for pure water, conventional electrolyte and a hybrid electrolyte composed of DMAC and TMP. (h) Deprotonation (H^+ dissociation of H_2O) energy from Zn^{2+} inner solvation shell of the two electrolytes. Reproduced with permission from ref. 86. Copyright 2023, Springer Nature.

interact and how the final electrolyte phase is formed. Co-solvent systems are based on the physical mixing of water with miscible organic solvents, resulting in a simple dilution effect. In contrast, DESs are defined as specific compositional combinations of two or more components with a modified melting point. They form hydrogen bonding between a hydrogen bond acceptor (HBA) and a hydrogen bond donor (HBD).[87,88] Consequently, DES-based electrolytes often exhibit reduced

free water activity, which may contribute to an enlarged ESW under certain conditions.

One representative study of eutectic electrolyte design employed sulfolane (SL) as a HBD to construct a hybrid SL–water system for AZIBs.[89] By tuning the SL content, the authors investigated how solvation structures and free water are affected. At the bulk scale, the blue shift of bending and stretching modes at 1620 and 3400 cm^{-1} in Fourier transform infrared (FT-IR) spectrum indicates a strengthened O–H bond and reduced water activity due to the interaction between SL and H_2O (Fig. 3a). More importantly, a notable feature of this study is that MD simulations and formation energy analysis confirmed that the fully hydrated $(Zn(H_2O)_6)^{2+}$ structure is thermodynamically more stable than partially substituted species such as $Zn^{2+} \cdot 4H_2O \cdot 2OTf^-$ or $Zn^{2+} \cdot 4H_2O \cdot 1OTf^- \cdot 1SL$ (Fig. 3b). For both structures, the Gibbs free energy of transformation into the fully hydrated structure is negative, with values of -62.4 kJ mol^{-1} and -282.6 kJ mol^{-1}, respectively, indicating the thermodynamic favorability of complete hydration. When water-free Zn^{2+} solvation or ion pairing with
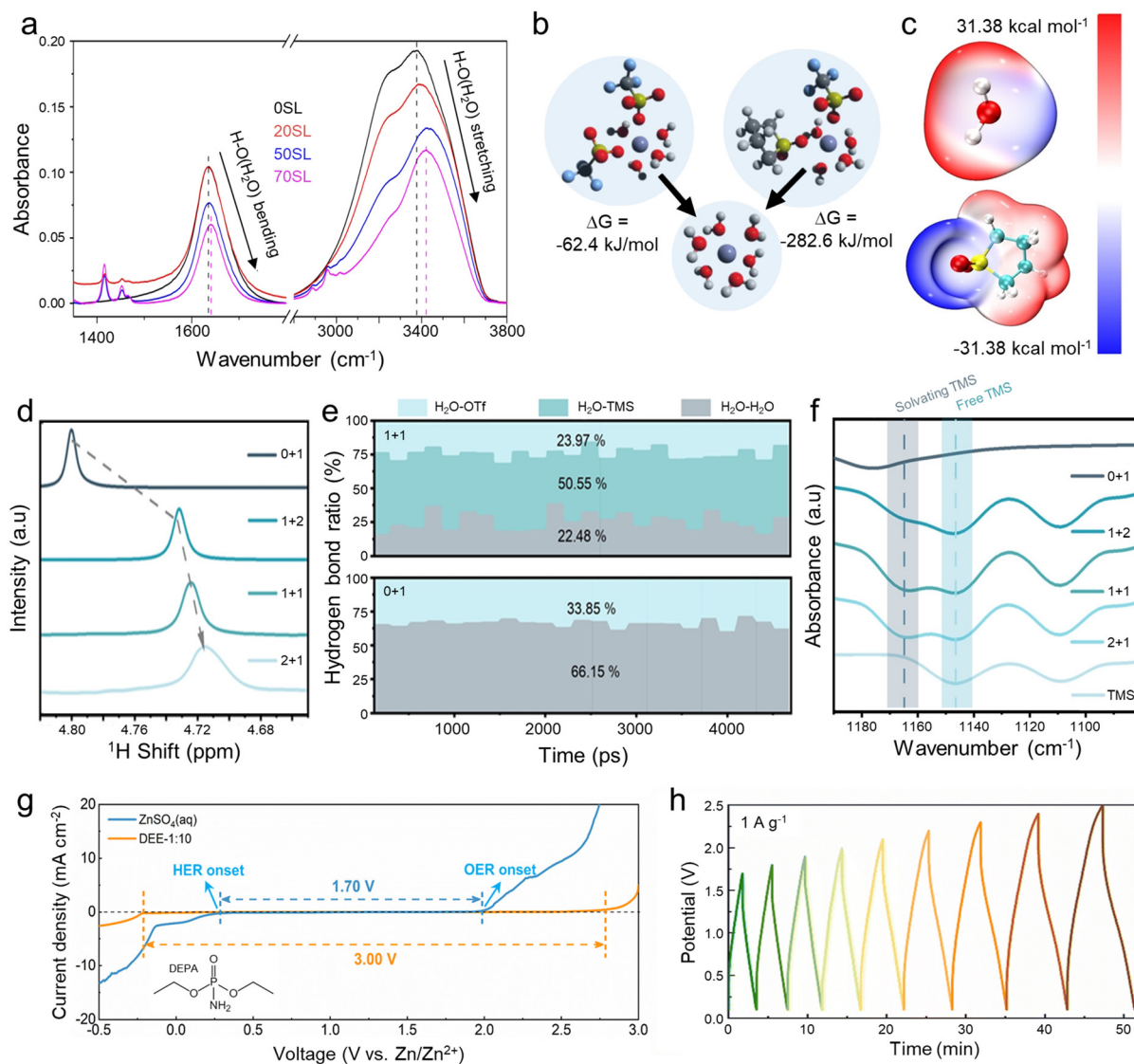

Fig. 3 Design principles of electrolytes with widen ESW guided by DES chemistry. (a) FTIR spectral evolution of electrolytes with SL. (b) DFT-computed reaction energies to form fully hydrated Zn^{2+} from other cluster types (left: $Zn^{2+} \cdot 4H_2O \cdot 2OTf^-$, right: $Zn^{2+} \cdot 4H_2O \cdot 1OTf^- \cdot 1SL$). Reproduced with permission from ref. 89. Copyright 2023, Springer Nature. (c) Electrostatic potential maps of TMS and H_2O molecule. (d) NMR spectra with varying TMS content. (2 M Zn(OTF)$_2$ concentration is maintained, ratio of TMS to H_2O is 0 : 1, 1 : 2, 1 : 1 and 1 : 2) (e) Different types of hydrogen bonds ratio in MD simulation of 1 + 1 and 0 + 1, (f) FTIR spectra of pure TMS, 0 + 1, 1 + 2, 1 + 1 and 2 + 1. Reproduced with permission from ref. 90. Copyright 2023, Wiley-VCH. (g) LSV curves of Zn–SS cells using a DES electrolyte containing DEPA and a ZnSO$_4$-based aqueous electrolyte at 1 mV s^{-1}. The inset presents the chemical structure of DEPA. (h) GCD curves of Zn-ion hybrid capacitor from 0.1 V to 2.5 V. Reproduced with permission from ref. 92. Copyright 2024, The Royal Society of Chemistry.

OTf$^-$ occurs, the desolvation energy barrier increases and Zn^{2+} transport is hindered, which demonstrates that maintaining the six-water solvation is critical. The hydrated shell, therefore, enables more favorable interfacial desolvation kinetics in aqueous systems containing SL. In addition, the presented eutectic strategy was also shown to suppress water decomposition and expand the ESW by forming a strong hydrogen-bonding network between SL and water molecules, which reduces water activity.

Interestingly, another study applied the same molecule, but with a different mechanism from the one used above, referred to as tetramethylene sulfone (TMS) in a hydrated deep eutectic solvent (HDES) system.[90] Zhong et al. presented a mechanistically similar yet functionally distinct approach at the molecular level. While the previous study primarily focused on reducing free water activity by disrupting H$_2$O–H$_2$O hydrogen bonding, this work placed greater emphasis on tuning the solvation structure of Zn^{2+} based on electrostatic potential (ESP) calculation of water and TMS (Fig. 3c). The result showed that S=O is more attractive to hydrogen atoms than O–H in the water molecule, because of the negative charge distribution. The ESP culminates in the following effect, as demonstrated in Fig. 3d: ^{1}H NMR spectroscopy revealed an upfield shift of the D$_2$O signal from 4.80 ppm to 4.71 ppm, which suggests increased electron density around water protons due to the formation of hydrogen bonds between TMS and D$_2$O. The shift also reflects suppressed water reactivity and restructured hydrogen-bond networks. Additionally, MD simulations also confirmed that TMS disrupts weak H$_2$O–H$_2$O hydrogen bonding, reducing the average hydrogen bond ratio from 66.2% to 22.5%, while simultaneously promoting the formation of stable TMS–H$_2$O interactions (Fig. 3e). Together, these spectroscopic and computational results consistently demonstrate the disruption of weak H$_2$O–H$_2$O hydrogen bonding by TMS, highlighting the role it plays in reshaping the aqueous hydrogen-bonding environment. The formation of TMS–H$_2$O hydrogen bonds also inhibits the dissociation of ionic intermediates during proton-coupled steps, thereby suppressing the HER and widening the electrolyte's ESW from 2.11 to 4.08 V. In addition, MD simulations further demonstrated that TMS molecules enter the primary solvation sheath of Zn^{2+} in the DES system. TMS coordination with Zn^{2+} was further evidenced by a distinct vibrational peak, which appeared upon the addition of Zn(OTf)$_2$ as observed in FTIR spectra (Fig. 3f). The coordination interactions also enabled the intercalated TMS molecules to function as structural pillars within the NH$_4$V$_4$O$_{10}$ (NVO) cathode, improving zincophilicity and stabilizing the structure. Taken together, this study highlights the multifunctional role played by TMS, from hydrogen-bond reorganization to coordinated solvation and structural modulation, and provides a compelling strategy for advanced AZIBs.

In line with the previous study, solvation structures in DES-based electrolytes have also been extensively investigated, and among these, several reports have proposed composition-dependent solvation models. For instance, Chen et al. reported a systematic study on how varying water content affects the Zn^{2+} solvation environment in a DES composed of ethylene glycol (eg) and Zn salt.[91] DFT calculations identified [Zn(H$_2$O)$_6$]$^{2+}$ as the dominant Zn^{2+} species in highly hydrated environments, where six water molecules coordinated the cation with relatively weak interactions (−2.8 eV). In DES-based media, Zn^{2+} strongly coordinated with eg and anions (−10.0 eV), a configuration that compromises ionic mobility. As the water content increased, the solvation sheath gradually transitioned toward a more aqueous-like coordination, reducing anion participation and weakening binding strength. A finely tuned water-deficient coordination structure, such as [Zn(H$_2$O)$_2$(eg)$_2$(OTf)$_2$], was shown to promote Zn^{2+} dissociation while reducing water activity. Combined with the presence of bound-free water molecules in the bulk phase, this environment effectively suppressed the HER and OER, resulting in a widened ESW exceeding 2 V. This study underscores the dynamic solvation behavior in DES systems and highlights the critical role played by water in modulating both solvation structure and electrolyte performance.

In addition to expanding the ESW, Bai et al. demonstrated stable battery operation across a wide temperature range by utilizing the intrinsic properties of eutectic solvents.[92] Diethyl phosphoramidate (DEPA) was employed to formulate a DES-based Zn(TFSI)$_2$ electrolyte. Similar to previous DES-based systems, the authors confirmed the reorganization of the hydrogen-bond network and restructuring of the Zn^{2+} solvation sheath in the DEPA-containing medium. The ESW became wider, which was evident from the delayed onset of the HER and OER (Fig. 3g). The Zn-ion hybrid capacitor further demonstrated high voltage tolerance with the operating window ranging from 0.1 V to 2.5 V of modified electrolyte, which exhibits superior stability compared with conventional aqueous electrolytes (Fig. 3h). Notably, as a practical demonstration, Zn||V$_2$O$_5$ full cells were also operated at both −20 °C and 80 °C, which supports the thermal adaptability of the system. The work underscores the potential of carefully tailored eutectic formulations in enabling stable AZIB operation under harsh environmental conditions, while simultaneously addressing interfacial and solvation challenges.

The unique advantage of HBD–HBA interactions in DES-based electrolytes immobilizes free water and maintains operability at low temperatures. This combination of properties provides dual functionality that overcomes the freezing limitation observed in conventional aqueous systems. In addition to pushing the ESW limit, the anti-freezing properties make the system a highly promising direction for future aqueous electrolyte research.

However, although numerous co-solvent-based and DES-based strategies have been extensively explored in AZIBs and have demonstrated various advantages, several fundamental limitations remain unresolved. Co-solvents and DES-based electrolytes are widely used to tailor solvation structures and broaden the ESW, yet their incorporation often compromises the intrinsic benefits of aqueous systems. While water-based electrolytes naturally possess much higher ionic conductivity

and lower viscosity compared with organic electrolytes used in LIBs, the addition of organic solvents tends to reduce ion mobility and increase viscosity, and co-solvent systems as well as DESs exhibit similar characteristics.[93,94] In parallel, the flammability of many organic co-solvents poses serious safety concerns, which directly conflict with the inherent non-flammability of aqueous electrolytes.[95,96] Many co-solvent and DES systems also fail to retain the inherent advantages of aqueous batteries and often introduce flammability. Another critical concern is the use of large amounts of organic solvents in these systems, which requires continuous consideration of environmental impacts. The production, handling, and disposal of organic-rich electrolyte formulations often increase the carbon footprint and introduce ecological burdens, which undermine the sustainability appeal of AZIBs. The mentioned properties undermine a key motivation for adopting AZIBs, and continuous efforts are required to develop alternative approaches that address this critical drawback.

3.4 Electrolyte modulations *via* additives

Additives are defined as a set of functional compounds that are intentionally 'added' to electrolytes to address their fundamental deficiencies. Similar to co-solvent and DES strategies, they function by reorganizing the Zn^{2+} solvation structure or decreasing the amount of free water, thereby suppressing water decomposition and extending the ESW. In addition to widening the ESW, additives operate through various mechanisms such as electrostatic shielding, interfacial adsorption, *in situ* formation of SEI, enhancement of water stability, and surface texture regulation.[97–100] Furthermore, many additives possess well-defined functional groups that induce unique and diverse physicochemical behaviors within the electrolyte, a characteristic that continues to receive considerable scientific attention.

In the following section, we examine the roles played by various additive types and how these functionalities have been strategically leveraged to push the energy density limits of AZIBs.

The first study to be introduced as an additive strategy utilized a large dosage of additives to construct a densified electrolyte, thereby enhancing electrochemical performance. Unlike conventional strategies where additives dissolve into the electrolyte, the modification here originates from the densifying effect of undissolved particles. $SrTiO_3$, a cubic perovskite oxide, has been employed as a functional additive (Fig. 4a).[101] Upon dispersion in aqueous systems, the uniformly dispersed $SrTiO_3$ particles (<5 μm) created a grayish-white colloid with semi-solid texture (Fig. 4b and c). This densified electrolyte weakened the hydrogen bonding network of water, as evidenced by a shift from strong to medium hydrogen bond dominance in Raman spectra. The reduction in strong H-bond area from 49% to 41% indicated reduced water activity, which contributed to broadening the ESW from 1.8 V to 2.2 V. Importantly, the system not only tolerated higher voltages but also supported practical operation up to 2.0 V in Zn‖ MnO_2 full cells. As shown in Fig. 4d, the conventional electro-

lyte exhibited MnO_2 formation near 1.99 V due to Mn^{2+} oxidation during charging. In contrast, the densified electrolyte avoided this process and remained stable when charged to 2 V. Collectively, this approach demonstrates concurrent improvements in both voltage window and capacity, and provides a promising route for high-energy-density AZIBs.

Most additive-based strategies modify the electrolyte with minimal changes to structure and functionality.[72] Unlike co-solvents, DESs, and high concentration additives that significantly alter solvation environments, this method uses a gentler modification. Nevertheless, the ability to achieve functional improvements with only trace amounts of additives offers clear advantages in terms of cost, environmental compatibility, and retention of aqueous system safety. Such benefits correspond closely to the core strengths of AZIBs, and the compatibility has encouraged increasing attention toward additive-based electrolyte design.

Several examples have demonstrated the application of small amounts of additives, and some representative studies are introduced here. The first work was reported by Wang's group, where *N,N*-methylenebis(acrylamide) (MBA) with a –CONH– functional group was employed as an additive.[102] ESP analysis revealed that the lowest ESP site was an oxygen atom with a value of −10.8 eV. This result showed that the oxygen in MBA was favorable for forming hydrogen bonds with water. NMR analysis further confirmed the interaction. The ^1H chemical shift of water in the MBA-containing electrolyte moved to a lower ppm compared with the bare electrolyte (Fig. 4e). The downfield shift demonstrated stronger electron shielding of H_2O, and the observation supported the formation of hydrogen bonding between MBA and water molecules. IR analysis provided additional confirmation by revealing reduced water activity. The combined spectroscopic evidence demonstrated that water activity decreased in the presence of MBA. The reduced water activity suppressed water decomposition, inhibited the OER, and broadened the ESW. Although MBA is widely used as a crosslinking agent, the work by Wang's group revealed that MBA can also act effectively as an electrolyte additive.[102]

Another example of additives applied in electrolytes is the saccharide family. Saccharide-based compounds such as glucose, trehalose, and dextran are typically used in areas such as food processing and biomedical applications, but they have also been shown to enhance battery performance when introduced as electrolyte additives.[103–106] Especially, trehalose and dextran are effective because both suppress the OER and broaden the ESW. Trehalose is a disaccharide composed of two glucose units, while dextran is a branched polysaccharide composed of multiple glucose units linked together by glycosidic bonds. Liu *et al.* demonstrated that the introduction of trehalose to AZIBs increases the proportion of strong hydrogen bonds (denoted as O–H1) (Fig. 4f). Because ESP analysis revealed that the hydroxyl groups of trehalose serve as electron donors capable of forming hydrogen bonds with water molecules, the amount of free water decreases and a stable hydrogen-bonding network is established between
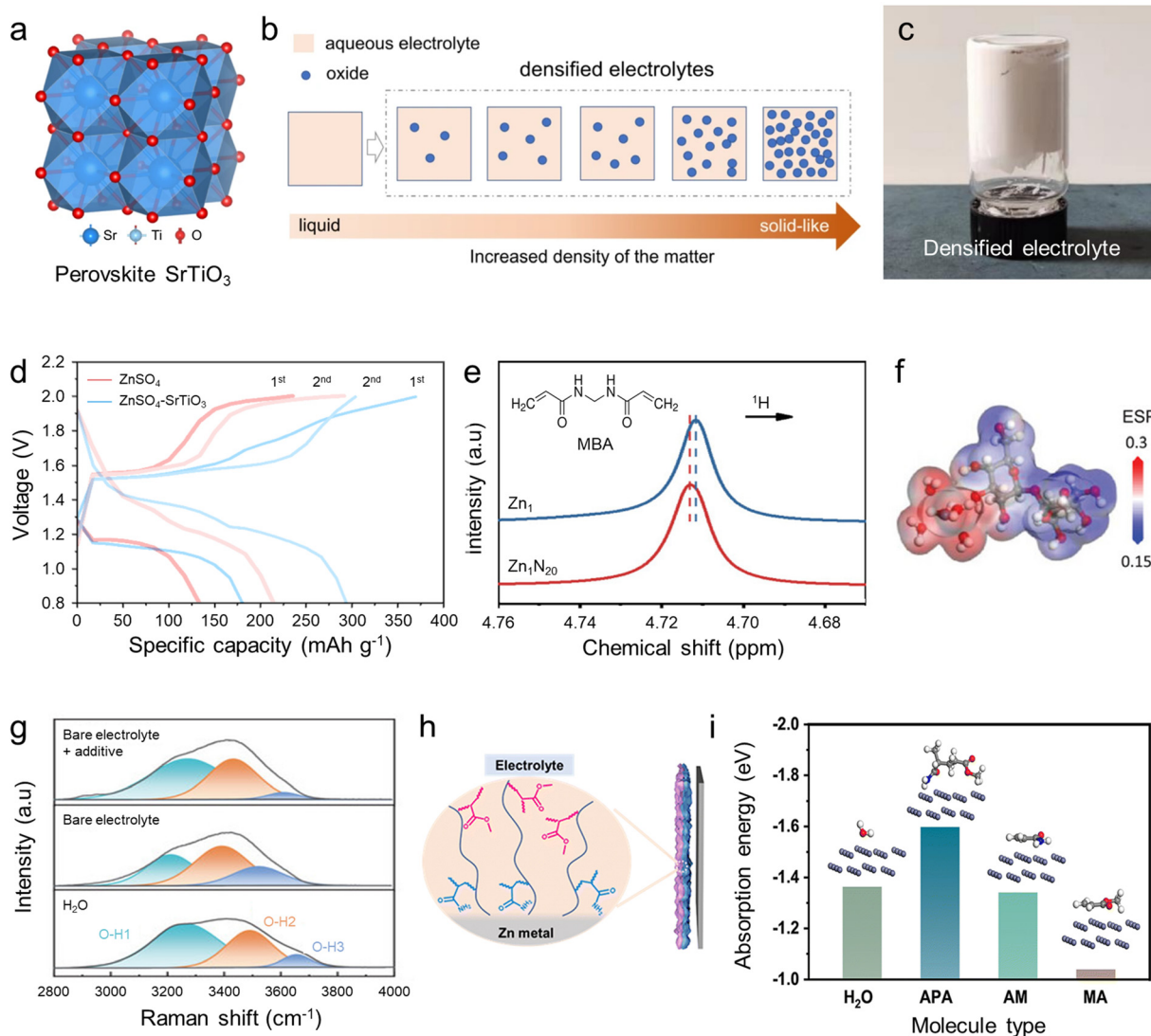
Fig. 4 ESW expansion strategies through additive-assisted electrolyte design. (a) The crystal structure of SrTiO₃. (b) Schematic illustration of densified electrolytes formed by increasing density of solution after the addition of oxide. (c) Optical photos of the densified electrolyte. (d) The first two charge and discharge curves of Zn/MnO₂ full cells. Reproduced with permission from ref. 101. Copyright 2023, Springer Nature. (e) ^{1}H NMR spectra of bare electrolyte (Zn_1) and electrolyte with MBA additive (Zn_1N_{20}). The inset depicts the chemical structure of MBA. Reproduced with permission from ref. 103. Copyright 2024, American Chemical Society. (f) Raman spectra of H₂O, bare electrolyte, and electrolyte with trahalose additive. (g) Electrostatic potential mapping of Zn^{2+}-5H₂O-trahalose. Reproduced with permission from ref. 105. Copyright 2023, Wiley-VCH. (h) An amphiphilic polymer layer forming a hydrophobic interfacial barrier at the Zn/electrolyte interface. (i) Adsorption energy of H₂O, APA, MA and AM on the Zn (101) surface. Reproduced with permission from ref. 107. Copyright 2023, The Royal Society of Chemistry.

trehalose and water (Fig. 4g). The reconstructed hydrogen-bonding network suppresses water decomposition and increases the overpotential required for the reaction. The increased overpotential ultimately contributes to an expanded ESW.

In addition to trehalose, Wei's group also demonstrated that dextran, when used as an additive, suppresses the OER and enhances electrochemical performance similar to trehalose.[106] In particular, the group confirmed that dextran improves AZIB's performance not only in a single-electrolyte system but also consistently across Zn(CF₃SO₃)₂, ZnSO₄, Zn

(ClO₄)₂, and ZnCl₂ electrolytes. The consistent performance across different systems highlights the broad chemical compatibility of dextran in Zn-ion batteries.

Not only small-molecule additives but also high-molecular-weight compounds such as dextran have been widely reported, and an additional example is the use of poly(acrylamide-co-methyl acrylate) (APA) as an AZIB additive.[107] The study, which was introduced by Niu et al., incorporated a nonionic amphiphilic copolymer additive, poly(acrylamide-co-methyl acrylate) (APA), into Zn(OTf)₂ electrolytes to regulate interfacial chemistry and mitigate water-induced side reactions. APA is com-

posed of 85 mol% hydrophilic acrylamide (AM) and 15 mol% hydrophobic methyl acrylate (MA) units. The amphiphilic structure enables preferential adsorption of AM segments onto the Zn surface, while the hydrophobic MA segments form a local interphase that prevents direct contact with bulk water (Fig. 4h). Fig. 4i further confirmed that AM units exhibit stronger adsorption on the Zn metal surface than either H_2O or MA, accounting for the stability of the protective interfacial layer. This adsorption not only suppressed Zn corrosion but also promoted the formation of an F-rich, O-deficient composition *via* anion cleavage. Beyond interfacial stabilization, linear sweep voltammetry (LSV) corroborated these findings by confirming suppressed HER and OER. Although a full-cell demonstration at high voltages was not reported, the system exhibited stable cycling up to 1.9 V in a capacitor configuration, underscoring its strong potential for high-voltage operation.

As discussed in previous studies, additives have the distinct advantage of tailoring electrolyte properties with only a trace amount of material. However, the use of such small quantities inherently limits the extent to which the electrolyte's fundamental structure and electrochemical environment can be altered. In addition, several studies have attempted to expand the ESW by adjusting the electrolyte pH through the use of additives. While this may appear effective, it is important to recognize that tuning pH does not fundamentally widen the ESW.[116] This is because the HER inevitably persists during continuous cycling. Therefore, extensive research and careful consideration are still needed to address this challenge.

To enable not only the expansion of the ESW but also the practical implementation of AZIBs, additive design should be approached from a more holistic perspective. First, most existing studies have employed single-component additives aimed at resolving isolated interfacial issues. Composite additive systems that integrate multiple functions such as polymeric adsorption and electrostatic shielding should be developed to achieve synergistic effects. Clarifying the interplay between different additive functionalities will be essential to constructing more robust interfacial environments. Second, although numerous studies have explored the influence of organic additives on Zn anodes, comparatively fewer have investigated their impact on cathode behavior. Given the central role played by cathodes in determining full-cell performance, additive strategies must be extended to assess whether additives contribute to structural reinforcement at the cathode as demonstrated in earlier studies, or inhibit detrimental phenomena such as transition metal dissolution and Zn^{2+} intercalation interference. A holistic understanding of additive–cathode interactions will be vital for achieving balanced electrochemical performance across both electrodes. Finally, the cost-efficiency of electrolyte additives should be carefully evaluated. While generally more affordable than WiS systems, additives still require optimization to maximize performance per cost. The development of low-cost, high-efficiency additives will play a pivotal role in accelerating the commercial adoption of AZIB technologies.

3.5 GPE-based electrolyte modification strategies

Among various electrolyte systems developed for AZIBs, polymer electrolytes have emerged as a promising solution to address leakage issues associated with liquid electrolytes, particularly in flexible or deformable battery formats.[108] Polymer electrolytes are broadly classified into two main types: solid polymer electrolytes (SPEs) and GPEs.[109] Among them, SPEs exhibit inherently wider ESW than aqueous electrolytes, but their low ionic conductivity at room temperature and high interfacial resistance severely limit their practical application in energy storage devices, despite their superior mechanical strength.[110,111] In contrast, GPEs have attracted growing interest owing to their semi-solid nature, which allows for higher ionic conductivity at ambient temperature and alleviates interfacial challenges during cycling.[112]

Within the broad class of GPEs, hydrogel-based electrolytes stand out due to their three-dimensional (3D) polymer networks that highly absorb water.[113] This hydration not only imparts softness and flexibility but also facilitates efficient ion transport through the hydrated channels. Occasionally, unlike conventional liquid electrolytes, hydrogels can suppress water-related parasitic reactions by forming tailored hydrogen bonds between water molecules and functional groups within the polymer matrix. Such intermolecular interactions modulate water activity and contribute to improved interfacial stability. Owing to this combination of electrochemical and structural benefits, hydrogel electrolytes are now recognized as a versatile platform for next-generation energy storage systems.

To further explore the practical utility of hydrogel electrolytes, recent studies have focused on leveraging specific functional polymers to modulate interfacial control and electrochemical performance. Among various candidates, biopolymer-based hydrogels have shown particular promise due to their inherent biocompatibility and ability to form strong hydrogen-bonding networks.[114,115] In this context, hyaluronic acid (HA), a naturally occurring polysaccharide, was employed to construct a tailored gel polymer electrolyte system. The HA-based gel polymer electrolyte was developed to fortify the electrochemical stability of aqueous Zn||LiMn$_2$O$_4$ batteries. By constructing a hydrogen-bonded polymer network, the HA gel reduced water activity and regulated interfacial solvation. Compared with the liquid electrolyte, where oxygen evolution became increasingly severe upon cycling, the HA-based system effectively suppressed gas formation and parasitic side reactions, as evidenced by negligible OER signals in differential electrochemical mass spectrometry (DEMS) measurements (Fig. 5a). As shown in Fig. 5b and c, to gain further insight into interfacial ion dynamics, *in situ* synchrotron-based FTIR spectroscopy was also employed to track real-time solvation interactions during Zn plating and stripping. Both HA gel and liquid electrolytes exhibited reversible variations in O–H and SO_4^{2-} vibrational bands, reflecting the desolvation and resolvation of Zn^{2+} at the interface. Notably, the HA gel system showed a more pronounced blue shift of the O–H bond and reduced sulfate intensity during plating, indicating accelerated
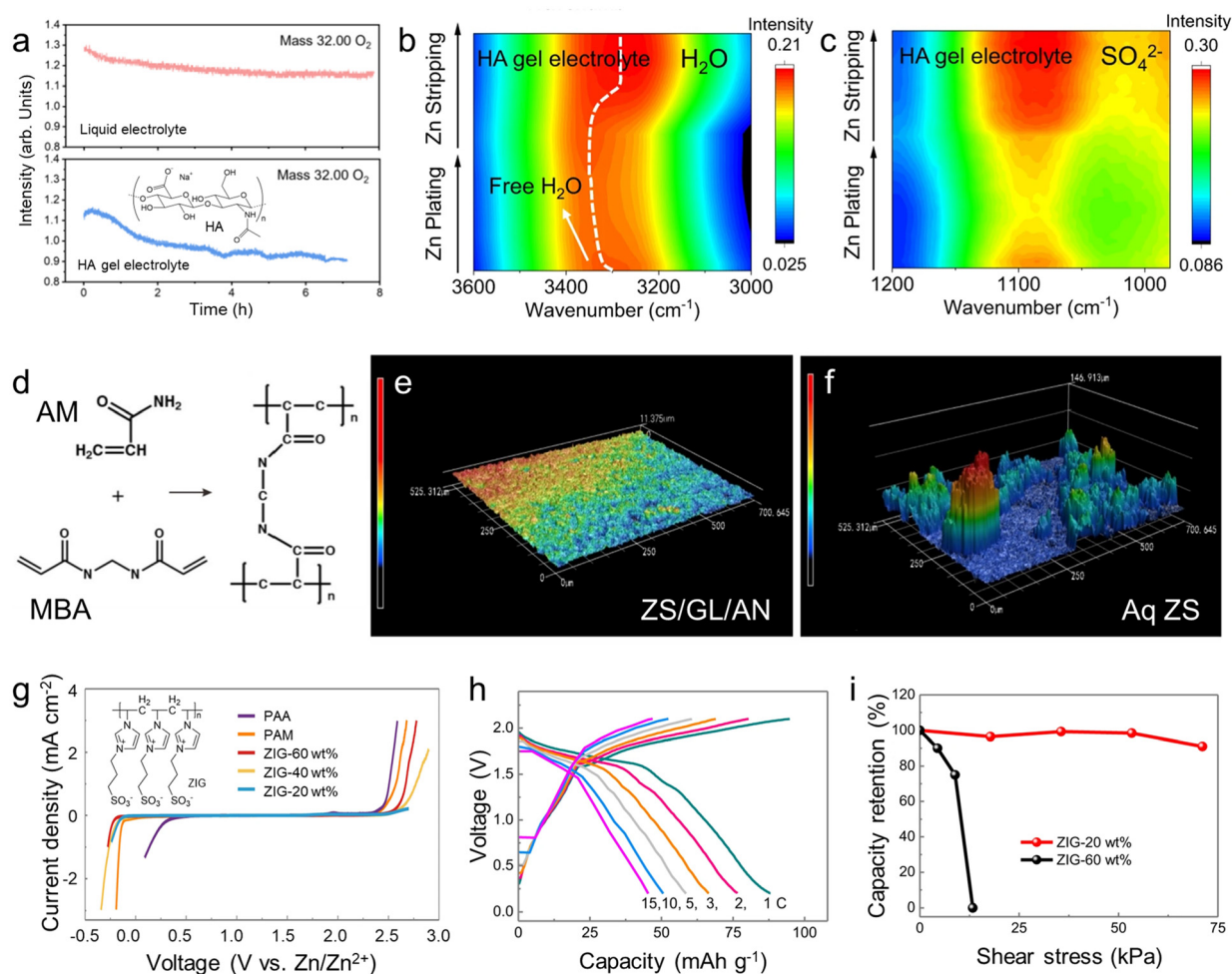
Fig. 5 Design strategies of GPE for high-voltage AZIBs. (a) The O_2 spectra obtained from differential electrochemical mass spectrometry of Zn‖ LMO cells upon charge/discharge at a current rate of 1C in the liquid electrolyte and the HA gel electrolyte. The inset depicts the chemical structure of HA. *In situ* synchrotron-FTIR spectra in attenuated total reflection (ATR) mode of stainless-steel electrode during Zn plating/stripping. (b) $\nu(\text{OH})$- HA gel electrolyte, (c) $\nu(\text{SO}_4^{2-})$-HA gel electrolyte. Reproduced with permission from ref. 115. Copyright 2023, Springer Nature. (d) The polymeriz- ation mechanism diagram of the hydrogel electrolyte. The corresponding 3D surface topographies of the cycled Zn electrodes with (e) the hydrogel electrolyte and (f) the conventional electrolyte. Reproduced with permission from ref. 116. Copyright 2022, Elsevier. (g) LSV of ZIG (20, 40, 60 wt% water content), PAM and PAA (conventional HPEs). The inset presents the chemical structure of ZIG. (h) Discharging−charging profiles of Zn‖MnHCF cell with the ZIG-20 wt% electrolyte at different rates. (i) Capacitance retentions of the full battery based on ZIG with 20 wt% and 60 wt% water con- tents at different shear stresses. Reproduced with permission from ref. 111. Copyright 2023, Springer Nature.

removal of water molecules and SO_4^{2-} anions from the Zn^{2+} solvation shell. This rapid desolvation facilitated uniform Zn^{2+} flux and smoother nucleation. The enhanced behavior was attributed to the HA polymer's strong interaction with water *via* hydrogen bonding and its negatively charged groups, which collectively weakened the Zn^{2+}–H_2O/SO_4^{2-} electrostatic interactions. By promoting efficient ion desolvation and mini- mizing residual coordinated species on the Zn surface, the HA gel electrolyte effectively regulated interfacial ion transport and stabilized Zn deposition. Overall, the hydrogen bonding between HA and water not only facilitated Zn^{2+} desolvation but also contributed to suppressing the OER and exhibited a wider ESW compared with conventional liquid electrolytes. Notably, even under a high cutoff voltage of 2.1 V in full-cell configur-

ations, the system maintained a stable voltage profile over 1000 cycles, which was not achievable with the liquid electrolyte.

In addition to biopolymer-based systems, recent studies have also actively explored synthetic polymer architectures to further regulate hydrogen-bonding interactions and enhance temperature adaptability. In particular, the development of composite gel electrolytes with tunable solvation and bonding interactions presents a promising direction for multifunctional AZIBs. As a representative example, Wei *et al.* reported a multi- functional gel electrolyte tailored for AZIBs.[116] In this system, the gel was synthesized through chemical crosslinking of acryl- amide (AM) and *N,N*′-methylenebisacrylamide (MBA), initiated by ammonium persulfate (APS), to construct a robust 3D

polymer network (Fig. 5d). $ZnSO_4$ (ZS) and glycerol (GL) were also uniformly distributed throughout the matrix to foster hydrogen-bonding interactions. The oxygen atoms in polyacrylamide (PAM) and GL preferentially interacted with H_2O and Zn^{2+}, which disrupted native H_2O–H_2O and H_2O–Zn^{2+} coordination. The restructured hydrogen-bonding environment reduced free water activity, suppressed the OER, and improved thermal resilience over a temperature range from −20 to 60 °C. After long-term cycling, Zn foil retrieved from the hydrogel electrolyte showed a smooth surface with a maximum height of only 11.4 μm (Fig. 5e). In contrast, the Zn foil after cycling in the conventional aqueous electrolyte developed dense dendrites over 146.9 μm (Fig. 5f). The suppression of dendrite growth originates from two key mechanisms. First, the 3D gel provides directional ionic channels that facilitate Zn^{2+} transport. Second, the strong affinity between Zn^{2+} and the PAM/GL matrix confines lateral diffusion, guiding uniform Zn deposition.

Although numerous studies have pursued similar approaches, side reactions induced by water are still prevalent in hydrogel-based electrolytes. To address this persistent challenge, an alternative strategy involving a lean-water hydrogel design has been proposed. In this context, Wang et al. developed a zwitterion hydrogel electrolyte system (ZIG) that significantly reduced water content while retaining ionic conductivity and mechanical integrity.[111] Unlike typical PAA or PAM-based hydrogel electrolytes, ZIG demonstrated appreciably advanced electrochemical stability as the water content was reduced from 60 wt% to 20 wt%. Fig. 5g reveals a markedly expanded ESW, with stable cell operation sustained up to approximately 2.1 V. The behavior was attributed to the strengthened O–H covalent interactions under reduced hydration conditions. The ZIG-20 wt% system, when applied to Zn||MnHCF full cells, exhibited excellent rate performance ranging from 48 to 92 mAh g^{-1} (15 C to 1 C). This result was attributed to sustained ionic conductivity under low-hydration conditions

(Fig. 5h). Beyond electrochemical performance, ZIG also exhibited outstanding mechanical resilience under shear stress, a key parameter for flexible electronics (Fig. 5i). The ZIG-20 wt% cell preserved 90% of its capacity under 71 kPa of shear stress, whereas the ZIG-60 wt% device failed completely at only 13 kPa due to interfacial detachment. The difference demonstrated the strong adhesion and mechanical adaptability of low-water-content hydrogel electrolytes, which are suitable for use in deformable and wearable energy storage systems.

Driven by accelerating development of flexible and wearable electronics, gel and solid-state electrolytes have garnered significant attention as next-generation components for AZIBs. The semi-solid nature not only addresses safety concerns such as leakage but also offers the structural flexibility required for device-level integration. Despite this progress, several intrinsic limitations remain. Issues such as insufficient ionic conductivity, limited thermal tolerance, and inadequate mechanical strength continue to restrict the broader adoption of these materials in real-world applications.[117] To realize the full potential of gel and solid-state electrolytes in advanced AZIBs, future studies must focus on systematically improving ion transport, optimizing mechanically compliant frameworks, and stable operation across variable temperatures in addition to earlier strategies. Bridging electrochemical performance with the strategies will be the key to transforming gel-based electrolytes from promising concepts into practical energy storage solutions.

In the preceding discussion, strategies to expand the ESW of electrolytes have been examined through various approaches including co-solvents, DESs, additives, and GPEs. The studies discussed above are summarized in Table 1. As shown here, electrolytes play a critical role in determining the energy density of AZIBs, and considerable progress has been made in recent years to enhance electrochemical stability, ion transport, and interfacial compatibility. While these advances

Table 1 Electrolyte development strategies for high-energy-density AZIBs

Strategy	Materials	Composition	ESW (V vs. Zn/Zn^{2+})	Ref.
Co-solvent	Tetramethylene glycol (TG4)	1 m Zn(OTf)$_2$ with 50 vol% TG4	−0.20–2.53^a	84
	Hexafluoro-2-propanol (HFIP)	3 M Zn(OTf)$_2$ with 30 vol% HFIP	−0.04–2.5^a	85
	N,N-Dimethylacetamide (DMAC) + trimethyl phosphate (TMP)	1 M Zn(OTf)$_2$ with 50 vol% DMAC + 20 vol% TMP + 30 vol% water	−0.043–3.47^b	86
DES	Sulfolane	2 m Zn(OTf)$_2$ with 70 wt% solfolane + 30 wt% water	−0.10–2.75^c	89
	Tetramethylene sulfone (TMS) (= sulfolane)	2 M Zn(OTf)$_2$ with 50 mol% TMS + 50 mol% water	−1.0–3.3^a	90
	Ethylene glycol (EG)	Zn(OTf)$_2$: EG (1 : 6, molar ratio) + 30 vol% water	−0.15–2.6^d	91
	Diethyl phosphoramidate (DEPA)	Zn(TFSI)$_2$: DEPA (1 : 10, molar ratio)	−0.30–2.85^e	92
Additive	SrTiO$_3$	2 M ZnSO$_4$ + 50 wt% SrTiO$_3$	−0.083–2.32^a	101
	Dextran	1 m Zn(OTf)$_2$ + 50 mg mL^{-1} dextran	~2.66^e	106
	Trehalose	2 M ZnSO$_4$ + 100 mM trehalose	−0.087–2.38^a	105
	N,N-Methylenebis(acrylamide)	1 M ZnSO$_4$ + 20 mM N,N-methylenebis(acrylamide)	−0.13–2.6^a	103
	Poly(acrylamide-co-methyl acrylate) (APA)	3 M Zn(OTf)$_2$ + 1 wt% APA	−0.155–2.72^e	107

Current conditions for cycling tests. ^{a} 1 mA. ^{b} 0.002 mA. ^{c} 0.025 mA. ^{d} 0.1 mA cm^{-2}. ^{e} 1 mA cm^{-2}.

have led to significantly improved performance, further innovations are required to meet the demands of next-generation battery systems. Several key perspectives are proposed here to guide future electrolyte development.

Despite the growing number of electrolyte systems demonstrating excellent electrochemical performance, many of these results are achieved under high N/P ratios. Such conditions, although beneficial for demonstrating a wide ESW, do not contribute meaningfully to practical volumetric or gravimetric energy densities. Future research must focus on developing electrolyte formulations that support stable operation under low N/P configurations. In addition, achieving reliable cell performance under lean electrolyte conditions, where electrolyte volume is minimized to reflect practical device packaging, is also essential for realizing high-energy-density in real systems. Another critical challenge in electrolyte research is the lack of electrolyte systems that have been properly paired with high-voltage cathodes. While considerable efforts have improved the cathodic stability of aqueous electrolytes, studies evaluating compatibility with high-voltage cathode materials under full-cell configurations remain scarce. Understanding the practical feasibility of these systems requires pairing with high-voltage cathodes to be tested directly at the device level, where interfacial stability, redox kinetics, and side reactions can be systematically assessed. Finally, the economic aspect must also be carefully considered when modifying electrolytes. In particular, when large amounts of additional components are employed, strategies should be continuously devised to achieve improved electrochemical performance without undermining the inherent cost advantage of AZIBs. Such consideration represents one of the essential directions to simultaneously realize high energy density and practical commercialization of AZIBs.

4. Maximizing Zn utilization through deep-discharge anode design

Metallic Zn has been regarded as the most promising anode material for AZIBs, owing to its low redox potential (-0.76 V vs. standard hydrogen electrode) and high gravimetric and volumetric capacities (820 mAh g^{-1} and 5855 mAh cm^{-3}, respectively).[118–120] However, the direct employment of Zn metal introduces challenges related to dendritic growth and irreversible zinc loss during repeated cycling, which often necessitates the use of thick Zn foils or even powders to maintain electrochemical stability. Since Zn stores energy through surface conversion reactions, a substantial portion of excess Zn remains electrochemically inactive, thereby reducing the overall energy density of the cell. Typically, the areal capacity (Q_a) of Zn anode can be calculated using the following equation:

$$Q_a\left(\mathrm{mAh\,cm^{-2}}\right) = \frac{nF\rho l}{3.6M} \tag{1}$$

where n is the number of electrons (2 for Zn), F is the Faraday constant (96 500 C mol^{-1}), ρ is the density of Zn (7.14 g cm^{-3}), l is the thickness of the Zn anode (cm), and M is the molar

mass of Zn (65.4 g mol^{-1}). Based on eqn (1), a Zn anode with a thickness of 1.71 μm delivers a theoretical areal capacity of 1 mAh cm^{-2}. However, since conventional Zn foils used in electrochemical tests are often tens of micrometers thick, only a small portion of Zn is electrochemically utilized and a large excess fraction remains unreacted.

As a result, the depth of discharge (DOD), which represents the extent to which the anode is utilized within a given cell, has become a critical factor in evaluating the energy optimization of AZIBs that employ Zn metal as the anode active material. DOD can be calculated using the cell capacity and overall capacity of the metallic anode, expressed as:

$$\mathrm{DOD}\,(\%) = \frac{x}{Q_a} \tag{2}$$

where x denotes the areal capacity of the full cell (mAh cm^{-2}). According to eqn (1) and (2), increasing the DOD by reducing the anode thickness or maximizing the electrochemical utilization of Zn significantly contributes to raising the practical energy density. A high DOD indicates efficient use of Zn, allowing more energy to be stored per unit mass and volume. In practical AZIB configurations, however, achieving high DOD poses a significant issue due to hurdles such as poor reversibility and dendrite formation, which are exacerbated under lean-Zn conditions.[33,121] In this section, recent efforts toward designing high-DOD Zn anodes are discussed, with emphasis on reducing electrochemically inactive Zn and achieving high-energy-density AZIBs.

4.1 Constructing artificial protective layers

Constructing artificial protective layers on Zn anodes is one of the most practical and scalable approaches for mitigating dendritic growth and interfacial degradation because they are simple to fabricate, cost-effective to produce, and easy to implement in real systems.[122–124] The introduced layers serve as ion-conductive yet protective barriers that regulate Zn^{2+} transport and promote spatial uniformity in the local electric field, leading to homogeneous Zn deposition and suppressed side reactions.[125] Importantly, the interfacial layer plays a crucial role in improving anode reversibility and stabilizing the electrochemical environment since charge transfer reactions occur primarily at the electrode–electrolyte interface. Moreover, the structural and chemical design of the interfacial layer can be tailored to modulate structural robustness and surface characteristics, including interfacial energy and ion-binding affinity, which supports stable operation under high DOD conditions.[126,127]

From a materials design perspective, artificial interfacial layers should satisfy stringent requirements to ensure the stable operation of Zn metal anodes. At the structural level, sufficient elastic modulus and mechanical durability are needed to resist dendritic intrusion and withstand the stresses associated with Zn plating and stripping. In parallel, mechanical adaptability is required to accommodate dynamic volume changes and respond to spatially uneven morphological evolution during cycling. On the electrochemical side, electro-

chemical functionality demands both high Zn^{2+} conductivity to facilitate ion transport and limited electronic conductivity to prevent uncontrolled Zn deposition.[128] Uniform ion conduction pathways are also advantageous for eliminating localized flux and minimizing issues originating from the tip effect. Additionally, long-term operation in aqueous electrolytes necessitates strong chemical and electrochemical stability to avoid dissolution, side reactions, and interphase degradation.

Among various artificial interfacial designs, organic coatings like poly(2-vinylpyridine), xanthan gum, poly(vinylidene fluoride-trifluoroethylene), polypyrrole, and specific porous organic polymers, offer several distinct advantages.[129–133] Their inherently flexible and conformal architectures allow them to endure repeated mechanical deformation without fracture.[134,135] Functional groups within the polymeric matrix can interact selectively with Zn-ions, promoting uniform ion distribution and deterring localized nucleation. For instance, a hydrophobic organic protective layer based on poly(tetrafluoroethylene)-derived carbon, denoted as $(C_2F_4)_n$–C, was introduced to improve anode reversibility by physically isolating the metal surface, using vacuum-evaporated PTFE onto a Cu substrate.[136] Accordingly, three types of electrodes were prepared to examine the surface regulatory effects of the protective layer: a bare Zn electrode with 20 μm thickness (20 μm-Zn), a Zn-deposited Cu foil without surface modification (Cu@Zn), and a Zn-deposited Cu foil coated with carbon $((C_2F_4)_n$–C@Cu@Zn). As illustrated in Fig. 6a, the fluorine-rich carbon layer blocked water molecules through strong hydrophobicity and inhibited side reactions. Zn^{2+} were directed beneath the interfacial layer rather than depositing on the outer surface, guided by zincophilic fluorine embedded in the semi-ionic C–F framework. Scanning electron microscopy (SEM) images revealed that Zn deposited as a dense and compact layer on the coated electrode, whereas the uncoated Cu@Zn showed a loosely packed and porous structure. As a result, the $(C_2F_4)_n$–C@Cu@Zn electrode demonstrated stable cycling under a high DOD of 40%, maintaining a prolonged lifetime exceeding 900 h at a current density of 5 mA cm^{-2}. The stable performance was further corroborated by Raman spectroscopy after 20 cycles, which revealed no detectable side reaction products on the coated electrode, whereas the uncoated electrodes exhibited strong signals corresponding to insulating byproducts (Fig. 6b).

Meanwhile, inorganic protective layers such as TiO_2, ZnF_2, silicon nitride, and layered double oxide offer excellent chemical durability and mechanical stiffness, as a high elastic modulus effectively suppresses dendritic growth by limiting deformation and physically blocking protrusions.[137–142] Zn^{2+}-conducting structures in specific inorganic compounds additionally facilitate directional ion transport across the interface and promote uniform Zn deposition.[143] Microscale porosity commonly observed in inorganic coatings, however, reduces the electrode isolation from aqueous electrolytes and hinders the suppression of parasitic reactions.[144] The intrinsic rigidity of inorganic materials also limits accommodation of morphological changes during Zn plating and stripping. Taken together, integrating inorganic components with organic polymers to form hybrid interfacial layers provides an effective strategy to combine structural robustness and ion-transporting capability with improved mechanical adaptability and interfacial integrity.

Recently, Gan et al. developed a hybrid interfacial layer using a zeolitic imidazolate framework (ZIF-8).[145] The hybrid structure, referred to as ZGL, was constructed by integrating ZIF-8-decorated graphene oxide (GO) support and a PVDF binder, isolating the anode interface and merging the ion-coordinating ability of ZIF-8 with the robust interfacial adhesion. As shown in Fig. 6c, cross-sectional SEM and energy-dispersive X-ray spectroscopy (EDS) mapping demonstrated a stratified configuration in the ZGL layer, where carbon, nitrogen, and fluorine elements were predominantly distributed in the upper region. The compositional distribution effectively isolated the underlying Zn from direct contact with the aqueous electrolyte while enabling directional Zn^{2+} transport across the interface. Binding energy analysis revealed that Zn atoms preferentially adsorbed onto ZIF-8, suggesting stronger Zn^{2+} affinity that facilitated efficient desolvation and uniform distribution. A substantially higher ionic conductivity was also measured in ZGL compared with PVDF, attributed to the improved ion transporting properties. Consequently, the ZGL@Zn cell demonstrated markedly improved cycling performance under a high DOD of 42.7% at 5 mAh cm^{-2}, maintaining stable operation over 500 h, which was attributed to the combined effects of interfacial shielding and regulated ion flux within the hybrid matrix (Fig. 6d). Confocal laser scanning microscopy (CLSM) further clarified the origin of anode durability, where the ZGL-protected electrode exhibited a reduced vertical height variation of 11.1 μm compared with 43.0 μm in the bare Zn, indicating homogeneous surface evolution and more uniform Zn utilization behaviors under high DOD conditions.

The incorporation of zincophilic metal particles has been widely explored to improve Zn^{2+} adsorption and regulate nucleation behavior, thereby enhancing the reversibility of Zn metal anodes. Wang and co-workers introduced Cu atoms into a polymeric carbon nitride (PCN) matrix to form a multifunctional Cu@PCN interfacial layer.[146] The embedded Cu atoms provided strong Zn^{2+} affinity and promoted directional Zn deposition while concurrently inhibiting parasitic reactions (Fig. 6e). The resulting coated layers exhibited both zincophilic and hydrophobic characteristics, enabling selective Zn^{2+} migration and preventing water permeation at the interface. Additionally, local current concentration was alleviated by the charge redistribution effect of the Cu@PCN layer, which fostered uniform deposition. Notably, Cu@PCN guided Zn anode to grow preferentially directing the (101) crystal plane, as supported by DFT calculations (Fig. 6f). The surface energy of Zn on the (101) plane was calculated to be lower than that on the (002) plane, suggesting thermodynamically favored growth. Furthermore, binding energy analysis confirmed that Zn atoms interacted more strongly with the (101) surface (−0.64 eV) than with the (002) surface (−0.37 eV), reinforcing the selective plating tendency induced by the interfacial layer. The
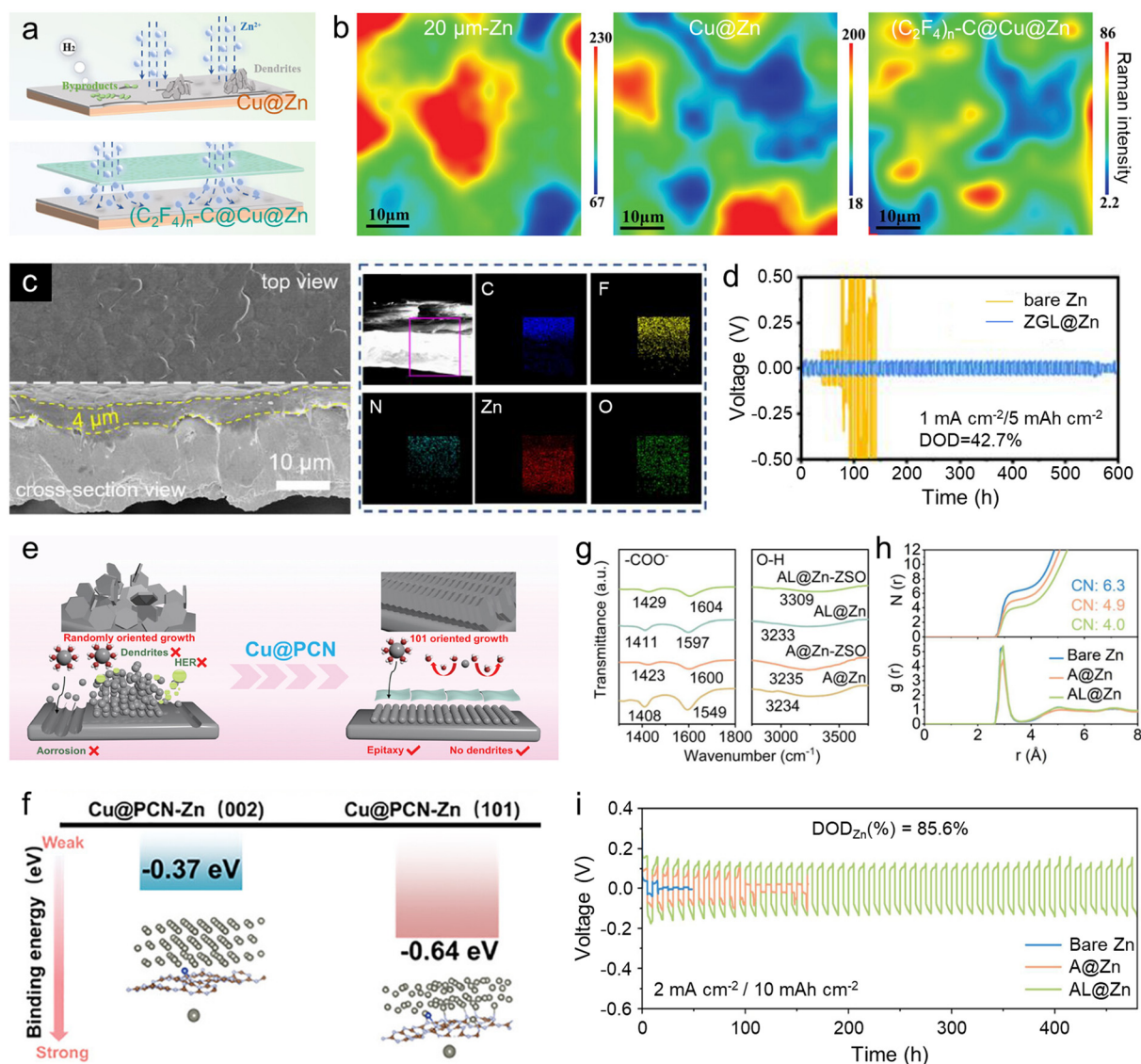
Fig. 6 Artificial interface layer-enabled stabilization strategies for Zn anodes. (a) Schematic illustration of Zn deposition mechanisms depending on the type of protective layer applied to the Zn anode. (b) Raman mapping of 20 μm-Zn, Cu@Zn, and $(C_2F_4)-C@Cu@Zn$ anodes after 50 cycles. Reproduced with permission from ref. 136. Copyright 2023, Wiley-VCH. (c) Cross-sectional SEM image and corresponding EDS mapping of the ZGL-coated Zn anode. (d) Long-term cycling performance of bare Zn and ZGL@Zn symmetric cells at an areal capacity of 5 mAh cm^{-2} under a current density of 1 mA cm^{-2}. Reproduced with permission from ref. 145. Copyright 2022, Elsevier. (e) Schematic illustrations of Zn plating behavior on bare Zn and Cu@PCN-Zn electrodes. (f) Calculated binding energies between Zn atoms and Zn (101) and Zn (002) planes with the Cu@PCN coating. Reproduced with permission from ref. 146. Copyright 2024, Wiley-VCH. (g) FTIR spectra of A@Zn and AL@Zn before and after ZSO uptake. (h) Simulated radial distribution functions and coordination environment of Zn^{2+} in ZSO solution. (i) Cycling performance of Zn‖Zn symmetric cells at a current density of 2 mA cm^{-2} and an areal capacity of 10 mAh cm^{-2}. Reproduced with permission from ref. 147. Copyright 2025, American Chemical Society.

multifunctionality of Cu@PCN was further validated by Tafel plots and LSV analyses, both of which revealed enhanced resistance to side reactions. Together, these findings highlight the effectiveness of the interfacial layer in enhancing Zn^{2+} transport and improving interfacial robustness under aqueous conditions.

To further enhance interfacial regulation, inorganic materials with strong Zn^{2+} affinity have been employed to construct artificial interfacial layers. As an example, a hybrid interfacial layer composed of alginic acid (AA) and lithium mag-

nesium silicate (LMS) platelets was proposed, inspired by the selective ion transport characteristics of cytomembranes.[147] The integrated architecture established ion-conducting channels that enabled preferential Zn^{2+} migration, which facilitated rapid charge transfer and promoted uniform plating. To examine interfacial interactions, the evolution of –COO$^-$ stretching peak was monitored using Zn electrodes modified with either the AA-LMS composite (AL@Zn) or AA alone (A@Zn). FTIR spectra in Fig. 6g displayed a notable redshift in AL@Zn compared with A@Zn, suggesting coordination

between –COO⁻ groups in AA and LMS platelets. Moreover, exposure to 2 M ZnSO₄ aqueous electrolyte (ZSO) led to a further shift in the –COO⁻ peak regardless of the coating layer composition, which confirmed selective Zn^{2+} interactions with both AA and LMS. The resultant dual coordination contributed to the immobilization of absorbed water, as evidenced by reduced O–H vibrational signals, which reflected a lower population of free water and suppression of interfacial side reactions. Computational analysis results revealed that the coordination number (CN) of Zn^{2+} decreased from 6.3 for bare Zn to 4.9 and 4.0 for A@Zn and AL@Zn, respectively, reflecting that water molecules were substituted by AA or LMS through electrostatic interactions (Fig. 6h). As a result, symmetric cells employing AL@Zn anodes retained stable cycling over 450 h under a high DOD of 85.6%, and this performance corroborates the role played by the hybrid layer in enabling Zn^{2+} selectivity and regulating free water (Fig. 6i).

Introducing artificial interfacial layers represents a simple yet tunable strategy to improve Zn anode reversibility by leveraging the distinct functionalities of various materials to regulate water and ion transport in aqueous electrolytes. For the development of high-energy-density AZIBs, it is recommended to consider the following aspects in designing interfacial coatings from the perspective of anode optimization. First, since the protective layer does not directly contribute to energy storage, it must remain sufficiently thin. Considering that the thinnest commercially available Zn foil is 5 μm thick, the additional layer should be no thicker than 5 μm. To meet this requirement, the coating must maintain structural robustness during cycling and provide puncture resistance without compromising mechanical integrity. Designing elastic or even stretchable polymer-based coatings is therefore desirable to accommodate volume changes and suppress dendritic growth in ultrathin configurations. In addition, maintaining performance with a minimal anode inventory through the use of a protective layer is also an important direction. For instance, Cho et al. reported a single-walled CNT-coated Cu substrate (CNT@Cu) that functioned as a nearly anode-free system.[148] In that study, only 1 mAh cm⁻² of Zn was deposited on CNT@Cu and then used in an AZIB full cell. Although reducing the anode content generally increases the overall energy density, the amount of Zn that can be reversibly cycled becomes extremely limited, which compromises long-term operation. By contrast, the protective layer in this work enabled more stable electrochemical behavior than bare Zn foil over extended cycling, highlighting the broader applicability of protective-layer engineering. Meanwhile, detailed analysis of ion behavior within the protective layer is expected to uncover further opportunities for enhancing anode performance. Although considerable efforts have been devoted to understanding the interactions between Zn^{2+} ions and the coating matrix, deeper insights into the underlying mechanisms may unlock new strategies for interface engineering. Moreover, the transport behavior of SO_4^{2-} and H^+ ions, which are often overlooked in comparison with Zn^{2+}, should also be carefully considered. Elucidating their migration patterns and developing coatings

that selectively restrict their transport will enable the design of interfacial layers with elevated Zn^{2+} transference numbers, offering a promising avenue for improving the reversibility of Zn metal anodes.

4.2 Deposition modulation using additives

Electrolyte additives have emerged as an effective and versatile strategy to enhance the reversibility and morphological stability of Zn metal anodes.[149,150] Since the electrolyte directly affects Zn^{2+} transport and interfacial reaction behavior, its local tuning through additives plays a critical role in determining anode utilization and electrochemical reversibility. By modulating the local chemical environment without altering the bulk cell architecture, additives influence various interfacial phenomena such as Zn nucleation, growth kinetics, and parasitic reactions.[151–153] Moreover, solution-phase modifications are particularly attractive due to their design flexibility, ease of implementation, and broad compatibility with different cell chemistries.[154,155] A diverse range of additives, including metal cations and organic molecules, have been investigated to control Zn plating behavior, leading to extended cycle life under practical conditions. As a result, a comprehensive understanding of how additives regulate interfacial stability and ion transport is essential to fully exploit their potential in high-performance AZIBs.

Cationic salt-modified electrolytes are formulated by dissolving water-soluble ionic compounds into aqueous media, enabling the electrochemical behavior to be modulated according to the ionic radius, valency, and coordination characteristics of the introduced cations.[156] As viable additive candidates NH_4^+, Li^+, Na^+, Mg^{2+}, La^{3+}, and Bi^{3+} have been employed as cationic species that contribute to interfacial ionic regulation and Zn plating stabilization.[157–162] One primary mechanism responsible for deposition stabilization is the electrostatic shielding effect induced by inert cations that accumulate at the electrode surface.[1] The introduced cations have a reduction potential lower than the redox potential of Zn^{2+} and therefore remain electrochemically inactive near the surface, where they repel incoming Zn^{2+} via coulombic interactions. As a result, the "tip effect", in which charge concentrates and accelerates dendritic growth at the protrusions, is alleviated and Zn deposits laterally. Additionally, cationic additives confined within the electric double layer (EDL) reconstruct the local electric field distribution and effectively mitigate the field gradient, which in turn regulates Zn^{2+} flux and facilitates dense, guided metal deposition.[163,164]

Zhao et al. employed $La(NO_3)_3$ as a cationic additive to weaken the repulsive force between Zn deposits on the electrode surface and to modify the EDL environment.[161] The $La(NO_3)_3$-modified $ZnSO_4$ electrolyte (La^{3+}–ZS) yielded a dense Zn morphology after cycling by reducing inter-deposit repulsion and suppressing the formation of electrically isolated dead Zn, thereby supporting stable anode utilization. Zeta potential measurements revealed that Zn flakes in the pristine $ZnSO_4$ electrolyte exhibited a potential of −4.4 mV, indicating a negatively charged anode surface. In comparison, when

La^{3+}–ZS was used, the zeta potential increased to −0.7 mV, indicating a reduced net surface charge that is critical to changes in electrochemical behavior induced by the cationic additive. Schematic illustrations of the EDL structures under different electrolyte conditions in Fig. 7a clarify the underlying mechanism governing La^{3+}-induced deposition behavior. In aqueous media, both Zn^{2+} and La^{3+} competitively adsorb on the Zn surface. However, the net surface charge is lower in the presence of trivalent La^{3+}, which compresses the EDL and mitigates electrostatic repulsion between Zn deposits (Fig. 7b). Consequently, Zn nuclei are allowed to grow in closer proximity, enhancing interfacial cohesion and enabling them to pile up along the c-axis with improved structural alignment,

while the ZnSO$_4$-based electrode suffers from spatially separated Zn deposits with a loosely packed morphology. Benefitting from the EDL manipulation, the Zn||Zn symmetric cell could achieve stable cycling even under a high DOD of 80% with an areal capacity of 5.9 mAh cm^{-2}.

Meanwhile, organic additives, including hydrocarbon derivatives, sulfones, and amides, have also been widely employed in AZIBs to suppress dendritic growth and enhance anode reversibility.[165] Similar to cationic additives, these molecules adsorb onto the electrode surface to regulate Zn deposition behavior and suppress parasitic reactions.[40] Notably, when bulky additives preferentially bind to specific Zn crystal planes, deposition occurs along a favored orientation, which
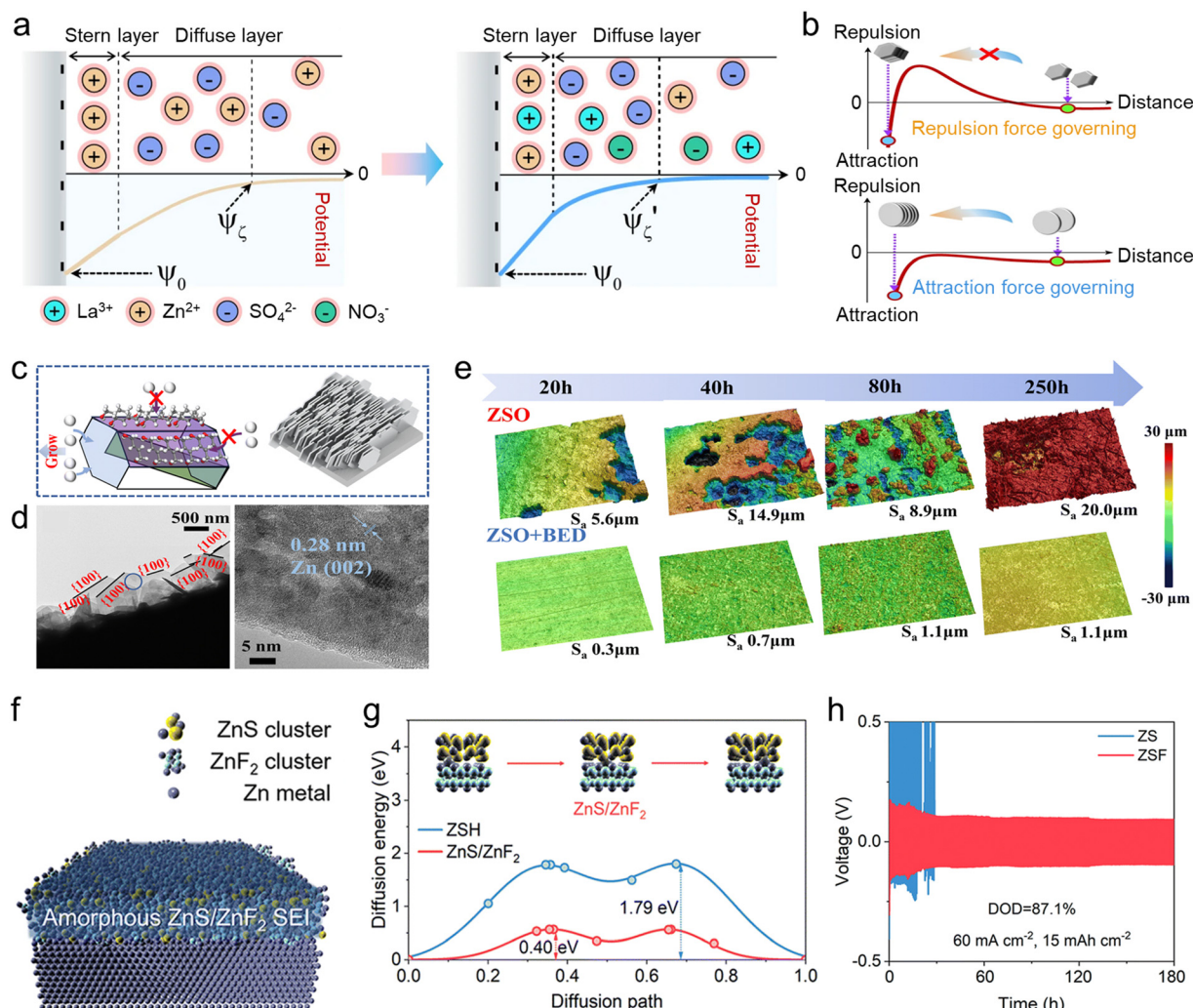

Fig. 7 Zn anode stabilization strategies based on additive-assisted electrolytes. (a) Comparison of the electric double layer formed by Zn deposits in ZS and La^{3+}-ZS electrolytes. (b) Proposed growth models of Zn deposits in ZS (top) and La^{3+}-ZS (bottom) electrolytes. Reproduced with permission from ref. 161. Copyright 2022, Springer Nature. (c) Schematic diagram illustrating the deposition mechanism in the ZSO + BED electrolyte. (d) TEM images of early-stage Zn deposition in the ZSO and ZSO + BED electrolyte. (e) CLSM images of Zn anodes after cycling in ZSO and ZSO + BED electrolytes. Reproduced with permission from ref. 168. Copyright 2025, The Royal Society of Chemistry. (f) Schematic illustration of the amorphous hybrid ZnS/ZnF$_2$-rich SEI layer on the Zn anode. (g) Calculated diffusion energy barriers of Zn^{2+} at various interfaces. (h) Galvanostatic Zn plating/stripping behavior in Zn||Zn symmetric cells at a current density of 60 mA cm^{-2} and an areal capacity of 15 mAh cm^{-2}. Reproduced with permission from ref. 169. Copyright 2025, The Royal Society of Chemistry.

promotes uniform growth, suppresses uncontrolled surface area expansion, and minimizes electrically isolated zinc, improving anode reversibility. Among the various crystallographic orientations, the (002) close-packed plane is typically preferred due to its low surface energy and its ability to drive ordered and densely stacked Zn deposition, ultimately leading to a dendrite-free morphology.[166,167] Wang's group found that sodium 3-mercapto-1-propanesulfonate (MPS) is an effective organic additive for suppressing dendritic growth and parasitic reactions.[98] The sulfonate moiety in the MPS anion exhibits strong affinity toward the Zn anode, which enables preferential adsorption at the electrode surface. Notably, the sodium cation in MPS exerts minimal influence, and the presence of MPS barely alters the Zn^{2+} solvation structure, indicating that the enhancement in electrochemical performance is primarily attributed to interfacial adsorption of the additive. DFT calculations revealed that the MPS anion preferentially adsorbs on the (100) and (101) planes of Zn, with adsorption energies of −4.70 and −4.58 eV, respectively, while the (002) plane exhibits a weaker adsorption energy of −3.24 eV. The selective surface occupation of MPS implies that the (002) plane remains relatively available for hydrated Zn^{2+} adsorption, facilitating preferred zinc growth on the (002) facet. In support of this, the adsorption energy of hydrated Zn^{2+} on the (002) plane increases markedly from −2.23 to −4.17 eV after MPS adsorption, suggesting enhanced Zn^{2+} stabilization. Collectively, these findings corroborate that Zn deposition proceeds more readily and in a directionally regulated manner.

In addition, Ren *et al.* introduced an organic additive that encourages exposure of the (100) plane and mitigates the inherently slower crystal growth rate of the (002) facet as well as its associated inefficiency during the stripping process.[168] Notably, 2-butene-1,4-diol (BED) adsorbs onto the Zn surface during deposition but subsequently detaches during stripping, which allows unobstructed Zn^{2+} transfer and enhances the reversibility of the Zn anode. The incorporation of 150 mM BED into the aqueous electrolyte enabled stable cycling at a high DOD of 67.7% and an areal capacity of 40 mAh cm^{-2}, while concurrently suppressing dendrite formation and inhibiting corrosion. Surface adsorption studies revealed that BED exhibits a significantly stronger affinity for the (100) plane than for the (002) or (101) planes, leading to preferential binding at the former. The guided adsorption behavior hinders Zn^{2+} deposition onto the (100) plane and maintains dominant exposure of the (100) plane, which subsequently directs Zn growth along a defined orientation and yields a well-ordered array of zinc plates with uniform morphology (Fig. 7c). Transmission electron microscopy (TEM) of the initial deposits confirmed that the inner domains were composed of (002)-oriented hexagonal crystals, whereas the outer regions were preferentially exposing (100) planes (Fig. 7d). Meanwhile, hydrated Zn^{2+} species coordinated by six water molecules induce severe side reactions and cause corrosion at the anode interface in conventional aqueous ZnSO₄ (ZSO) electrolytes. By contrast, BED contains a C=C bond with strong electronegativity that interacts with Zn^{2+}, modulates the local

solvation structure, and results in improved corrosion resistance. In addition, BED suppresses the adsorption of water molecules at the anode surface, a process that reduces the likelihood of the Volmer step in the hydrogen evolution reaction and limits direct water contact with zinc. Consequently, as illustrated in Fig. 7e, the BED-containing electrolyte (ZSO + BED) effectively mitigated surface degradation caused by dendrite formation and side reactions, and preserved a smooth Zn surface morphology throughout a continuous cycling.

Meanwhile, from the perspective of electrolyte formulation, the use of additives that promote the *in situ* formation of structurally robust SEI layers with strong affinity for the Zn anode and improved ion transport is an effective strategy for interface stabilization. For instance, Zeng and co-workers examined the influence of additives on SEI formation in 2 M ZnSO₄-based AZIBs.[169] The introduction of 80 mM Zn(CF₃COO)₂ led to the formation of an inorganic SEI layer composed of both ZnS and ZnF₂, where CF₃COO⁻ reorganizes the hydrogen-bonding network of water molecules, thereby lowering water activity and suppressing HER (Fig. 7f). XPS analysis of Zn 2p spectra after 100 cycles revealed that the baseline ZnSO₄ (ZS) electrolyte generated pronounced Zn–OH signals associated with Zn₄SO₄(OH)₆·5H₂O (ZSH) by-products. In contrast, the electrode cycled in the ZSF electrolyte exhibited negligible Zn–OH peaks, which suggests the formation of an SEI layer enriched in ZnS and ZnF₂. In typical ZnSO₄ electrolytes, participation of SO_4^{2-} in electrochemical reaction is limited because the H₂O–Zn^{2+}–H₂O coordination structure hinders its incorporation into the solvation shell. Despite its exclusion from the primary coordination shell, SO_4^{2-} retains a low LUMO energy level in the solvated state and remains readily reducible. CF₃COO⁻ forms strong hydrogen bonds with water, weakening the Zn^{2+}–H₂O interaction and allowing SO_4^{2-} to enter the primary solvation shell, where it can participate in SEI formation. Moreover, CF₃COO⁻ itself can be incorporated into the solvation structure and contribute to ZnF₂ formation *via* electrochemical reduction. The resulting ZnS/ZnF₂-rich SEI facilitates desolvation and provides a lower diffusion energy barrier for Zn^{2+} transport compared with the ZSH-dominated interphase (Fig. 7g). As a result, the ZSF electrolyte supported the formation of a stable SEI layer, improved Zn anode reversibility, and enabled long-term cycling in symmetric Zn||Zn cells under high DOD conditions of 87.1% (15 mAh cm^{-2}) at a current density of 60 mA cm^{-2} (Fig. 7h).

The introduction of electrolyte additives represents a simple yet versatile strategy for enhancing AZIB performance. Owing to their negligible volume and weight contributions, such additives can be employed without significantly affecting the energy density. To date, various approaches have been developed for improving anode stability, including cationic salts for regulating Zn deposition, organic and anionic compounds for modifying solvation structures and directing crystal growth, and additives that facilitate *in situ* SEI formation. However, the rational design of electrolyte additives must consider not only interfacial functionality but also environmental compatibility and cost-effectiveness. Certain

cationic salts and other chemical additives, when released into aqueous environments, may pose ecological risks. In addition, relatively high concentrations are sometimes required to achieve the desired interfacial effects, which raises concerns regarding both sustainability and scalability. Balancing electrochemical performance with environmental and economic factors is therefore essential. To address these issues, several eco-friendly and cost-efficient additives have been proposed. For instance, Wang et al. utilized a biocompatible additive that ensured renewability and non-toxicity, preserving the fundamental advantages of AZIBs.[170] Li et al. employed maleic anhydride (MA) as a low-cost additive that formed hydrogen bond networks with water molecules to reduce water activity and simultaneously adsorbed onto Zn surfaces to promote uniform metal deposition.[171] Similarly, Chen's group introduced cellulose nanocrystals (CNCs), a widely available bio-based material, to reconstruct the solvation structure and reinforce interfacial chemistry, thereby improving Zn-ion mobility and deposition uniformity.[172] The practical viability of additives in large-area configurations is another key consideration. Unlike coin-type cells, practical battery systems involve larger electrode areas and more complex geometries, which can result in non-uniform ion transport. Therefore, evaluating the reproducibility and spatial uniformity of additive-assisted Zn deposition under realistic operating conditions is essential for confirming their practical applicability.

4.3 Surface engineering strategies

In addition to strategies involving protective interfacial layers or electrolyte engineering to enhance Zn anode performance, a growing body of research has focused on directly engineering the Zn anode to achieve tailored electrochemical properties. Such approaches are less affected by changes in electrolyte composition or environmental conditions, as they are based on intrinsic modification of the electrode material. Moreover, direct structural tuning of Zn offers a highly intuitive route to improve anode stability, and a variety of methodologies have been developed following this concept. In essence, employing substrates with high interfacial affinity can mitigate crystalline inhomogeneity in subsequent Zn deposits and facilitates uniform Zn growth that leads to stable electrodeposition.[173] Ji et al. investigated the interfacial anisotropy between Zn deposits and underlying substrates, and introduced a Zn-containing alloy layer to regulate the interface.[174] Lattice mismatch (δ) between Zn deposits and the substrate can be classified into incoherent, semi-coherent, and coherent interfaces, where coherent configurations exhibit the lowest δ values. They proposed that incoherent interfaces ($\delta > 0.25$) induce higher nucleation overpotentials, leading to preferential deposition at surface protrusions and inhomogeneous Zn growth. While a coherent interface can, in principle, form between Zn deposits and a Zn substrate, the multi-oriented structure of metallic Zn induces random growth directions, disrupting ideal epitaxial stacking. In contrast, a $CuZn_5$ interfacial layer introduced on the Zn surface exhibits reduced lattice mismatch with the Zn crystalline structure and facilitates ordered and stable epitaxial

stacking. As a result, the interface-engineered electrode achieved a superior electrochemical reversibility in symmetrical cell tests, even under a high DOD level of 85%.

Fundamentally, Zn exhibits distinct characteristics depending on its crystallographic planes, and engineering the electrode to take advantage of the specific properties associated with each plane can help suppress dendrite formation and minimize side reactions. The (002) plane of Zn provides a flat surface that supports epitaxial growth and has low surface energy in its hexagonal structure, a combination that contributes to improved chemical stability. Recently, Cao et al. fabricated a (002)-exposed Zn substrate using a selective chemical polishing (CP) technique based on $(NaPO_3)_6$ as an etchant.[175] The CP process involved immersing the Zn metal in an etchant solution to remove the native passivation layer (e.g., zinc oxide and zinc carbonate), thereby increasing the availability of electrochemically active sites and lowering the charge transfer resistance. Furthermore, the authors eliminated thermodynamically unstable planes except for the (002) plane through the selective etching process, which allowed for ordered metal deposition and reduced surface parasitic reactions. Interestingly, PO_3^- anions interact with the Zn surface in a plane-specific manner. When adsorbed on the (100) or (110) plane, PO_3^- increases the Zn–Zn bond length, producing a strong pulling effect that extracts Zn atoms from the lattice and induces localized corrosion (Fig. 8a). In contrast, PO_3^- adsorption on the (002) plane causes no detectable change in Zn–Zn bond length, indicating that corrosion is suppressed on this surface. The chemically polished Zn (CP-Zn) enabled rapid yet confined two-dimensional Zn^{2+} diffusion under constant bias and significantly restrained dendrite formation compared with bare Zn (Fig. 8b). Electrochemical measurements confirmed that CP-Zn exhibited a lower nucleation overpotential, facilitating easier Zn deposition and promoting in-plane growth guided by dominant (002) exposure. Moreover, the high thermodynamic stability of the (002) plane made the CP-Zn surface more resistant to aqueous corrosion and effectively prevented the formation of $Zn_4SO_4(OH)_6 \cdot 4H_2O$ by-products. As a result, the combined effects of controlled deposition and suppressed side reactions supported stable cycling at a high DOD of 50%, and enhanced long-term performance was also demonstrated in full cells with a VO_2 cathode (Fig. 8c).

In contrast to previous studies that aimed to construct Zn anodes with dominant (002) planes to enhance electrochemical performance, Xu et al. proposed selectively removing the Zn (002) planes, suggesting that (002) is chemically unstable and prone to corrosion in aqueous environments.[176] Upon immersing Zn foils in 2 M $ZnSO_4$ aqueous electrolyte, X-ray diffraction (XRD) analysis detected a marked reduction in the (002) plane intensity, accompanied by the emergence of detrimental zinc hydroxide sulfate phases. By comparison, the (100) and (101) planes remained with hardly any change, which underscores the high chemical reactivity of the (002) plane toward an aqueous electrolyte. To further assess the effect of the (002) elimination, the authors immersed Zn foils in an etching solution and fabricated surface-engineered Zn anodes with minimal
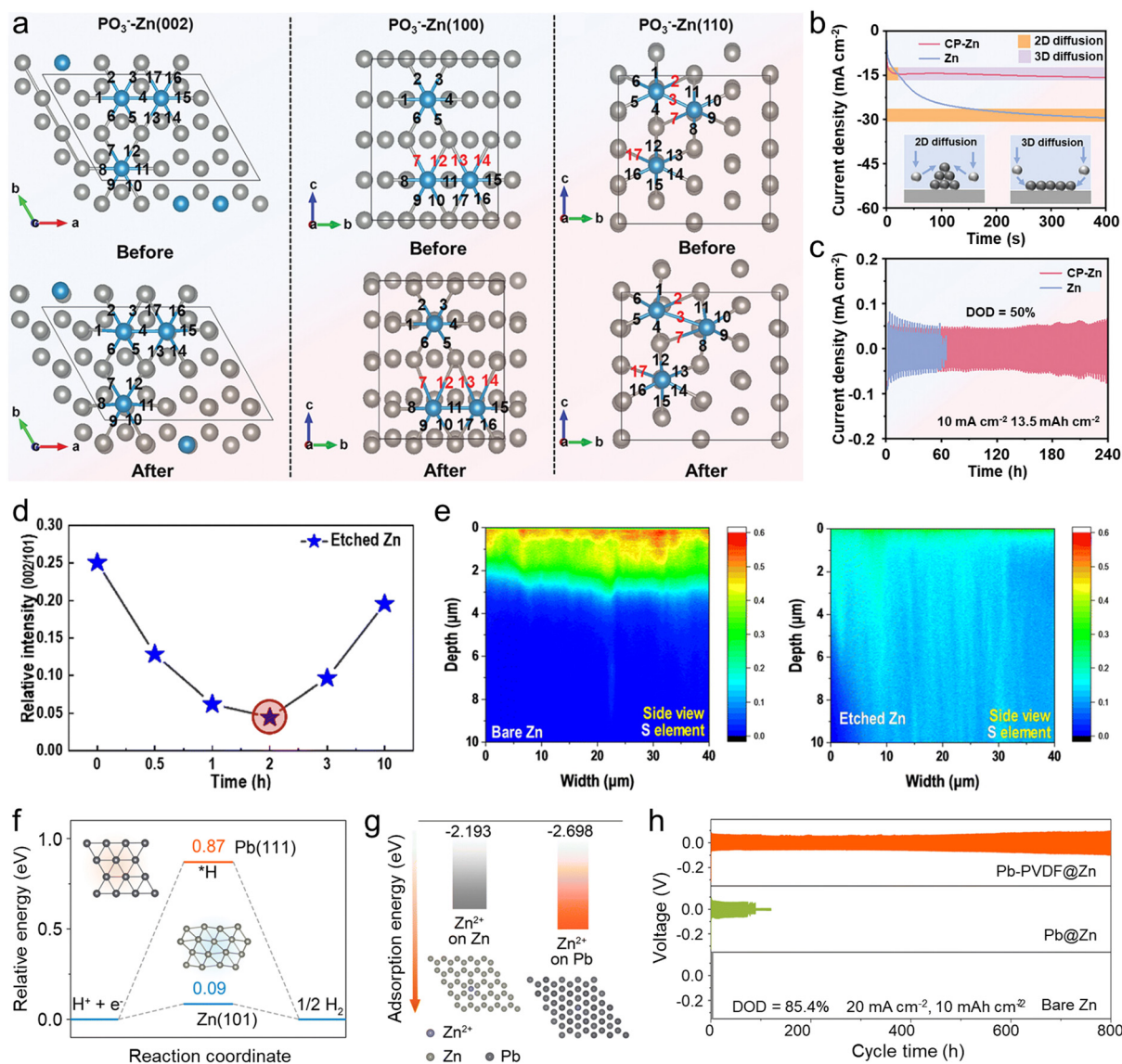
Fig. 8 Zn anode modification strategies for improving reversibility. (a) Atomic configurations before and after the adsorption of PO_3^{3-} on the (002), (100), and (110) crystal planes. (b) Chronoamperometry curves of Zn||Zn and CP-Zn||CP-Zn cells. (c) Cycling performance of CP-Zn and bare Zn electrodes in symmetric cells at a current density of 10 mA cm^{-2} and an areal capacity of 13.5 mAh cm^{-2}. Reproduced with permission from ref. 175. Copyright 2024, Wiley-VCH. (d) (002)/(101) Zn peak intensity ratios of etched Zn foils from XRD patterns obtained at different etching durations. (e) Depth color mapping of S element in cycled bare Zn (left) and cycled etched Zn (right). Reproduced with permission from ref. 176. Copyright 2024, The Royal Society of Chemistry. (f) Calculated Gibbs free energy for hydrogen evolution reaction on Pb and Zn surfaces. (g) Adsorption energies of Zn2 + on Zn and Pb metal surfaces. (h) Deep cycling performance of Pb-PVDF@Zn, Pb@Zn, and bare Zn cells at a current density of 20 mA cm^{-2} and an areal capacity of 10 mAh cm^{-2}. Reproduced with permission from ref. 189. Copyright 2024, The Royal Society of Chemistry.

(002) peak intensity by controlling the etching time (Fig. 8d). Etching durations shorter than 2 h were insufficient to effectively remove the (002) facet, while treatment exceeding 2 h led to the reappearance of (002) planes due to severe surface damage caused by over-etching. SEM observation after treatment revealed that the resulting electrodes formed a vertically aligned, pillar-like Zn microstructure, which provided a smoother surface and reduced dendritic growth after plating compared with bare Zn. Moreover, depth-resolved color mapping of sulfur species (Fig. 8e) indicated severe surface

degradation on bare Zn, which retained substantial (002) exposure. In contrast, selective elimination of the (002) plane greatly alleviated surface parasitic reactions and limited by-product accumulation. Collectively, this study presents a counterintuitive yet effective approach in which the removal of the commonly preferred (002) plane reduces interfacial degradation and promotes uniform, dendrite-free Zn deposition.

Meanwhile, introducing Zn nucleation seeds directly into the Zn metal substrate represents an effective strategy for stabilizing initial nucleation and enhancing long-term electro-

chemical performance.[177,178] To date, various heterometallic seeds including Ag, Au, Co, Cu, Pb, Sn, Bi, and In have been investigated, which either form alloys with Zn^{2+} during electrochemical reactions to lower the nucleation barrier or guide preferential deposition through strong Zn^{2+} affinity.[179–187] Notably, nucleation sites enhance the spatial uniformity of Zn^{2+} reduction across the electrode surface, which leads to compact metal deposition and promotes horizontal growth. The morphology of the initial nucleation is particularly important in determining the subsequent deposition pathway, since charge tends to accumulate at protrusions, a phenomenon commonly known as the "tip effect", and this localized field intensifies dendritic formation. Therefore, designing a well-defined nucleation framework at an early stage is regarded as a prerequisite for attaining durable Zn anode operation. Li and co-workers incorporated silver nanoflakes (AgNFs) into the Zn anode, which led to the formation of an $AgZn_3$ alloy phase during cycling and mitigated dendritic propagation.[188] The AgNF-integrated electrode exhibited a significantly lower nucleation overpotential of 45.3 mV, in contrast to 77.8 mV observed for bare Cu. Chronoamperometric analysis confirmed suppressed vertical Zn growth and showed enhanced deposition uniformity over extended cycling. Moreover, electric field simulations revealed that the AgNF-modified surface remained smoother and maintained a more uniform interfacial field distribution. Building upon the stabilization effects of nucleation host incorporation, Zhang's group engineered an electrode by embedding Pb nanoparticles within a PVDF matrix through a chemical displacement reaction.[189] The PVDF component possessed strong hydrophobicity toward aqueous electrolytes and adhered to the Zn surface to block direct contact between the electrode and the bulk electrolyte. Simultaneously, the Pb nanoparticles with high Zn affinity contributed to electric field regulation and lowered the energy barrier for Zn nucleation. Pb also demonstrated greater resistance to hydrogen evolution compared with metallic Zn and delayed the onset potential of hydrogen evolution. As shown in Fig. 8f, the Gibbs free energy of hydrogen adsorption on the Pb surface was significantly higher than that on the Zn (101) plane, which confirmed the HER suppression capability of Pb. Furthermore, the strong affinity between Pb and Zn^{2+} resulted in a more negative adsorption energy on Pb (−2.70 eV) than on Zn (−2.19 eV), supporting stable epitaxial Zn deposition on the Pb-modified interface (Fig. 8g). The synergistic interaction between the electrochemical contributions of Pb and the interfacial characteristics imparted by PVDF led to a marked improvement in Zn reversibility, which outperformed Pb-only modification and enabled the electrode to sustain stable cycling for 800 h under a harsh DOD condition of 85.4% (Fig. 8h).

Anode engineering is an effective strategy encompassing diverse approaches, including electrode interfacial modification, selective etching, nucleation seed adoption, and the use of powder-type Zn. All are aimed at enhancing Zn anode reversibility and enabling higher depth-of-discharge, thereby increasing the overall energy density. By directly modifying the anode itself, these strategies offer a methodologically intuitive

route to performance enhancement, as they inherently reduce the number of uncontrollable variables. Meanwhile, verifying the practical feasibility of surface treatment processes represents a crucial consideration. Chemical waste solutions generated during electrode engineering often exhibit high reactivity, potentially compromising the inherent environmental advantages of AZIBs. Additionally, direct electrode treatments that involve the incorporation of costly metallic nucleation sites may impose significant economic burdens. These approaches typically require high material purity and precise control over interfacial chemistry, which further increase complexity and manufacturing expenditure. When extended to large-area electrodes, these treatments make it increasingly difficult to maintain uniformity and reproducibility due to higher system complexity. Accordingly, consistent performance across scalable electrode modifications becomes essential for practical application.

Currently, a metallic Zn foil that serves as both substrate and active material is the most widely used configuration for Zn anodes, with Table 2 concisely summarizing representative specifications of the previously discussed Zn foil anodes. However, powder-type Zn has recently gained attention as a promising alternative due to its low cost, ease of large-scale processing, and tunable physicochemical characteristics.[190–192] Moreover, powder-type anodes can be implemented without a separate foil lamination step and can leverage existing slurry-based processes, enabling continued use of current LIB manufacturing facilities. In addition, rational design of the N/P ratio allows tuning toward an optimal balance between performance and product quality. Despite these merits, powder-based Zn anodes suffer from an inherently large surface area, which increases their susceptibility to electrochemical and chemical side reactions.[193,194] In addition, spherical Zn particles often experience contact failure during repeated cycling, leading to the formation of electrically isolated "dead Zn" and the loss of continuous electron pathways, which severely impairs anode reversibility.[20,195] To overcome these limitations, Chen and co-workers developed a Bi@Zn powder anode by introducing zincophilic Bi nanosheets via a galvanic replacement reaction (Fig. 9a).[196] Owing to its stronger adsorption affinity for Zn^{2+} than metallic Zn, Bi acts as an effective nucleation site, promoting uniform and stable Zn deposition. This nucleation control improves the reversibility of Zn plating and stripping by preventing interparticle disconnection and preserving uninterrupted electron transport channels. As a result, Bi@Zn exhibited a markedly reduced nucleation overpotential compared with bare Zn and demonstrated stable cycling in symmetric cells under a high DOD of 45%. Moreover, Bi incorporation mitigates local charge accumulation, which suppresses intensified Zn growth during prolonged operation (Fig. 9b). Although the large surface area of powder-type Zn typically accelerates side reactions, the Bi-modified electrode exhibited suppressed HER, attributable to a higher Gibbs free energy of hydrogen adsorption (Fig. 9c). Accordingly, both DEMS and Tafel curves validated the superior electrochemical and chemical stability of Bi@Zn, confirming its practical viability for
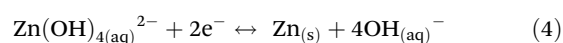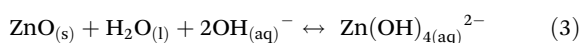
Table 2 Anode-focused strategies to develop high-energy-density metallic Zn foil-based AZIBs

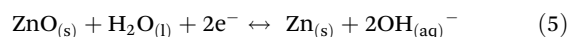| Strategy	Approach	Materials	Areal capacity (mAh cm^{-2})	Current density (mA cm^{-2})	Cycle life (h)	DOD (%)	Ref.
Artificial layers	Hydrophobic organic layer	$(C_2F_4)_n$–C	2	5	>900	40	136
	Hybrid multifunctional layer	ZIF-8 decorated GO	5	1	>500	42.7	145
	Hybrid multifunctional layer	Cu@PCN	20	10	>550	17.1	146
	Hybrid multifunctional layer	AA and LMS	10	2	>450	85.6	147
Additives	EDL modification	La(NO$_3$)$_3$	5.93	10	>140	80	161
	Adsorption on Zn	MPS	47.1	3	>350	80	98
	Adsorption on Zn	BED	40	1	>300	67.7	166
	In situ SEI formation	Zn(CF$_3$COO)$_2$	15	60	>180	87.1	167
Surface engineering	Selective chemical polishing	(NaPO$_3$)$_6$	13.5	10	>240	50	175
	Selective etching	Terephthalic acid and ZrCl$_4$	10	20	>400	20	176
	Alloy formation	Ag nanoflakes	5	10	>200	85.4	188
	Chemical displacement reaction	PVDF and PbCl$_2$	10	20	>800	85.4	189

AZIBs by addressing the critical drawbacks of powder-based Zn anodes.

While nucleation sites temper the initiation of metal growth, practical reversibility can also be achieved by the binder network that accommodates volume changes and preserves uniform ion transfer pathways. Currently, most reported studies have primarily focused on modifying the Zn powders themselves, whereas the role played by binder materials has received far less attention.[197,198] Given that the electrochemical performance of electrodes fabricated through slurry-casting processes is highly dependent on the properties of the binders, improving reversibility by optimizing binder functionality represents a methodologically sound and necessary direction. For instance, Lei et al. attempted to enhance electrochemical performance by replacing the commonly used PVDF binder with a blended binder composed of PTFE and carboxymethyl cellulose (CMC).[199] Single-component PVDF binders exhibit inadequate electrolyte wettability and poor Zn^{2+} affinity, rendering them unsuitable for uniform Zn deposition unless coupled with additional anode modifications. To address these limitations, the authors combined electrochemically stable and strongly hydrophobic PTFE, which mitigates side reactions in aqueous environments, with zincophilic CMC. The proposed dual-function binder suppresses hydrogen evolution and corrosion reactions, supports favorable Zn^{2+} transport pathways, and drives ordered Zn deposition.

Meanwhile, Zn–air batteries that target high energy density commonly employ alkaline electrolytes to promote the oxygen reduction reaction (ORR) and the oxygen evolution reaction (OER) at the cathode.[200] However, the poor reversibility of Zn anodes in alkaline media prevents full utilization of the attainable energy density and remains a bottleneck for the development of high-energy zinc batteries. Unlike in acidic media, Zn anodes in alkaline electrolyte undergo dissolution and precipitation, complexation, and redox reactions that lower reversibility, as follows:[201]

$$ZnO_{(s)} + H_2O_{(l)} + 2OH_{(aq)}^{-} \leftrightarrow Zn(OH)_{4(aq)}^{2-} \quad (3)$$

$$Zn(OH)_{4(aq)}^{2-} + 2e^{-} \leftrightarrow Zn_{(s)} + 4OH_{(aq)}^{-} \quad (4)$$

Overall:

$$ZnO_{(s)} + H_2O_{(l)} + 2e^{-} \leftrightarrow Zn_{(s)} + 2OH_{(aq)}^{-} \quad (5)$$

This complex solid–solute–solid pathway forms a ZnO passivation layer on the anode surface during cycling, which hinders the reversible reaction of metallic Zn. It can also trigger anode dissolution, leading to loss of active material and morphological degradation that undermines long-term operation. Recently, Liu's group reported an aqueous zinc battery operable under alkaline conditions by introducing a ZnO anode.[202] They replaced metallic Zn with ZnO nanorods to mitigate reversibility loss arising from parasitic reactions. The ZnO anode was coated with a TiO$_2$ passivation layer that allowed OH^{-} and H$_2$O transport while blocking Zn(OH)$_4^{2-}$, which improved stability. In addition, the TiO$_2$ layer exhibited low HER activity, suppressing hydrogen evolution and the associated electrolyte depletion that are problematic in alkaline media. To verify coating uniformity and the stability of the passivating effect, the authors synthesized a HER-suppressing sealed nanorod (HSSN) anode and confirmed a conformal TiO$_2$ shell around ZnO by scanning transmission electron microscopy (STEM) (Fig. 9d). Owing to this robust coating, immersion in 4 M KOH resulted in nearly 90% lower Zn dissolution for the HSSN anode compared with uncoated ZnO. To further assess HER suppression, TiN$_x$O$_y$ with a similar structure served as a control sample for linear sweep voltammetry, and TiO$_2$ showed markedly improved HER resistance (Fig. 9e). Since HER activity correlates with the free energy of hydrogen adsorption, a higher adsorption free energy corresponds to lower HER activity. Computational analysis revealed a larger H-adsorption free energy for TiO$_2$ (0.50 eV) than for TiN$_x$O$_y$ (0.24 eV), clarifying the underlying mechanism. As a result, cells employing the HSSN anode operated stably in a beaker cell environment and 100% DOD level, which demonstrates the feasibility of alkaline-electrolyte aqueous zinc batteries (Fig. 9f).
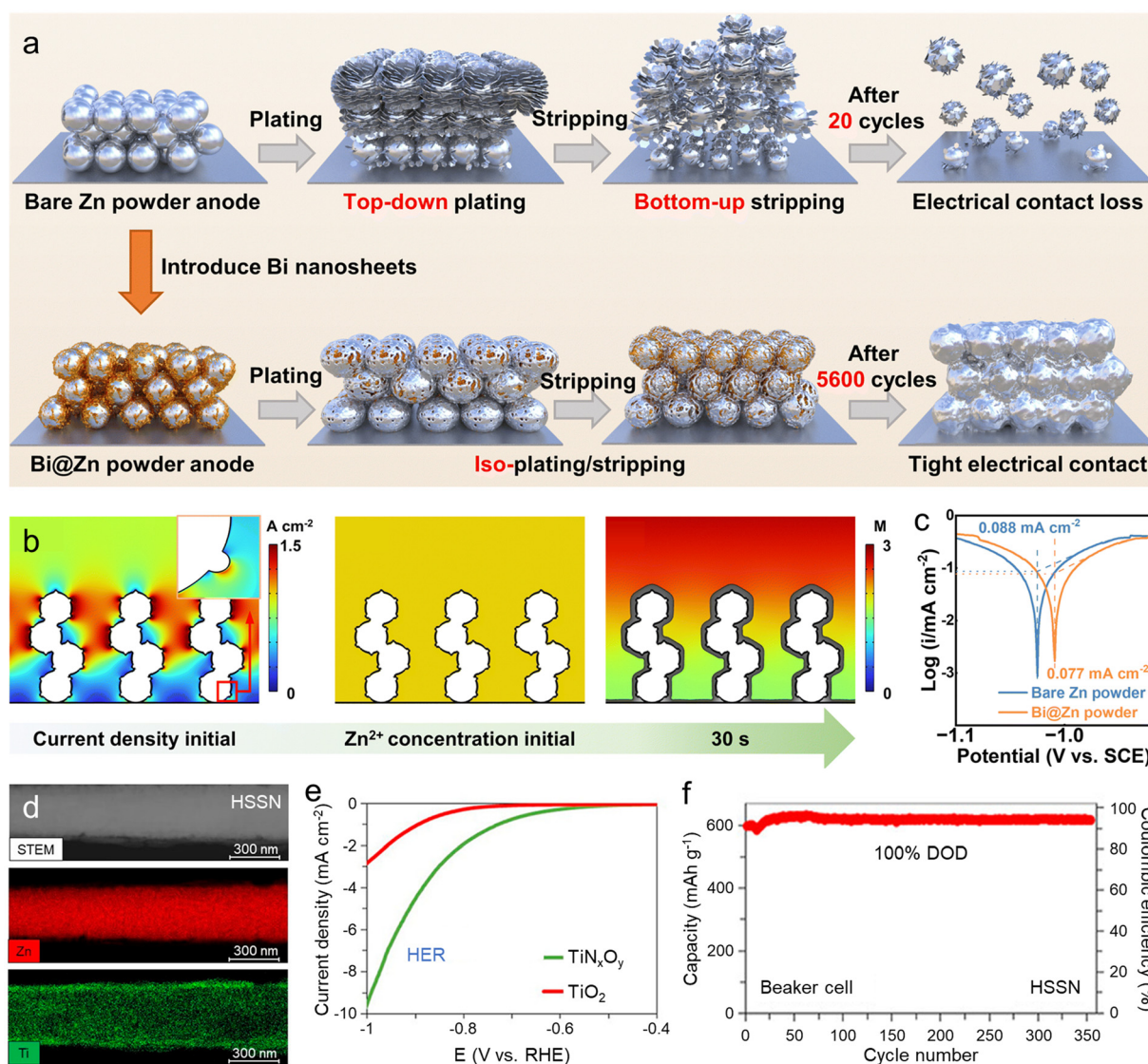
Fig. 9 Alternative anodes to replace Zn foil in high-energy-density AZIBs. (a) Schematic illustration of plating/stripping behavior of the bare Zn powder anode (top) and Bi@Zn powder anode (bottom). (b) COMSOL simulation of current density distribution (left), Zn^{2+} concentration (middle), and morphology evolution (right) of the Bi@Zn powder anode during plating to elucidate Zn deposition mechanism. (c) The calculated adsorption free energy of H (ΔG_{H*}) on the Zn and Bi. Reproduced with permission from ref. 196. Copyright 2024, The Royal Society of Chemistry. (d) STEM image and elemental mappings of a $ZnO@TiO_2$ nanorod. (e) IR-corrected polarization curves of TiN_xO_y and TiO_2 electrodes. At any fixed potential, the hydrogen evolution on the TiN_xO_y electrode is severer than the TiO_2 electrode. Scan rate is 2 mV s^{-1}. (f) Cycling performance of the HSSN anode in a beaker cell with a large amount of electrolyte at 100% DOD. Reproduced with permission from ref. 202. Copyright 2020, American Chemical Society.

5. Tailoring cathode materials for high capacity and elevated operating voltage

The energy density of AZIBs is governed by both specific capacity and the working voltage, where the working voltage is determined by the potential difference between the cathode and the Zn anode. In most AZIB configurations, metallic Zn is employed directly as the anode, which means that the working voltage is primarily governed by the cathode potential. This

relationship emphasizes the need for high-voltage cathode materials in AZIBs. From a capacity perspective, Zn anodes intrinsically provide high gravimetric and volumetric capacities. However, the relatively low capacity of most cathodes causes an imbalance, and a considerable fraction of the Zn anode remains unused. As a result, enhancing both redox potential and the capacity of cathode materials becomes a critical factor in boosting the overall energy density of AZIBs.

Currently, multiple strategies have been proposed to increase energy density through cathode-side modifications. From a chemical standpoint, a strategy to improve the intrinsic

characteristics of the active material, such as capacity and redox potential, is one approach. From an engineering standpoint, the practical energy density depends on minimizing the mass contribution of electrochemically inactive components, such as the current collector (CC), binder, and conductive materials. This objective may be realized by decreasing the absolute quantity of inactive constituents or by increasing the proportion of active material, which reduces the relative content of inactive phases within the electrode. For example, the binder system can be engineered to ensure strong adhesion even in thick-electrode configurations.[203] The structural reinforcement helps maintain the overall architecture and ensures sufficient mechanical contact. Beyond adhesion, advanced binders may also facilitate ionic and electronic transport throughout the bulk of the electrode. As a result, redox reactions can proceed uniformly across the entire thickness. The design of CC can also be modified by reducing its weight or enhancing its conductivity to maintain uniform electron transport within high-mass-loading electrodes. This section highlights recent progress in cathode-focused strategies aimed at increasing the energy density of AZIBs. Particular attention is given to material design, structural and compositional engineering of electrodes, and approaches that support high-mass-loading architectures. This section also provides future perspectives for the development of cathode systems capable of maximizing the energy output of AZIBs.

5.1 Design of optimized cathode materials

Cathode materials used in AZIBs can be broadly categorized into four representative families: manganese-based oxides, vanadium-based compounds, Prussian blue analogues (PBAs), and organic cathodes.[204] Each category offers distinct electrochemical characteristics and faces specific challenges that influence their suitability for practical applications. Manganese-based oxides are among the most extensively studied cathode materials due to their natural abundance, low toxicity, environmental friendliness, and cost-effectiveness.[205] Manganese-based oxides exhibit theoretical capacities of 308 mAh g^{-1} based on one-electron redox reactions and up to 616 mAh g^{-1} through two-electron processes.[206] Discharge potential of manganese-based oxides typically ranges between 1.2–1.4 V vs. Zn/Zn^{2+}, where crystalline phases of manganese dioxide exist in various polymorphs including α-, β-, γ-, λ-, and ε-MnO$_2$.[207–212] Owing to their structural differences, each phase exhibits unique ion transport kinetics, electrochemical stability, and charge–discharge characteristics, which play a key role in determining the electrochemical performance of each phase. In addition to MnO$_2$ polymorphs, both tunnel-type materials (e.g., Na$_{0.44}$MnO$_2$) and spinel-structured compounds (e.g., LiMn$_2$O$_4$) have been explored as candidates with structural versatility and potential for stable Zn^{2+} storage.[213] However, manganese-based materials still suffer from Mn^{2+} dissolution and limited ionic or electronic conductivity, which hinders long-term cycling performance.

Vanadium-based cathodes, which utilize vanadium oxides, also offer several promising features. Vanadium is inexpensive

and widely available and exhibits multiple valence states from V^{2+} to V^{5+}.[214] The multivalence allows multi-electron redox reactions, which theoretically support specific capacities ranging from 200 to 500 mAh g^{-1}. In particular, hydrated compounds such as V$_2$O$_5$·nH$_2$O have been reported to facilitate Zn^{2+} intercalation due to their expanded interlayer spacing and also exhibit pseudocapacitive behavior.[215] As a result, vanadium-based materials are not only employed in AZIBs but have also been actively studied in lithium-ion and sodium-ion battery systems.[216,217] Nonetheless, these materials typically operate at low discharge potentials below 1 V vs. Zn/Zn^{2+}, which limits the achievable energy density.[218] In addition, dissolution of active materials in aqueous electrolytes during the repeated cycles remains a critical issue, as similarly observed in Mn-based cathodes.[219] Extensive research efforts are ongoing to address these drawbacks through material modification and electrolyte engineering.

PBAs represent another important class of AZIB cathodes, particularly notable for their relatively high operating voltages (1.4 V–1.8 V vs. Zn/Zn^{2+}) and stable electrochemical behavior. These materials generally adopt a face-centered cubic framework with the formula A$_x$M$_1$[M$_2$(CN)$_6$]$_y$·nH$_2$O, where M$_1$ and M$_2$ are transition metals bridged by cyanide ligands and A represents mobile alkali or alkaline earth cations, respectively.[57] Their open 3D structure facilitates rapid Zn^{2+} diffusion, supporting efficient electrochemical kinetics. However, PBAs generally exhibit low theoretical capacities of less than 100 mAh g^{-1} and poor electronic conductivity.[220] To overcome these limitations, the development of high-capacity PBA-type materials and their integration with conductive frameworks is essential. Additionally, numerous AZIB cathodes are synthesized via hydrothermal routes. Continuous discussion is required to determine whether this method can be feasibly scaled up for practical implementation.[221] A summary of the representative inorganic cathodes for AZIBs discussed above is provided in Fig. 10.[222–229]

Organic cathodes, in contrast to inorganic systems, offer lightweight and sustainable alternatives. Organic cathodes can be synthesized from abundant feedstocks and provide structural tunability through molecular design. Environmental compatibility and broad functional diversity of organic cathodes have attracted increasing attention. Common redox-active groups in organic cathodes include quinone (C=O) and imine (C=N) functionalities, which reversibly interact with Zn^{2+} or H$^+$ during the cycle.[230,231] While these materials offer design flexibility and green chemistry potential, they also often suffer from low conductivity, structural instability in aqueous media, and solubility-related capacity loss. Consequently, strategies such as polymerization, backbone stabilization, and hybridization with conductive components have been explored to enhance their electrochemical performance. This section introduces each cathode material system in detail and highlights recent strategies that have been developed to enhance energy density by improving capacity and operating voltage through material design.

Recently, Katsuyama et al. reported a promising strategy to enable the two-electron redox process of manganese oxide,
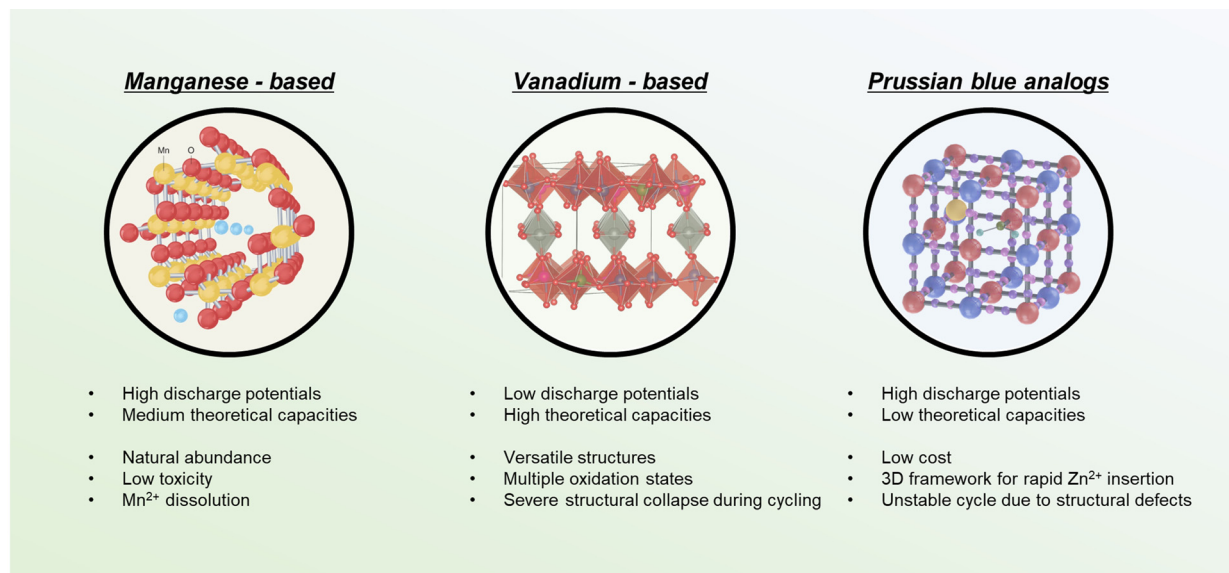
Fig. 10 Overview of diverse cathode materials investigated for AZIBs, with emphasis on their distinct advantages and critical challenges. Reproduced with permission from ref. 222. Copyright 2022, Springer Nature. Reproduced with permission from ref. 223. Copyright 2016, Springer Nature. Reproduced with permission from ref. 224. Copyright 2022, Elsevier.

thereby realizing its theoretical capacity.[232] While $ZnMn_2O_4$ theoretically allows a Mn^{4+}/Mn^{2+} redox reaction (448 mAh g^{-1}), previous studies had been limited to a one-electron process. By synthesizing ultrasmall $ZnMn_2O_4$ nanoparticles with a diameter of 5 nm *via* a rapid room-temperature alcohol reduction process and compositing them with high-surface-area graphene, a reversible capacity of 445 mAh g^{-1} was realized, which closely approaches the theoretical maximum (Fig. 11a). The graphene not only served as a conductive matrix but also mitigated nanoparticle aggregation by forming a percolating network that enhances both electron transport and electrochemical accessibility across the electrode. As evidenced in Fig. 11b, the ultrasmall $ZnMn_2O_4$ nanoparticles without graphene exhibited severe aggregation and developed large secondary clusters that can hinder ion/electron transport. In contrast, the graphene-containing composite in Fig. 11c displayed a well-dispersed morphology, where the nanoparticles are uniformly anchored on the graphene sheets. This configuration effectively prevented aggregation and promoted interfacial contact. In addition to achieving high capacity, the composite electrode demonstrated excellent tolerance under elevated current densities. The specific discharge capacity remained at 406 mAh g^{-1} at a high current density of 2000 mA g^{-1}, corresponding to only an 8% decrease compared with the value at 100 mA g^{-1}. Even at 10 000 mA g^{-1}, it maintained 334 mAh g^{-1}, confirming its remarkable rate capability. Furthermore, the full cell exhibited an energy density of 371 Wh kg^{-1}, with a projected increase to 504 Wh kg^{-1} when the active material loading reaches 80%. The improvement demonstrates that nanoscale engineering combined with conductive frameworks can unlock multivalent redox pathways in conventional spinel materials, providing a viable route toward high-capacity and high-rate AZIBs.

Building on the previous approach which enhances the capacity of Mn-based cathodes by introducing additional components into the electrode, the study introduced here focused on directly intercalating organic molecules into the voids between vanadium oxide layers, thereby altering the intrinsic characteristics of the active material itself. Zhang *et al.* utilized organic molecular intercalation to engineer vanadium oxide cathodes, aiming to address the sluggish ion diffusion and low operating voltage commonly seen in layered vanadium-based materials.[233] By intercalating 1,3-propane diamine (DP) molecules, the interlayer spacing of $V_3O_7·H_2O$ (VO) was expanded from 8.5 to 10.3 Å, as verified by the XRD peak shift from 10.4° to 8.6° (Fig. 11d). This structural modification alleviated electrostatic repulsion and steric hindrance, and it formed more accessible pathways for Zn^{2+} insertion. As clearly shown in Fig. 11e, electrochemical kinetics measured by galvanostatic intermittent titration technique (GITT) analysis revealed that VO-DP reached Zn^{2+} diffusion coefficients in the range of 10^{-7} to 10^{-8} cm^2 s^{-1}, which are much higher than pristine VO. Importantly, this fast diffusion was maintained even after 300 cycles at high current densities, indicating excellent structural resilience. In addition to improving Zn^{2+} transport, DP ligands also participated in the charge storage process alongside vanadium oxide, which helped to stabilize the layered framework during repeated cycling. This collaborative charge–discharge mechanism not only enhanced structural integrity but also elevated the redox potential, and the system reached a high operating voltage of 0.89 V (Fig. 11f). Through the intercalation strategy, the VO-DP cathode affords both higher operating voltage and capacity, offering a promising pathway for advanced AZIB development.

Differing from vanadium-based cathode systems, as mentioned above, PBAs operate at relatively high voltages but
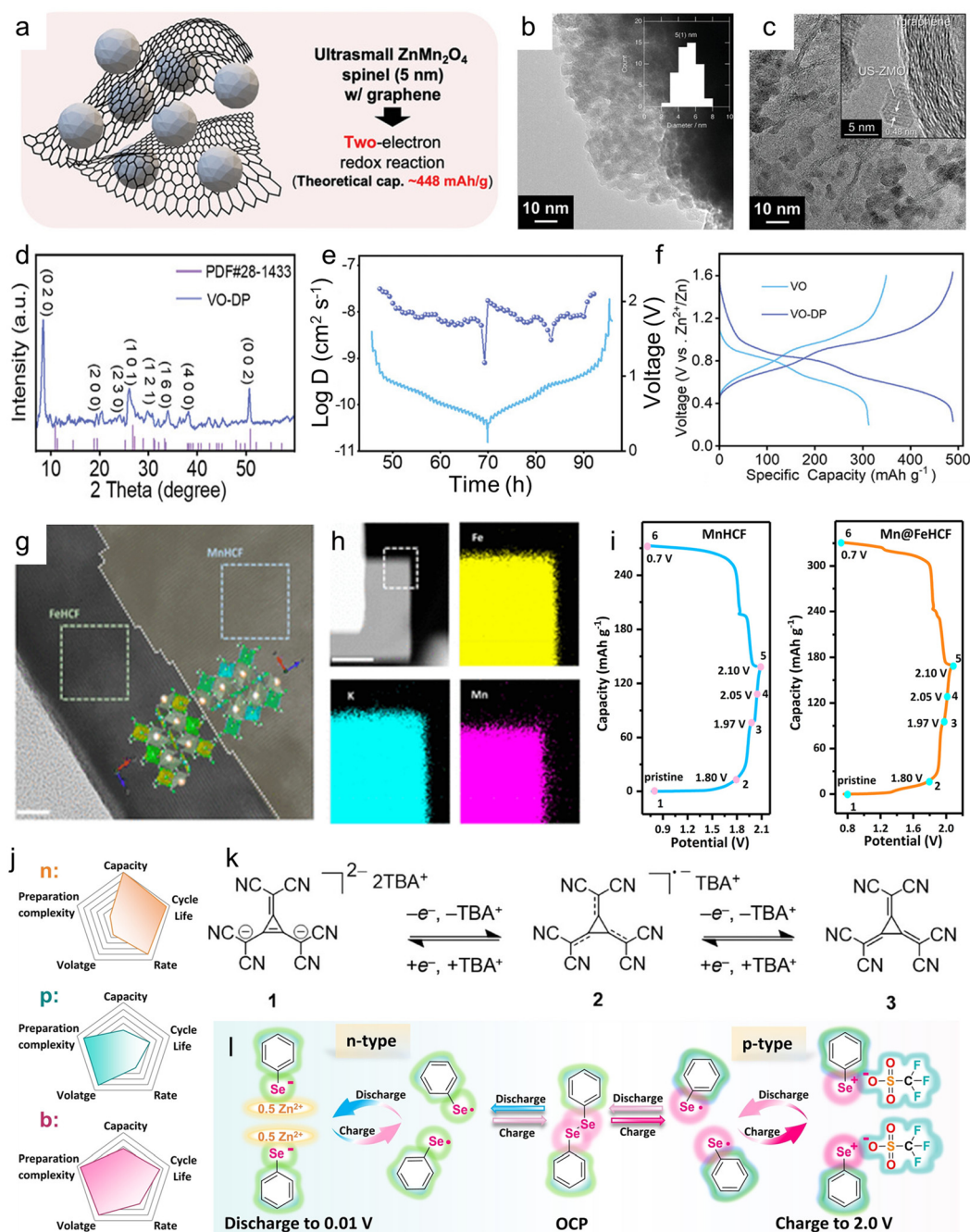
Fig. 11 Strategies to enhance energy density through the structural and compositional tuning of cathode materials. (a) Conceptual illustration of the ultrasmall $ZnMn_2O_4$ spinel (5 nm) and graphene composite. (b) TEM images of ultrasmall $ZnMn_2O_4$ nanoparticles and (c) ultrasmall $ZnMn_2O_4$ spinel nanoparticles composited with graphene. Reproduced with permission from ref. 232. Copyright 2024, Wiley-VCH. (d) XRD pattern of VO-DP. (e) Diffusivity coefficient and voltage files during GITT measurements. (f) The charge–discharge curves of Zn||VO and Zn||VO-DP cycling at 0.05 A g^{-1}. Reproduced with permission from ref. 233. Copyright 2023, Wiley-VCH. (g) HRTEM image of the Mn@FeHCF. (h) EDS elemental mappings. (i) Voltage profiles of the MnHCF and Mn@FeHCF. Reproduced with permission from ref. 234. Copyright 2023, American Chemical Society. (j) Overview of the basic characteristics of the n-, p-, and bipolar-type organic cathodes for AZIBs. (k) Proposed redox mechanism of $CpCN_6^{2-}$. TBA cation insertion/de-insertion occurs when $Cp(CN)_6$ core is oxidized/reduced between −2 to 0 state. Reproduced with permission from ref. 238. Copyright 2024, Wiley-VCH. (l) Schematic illustration of the molecular structure transformations of PDSe during charging and discharging. Reproduced with permission from ref. 237. Copyright 2024, Wiley-VCH.

suffer from intrinsically low capacity. Among them, manganese-based PBA compounds such as manganese hexacyanoferrate (MnHCF) are representative examples, characterized by the ability to access the Mn^{2+}/Mn^{3+} redox couple for capacity contribution and also facing critical limitations such as severe manganese dissolution and Jahn–Teller distortion during

cycling. The degradation pathways gradually reduce the amount of active material and compromise structural stability, which restricts both reversible capacity and long-term durability.

To overcome the challenges and enhance energy density, it is essential to simultaneously increase the active capacity and maintain structural stability during cycling. In response to this need, Yang *et al.* proposed an epitaxial core–shell architecture, where MnHCF serves as the high-capacity core, and iron hexacyanoferrate (FeHCF) forms a protective shell (Fig. 11g and h).[234] The protective shell effectively blocked the direct contact between the manganese core and the electrolyte, suppressing Mn dissolution. During Zn^{2+} insertion, the FeHCF shell partially transformed into an amorphous layer, which played a critical role in stabilizing the electrode interface. This amorphous region accommodated the mechanical stress generated during ion insertion and extraction, and this stress accommodation helped limit the volume expansion of the core. As a result, the FeHCF shell not only served as a protective barrier against electrolyte attack but also functioned as a dynamic buffer layer that stabilized both structural and electrochemical performance during cycling. Thanks to this design, the Mn@FeHCF electrode exhibited substantially improved cycling stability and higher capacity compared with pristine MnHCF (Fig. 11i). The core–shell structure delivered a high reversible capacity of 166 mAh g^{-1} and exhibited an average discharge voltage of about 1.8 V.

Consistent with the majority of reported studies, inorganic cathodes have been widely used in AZIBs. However, organic cathodes have also been explored as promising candidates, offering advantages such as structural tunability, sustainability, and the potential for high energy density. In terms of charge storage mechanisms, organic cathodes can be categorized into n-type, p-type, and bipolar (b-type) materials, each with distinct characteristics that significantly affect their electrochemical performance (Fig. 11j). The n-type organic cathodes primarily store charge by the insertion of cations, facilitated by functional groups such as carbonyl (C=O) or imines (C=N) and generally exhibit high capacities but operate at low redox potentials (<0.8 V *vs.* Zn/Zn^{2+}).[235,236] For example, calix[4]quinone (C4Q) has been studied for the high capacity, but practical application is limited by the relatively low voltage range.[230] In contrast, p-type organic cathodes store charge through the insertion of anions. The p-type organic cathodes are known for their high redox potentials, typically above 1.0 V *vs.* Zn/Zn^{2+}, making them ideal for achieving high energy density.[237] However, p-type cathodes often suffer from limited charge storage (<100 mAh g^{-1}), which constrains the deliverable energy output. Although high-voltage operation is feasible, the insufficient reversible capacity also narrows the scope of practical implementation in energy-demanding systems.

Accordingly, several efforts have been made to elevate the operating potential of n-type cathodes or to enhance the charge-storage capacity of p-type cathodes. Park *et al.* developed a cyclopropanate-based cathode, $Cp(CN)_6^{2-}$, and intro-

duced tetrabutylammonium triflate (TBAOTf) salts into the aqueous electrolyte.[238] The TBA^+ cation stabilized the cathode by preventing the dissolution of active materials throughout repeated cycling. This stabilization supported high-voltage operation beyond its intrinsic redox potential. In this system, during charging, TBA^+ de-inserts while $Cp(CN)_6^{2-}$ oxidized to its neutral state (Fig. 11k). During discharge, the TBA^+ re-inserted as the neutral $Cp(CN)_6$ was reduced back to the −2 state, completing a reversible two-electron redox cycle. The electrolyte engineering strategy allowed the n-type cathode to operate stably at discharging voltages up to 1.4 V, and the system overcame the conventional voltage limitations of n-type organic cathodes.

Uniquely, beyond the two types of cathodes, there is another type of organic cathode called b-type organic cathode. Dual redox functionality in b-type organic cathodes permits the uptake of both cations and anions by bridging the charge-storage mechanisms of both types. Accordingly, this class of cathode achieves a synergistic balance between large specific capacity and elevated working potential. Nevertheless, many studies reported that b-type systems cannot fully exhibit bipolar redox activity due to poor reversibility and suboptimal charge-storage capability. For example, bis(phenylamino)phenothiazin-5-ium iodide (PTD-1), a representative b-type organic cathode for AZIBs, delivers an average discharge voltage of 1.1 V and limited capacities below 150 mAh g^{-1} at a rate of 0.1 A g^{-1}.[239] Therefore, it is imperative to unlock the full potential of b-type organic cathodes by designing new electroactive sites beyond conventional organic functional groups.

Accordingly, a representative case is introduced here, in which a design strategy successfully addresses these challenges and fully realizes the bipolar advantages of b-type organic cathodes. For instance, Yan *et al.* introduced phenyl diselenide (PDSe) as a promising b-type cathode material that overcomes some of these limitations.[237] The charge–discharge mechanism of PDSe involves a dynamic structural transformation that enhances its electrochemical performance. Fig. 11l schematically displays the molecular changes during the cycle, where the Se–Se bond in PDSe can be continuously broken and repaired. The process is initiated in the first step, where the reaction is described as:

$$PhSe\text{-}Zn\text{-}SePh \rightleftharpoons PhSe\text{-}SePh + Zn^{2+} + 2e^- \quad (6)$$

In this step, the Zn^{2+} ions are extracted from the PDSe cathode, while electrons flow through the external circuit. The bond between PhSe and Zn is broken, and the Zn^{2+} ions, along with the electrons, are released into the electrolyte.

In the second step, the cathode undergoes an anion coordination reaction with OTf^-:

$$PhSe\text{-}SePh + OTf^- \rightleftharpoons 2PhSe\text{-}OTf + 2e^- \quad (7)$$
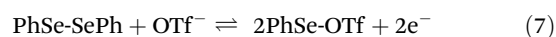
This step involves the PhSe-SePh molecules reacting with OTf^- to form PhSe-OTf, while diselenide bonds are released. This further facilitates the two-electron redox process that is key to high-voltage operation and long cycle life. These find-

Table 3 Summary of cathode materials for high-energy-density AZIBs

Cathode type	Materials	Voltage range (V vs. Zn/Zn^{2+})	Specific capacity (mAh g^{-1}) / current density (mA g^{-1})	Mass loading (mg cm^{-2})	Ref.
Mn-based	ZnMn$_2$O$_4$ spinel + graphene	0.8–1.85	448/0.1	—	232
V-based	1,3-Propane diamine-intercalated V$_3$O$_7$·H$_2$O	0.2–1.6	473/0.05	—	233
Prussian blue-based	Epitaxial Mn@FeHCF	0.7–2.1 (or ~2.2)	166.3/0.1 12 mAh/0.03	1.5 (coin cell-type) 4 (pouch-type)	234
Organic cathode	Cp(CN)$_6^{2-}$	0.7–1.8	78.4/3.76 50/38.4	2–2.5 10	238
	Phenyl diselenide + ordered mesoporous carbon	0.01–2.0	621.4/0.1	2	237

ings demonstrate that PDSe-based cathodes can achieve high voltage and long cycle life by leveraging the dynamic bond-breaking and self-repairing mechanism during charge–discharge cycles. Through sequential redox reactions, PDSe enables dual-ion coordination and offers potential as a viable b-type organic cathode material. Collectively, Table 3 summarizes the characteristics of the cathodes described above.

5.2 Modification of polymeric binders

As discussed in the anode section, achieving a high DOD and reducing N/P ratio are key strategies for maximizing energy density. However, most currently reported AZIB systems still exhibit relatively high N/P ratios, mainly due to the use of thin cathodes that limit the areal capacity. To address this issue, designing thick cathodes with minimized inactive fractions is necessary, and this relies on binder systems that can reliably support thick-electrode fabrication. Ironically, although the binder is required to deliver robust adhesion, it must simultaneously be used sparingly to preserve the high proportion of electrochemically active components. This conflicting requirement complicates the design of binder systems, especially under harsh cycling conditions.

Therefore, several core requirements must be met by binders to achieve this goal. First, strong adhesion is indispensable for maintaining the structural integrity of thick electrodes during fabrication and cycling. Without sufficient adhesion, electrode cracking and delamination occur more readily as the electrode thickness increases. Second, oxidative stability is critical because AZIB cathodes often operate at voltages beyond the thermodynamic window of water, where oxidative degradation of the binder could compromise both electrode stability and battery safety.[240] Third, binders must facilitate ionic conduction since they typically coat active materials, potentially hindering electrolyte penetration and Zn^{2+} transport.[241] Therefore, ionic pathways should be maintained across the electrode. Fourth, hydrophilicity is essential to ensure the aqueous electrolyte uniformly wets the entire electrode structure, particularly for thick electrodes where poor electrolyte infiltration could result in underutilized inner regions. Lastly, binder must enable homogeneous dispersion of active materials and conductive additives during slurry preparation to achieve uniform electrode microstructure and performance.

Beyond these essential properties, several optional but desirable features can further improve electrode stability and performance. Binders capable of buffering structural stress or exhibiting self-healing properties may alleviate damage caused by phase transitions or lattice distortions in AZIB cathodes.[242] While such structural changes are typically moderate in aqueous systems, they can still occur during the cycle in cathode materials like MnO$_2$ and other transition metal oxides, where repeated ion insertion and extraction induce local mechanical strain. Also, water-based slurry processability is beneficial for environmental sustainability and process scalability, aligning with the intrinsic eco-friendly nature of AZIBs that utilize non-flammable aqueous electrolytes and abundant raw materials. Moreover, imparting electronic conductivity to the binder could mitigate contact loss during the cycle, which becomes more problematic in thick electrodes. Lastly, ionic coordination capability could help immobilize dissolved metal species, such as Mn^{2+}, which are typically observed in cathode systems like MnO$_2$.[243] By suppressing metal dissolution and shuttling effects, such binders contribute to stabilizing the electrode–electrolyte interface and improving long-term cycling performance. In this section, recent binder designs are highlighted that enable thick cathode fabrication and improved electrolyte infiltration, ultimately advancing the practical energy density of AZIBs.

A recent study by Feng et al. introduced polyurea-based binders incorporating dynamic diselenide or disulfide bonds for AZIBs.[243] Through a one-step polymerization, two types of binders, polyurea-containing diselenide (PICSe) and polyurea-containing disulfide (PICS), were synthesized, which incorporated Se–Se and S–S linkages, respectively, into the polyurea backbone (Fig. 12a). These dynamic bonds, together with hydrogen bonding between urea groups, induced physical cross-linking that substantially enhanced the mechanical stability of the cathode. In particular, the PICSe-based electrode exhibited a peel strength of 3.36 N, over sevenfold higher than that of PVDF binder, effectively sustaining electrode integrity during repeated volume changes (Fig. 12b). Beyond mechanical reinforcement, these binders acted as dynamic cofactors for Zn^{2+} transport. Diselenide and disulfide units reversibly coordinated with Zn^{2+} ions, facilitating charge transfer and enhancing redox kinetics. Among the two, diselenide exhibited faster Zn^{2+} diffusion (log D_{Zn} = −7.5 to −10.5), which stems from selenium's lower bond dissociation energy and greater electrical conductivity compared with sulfur (Fig. 12c). The properties synergistically accelerated the dynamic bond
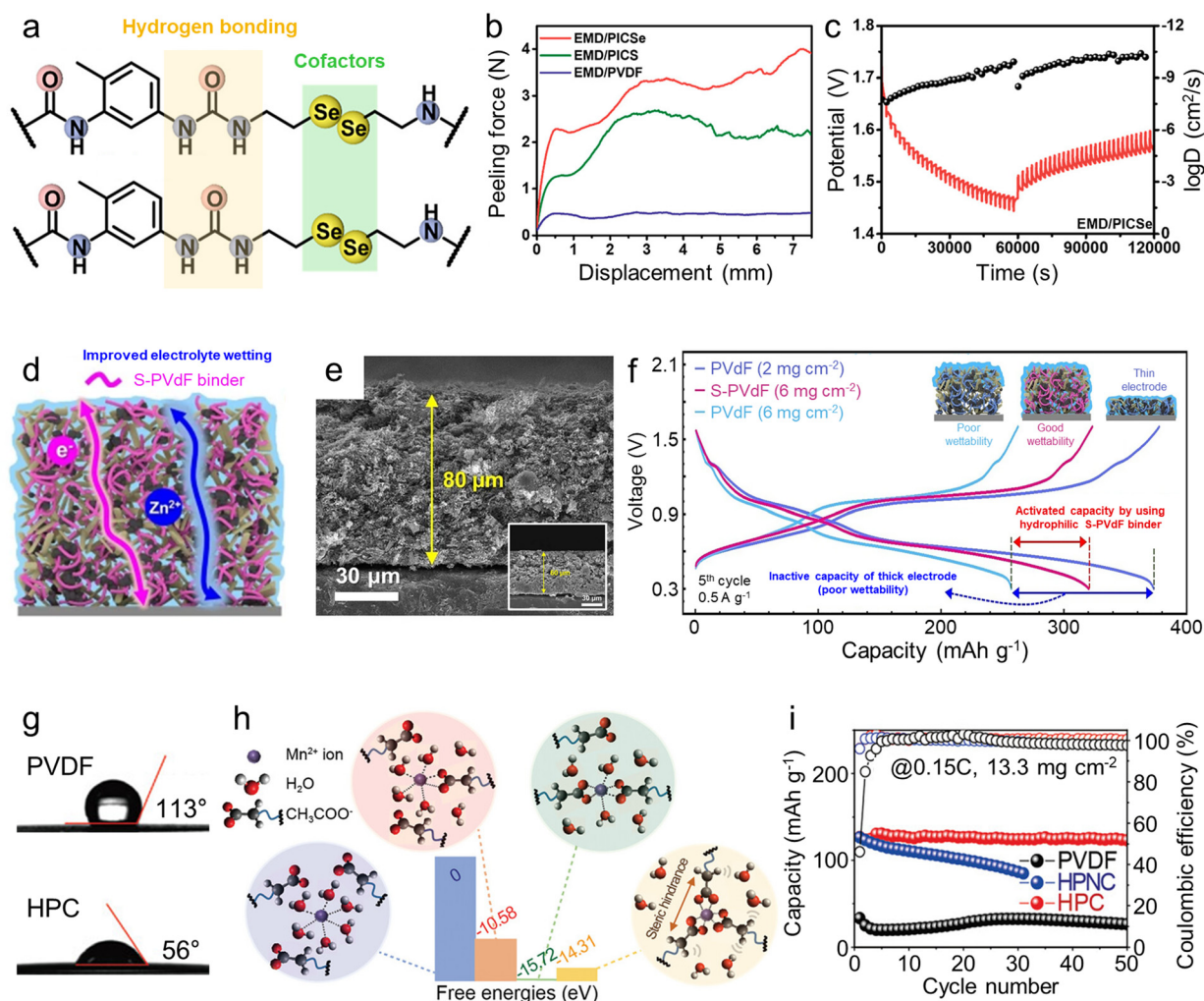
Fig. 12 Thick electrode engineering based on a newly developed functional binder. (a) Schematic diagram of the chemical structure and electrochemical reaction of the binders. (b) Peeling force−displacement curves of different binder-based cathodes. (c) GITT test curve of the PICSe-based cathode. Reproduced with permission from ref. 243. Copyright 2025, American Chemical Society. (d) Schematic illustrations show the facile transport of Zn^{2+} in a thick electrode with S-PVdF binders. (e) Cross-sectional SEM images of cathodes with S-PVdF binders before the calendering process. Inset images correspond to the post-calendering state. (f) Galvanostatic charge/discharge voltage profiles voltage *versus* specific capacity at a current density of 0.5 A g^{-1} (the 5th cycle). Reproduced with permission from ref. 244. Copyright 2023, Springer Nature. (g) Electrolyte contact angles of electrodes prepared with PVDF and HPC binders. (h) Comparison of the relative total energy between the CH_3COO^- functional group on the binder and Mn^{2+} ions dissolved in water. (i) Cycling performances of the $Zn\|MnO_2$ cells with three electrodes using PVDF and HPC binders with loading levels of 13.3 mg cm^{-2}. Reproduced with permission from ref. 245. Copyright 2024, Wiley-VCH.

exchange and Zn^{2+} migration during battery operation. Nevertheless, this work primarily focused on Zn^{2+} coordination and thin-film electrodes and did not explore the complexities associated with thick electrodes. Future studies should extend this binder design to high-mass-loading cathodes, assess ion transport properties and ensure that electrolyte infiltration enables sufficient electrochemical reactions throughout the entire electrode thickness. These investigations will be vital for advancing practical, high-energy-density AZIBs.

Another study on binder modification in AZIBs is summarized as follows. Lee *et al.* developed a sulfonated polyvinylidene fluoride (S-PVdF) binder as a practical approach to improve the wettability and electrochemical performance of

thick cathodes (Fig. 12d).[244] S-PVdF was synthesized *via* a simple sulfonation process. The process introduced numerous sulfonate groups onto the hydrophobic PVdF backbone. The modified hydrophilic groups dramatically reduced the electrolyte contact angle of the electrode to 39°, compared with 92° for the pristine PVdF, and enabled effective electrolyte penetration throughout the thick electrode. As a result, electrodes with S-PVdF achieved uniform ion transport and enhanced utilization of the active materials. As shown in Fig. 12e, cross-sectional SEM analysis showed that the S-PVdF-based thick electrodes reached an initial thickness of 80 μm before calendering, while an inset figure illustrates a reduced thickness of 60 μm after the calendering process. The results confirmed the

fabrication of densely packed thick electrodes without compromising electrolyte accessibility. Electrochemical testing further emphasized these improvements. As observed in Fig. 12f, voltage profiles indicated that thin PVdF electrodes (~2 mg cm^{-2}) delivered high capacity. On the other hand, thick PVdF electrodes (~6 mg cm^{-2}) exhibited substantial inactive capacity, largely due to poor wettability that restricted electrolyte access and limited the reaction depth. In comparison, thick S-PVdF electrodes retained high capacities with lower polarization. This improvement stemmed from the hydrophilic nature of S-PVdF, which promoted uniform electrolyte infiltration and efficient ion transport across the entire electrode thickness.

While previous studies separately addressed important aspects of binder design, one focusing on dynamic metal coordination and the other on improving hydrophilicity for thick electrodes, the following work combined both strategies and further eliminated fluorinated components. Choi *et al.* developed a fluorine-free, hydrophilic crosslinked (HPC) binder comprising sodium carboxymethyl cellulose (CMC), poly(acrylic acid) (PAA), and styrene–butadiene rubber (SBR).[245] The HPC binder not only improved hydrophilicity as confirmed by contact angle measurements (56° for HPC *vs.* 113° for PVDF) which means efficient electrolyte penetration into thick electrodes, but also provided metal coordination capability through its functional groups, as demonstrated by DFT calculations (Fig. 12g). The simulations showed that Mn^{2+} ions, initially coordinated with water molecules, formed progressively stronger interactions when replaced by carboxylate groups (Fig. 12h). When one carboxylate group replaced two water molecules, the binding energy decreased to −10.6 eV. The interaction became even more stable when a second carboxylate group binds, and the binding energy reached a minimum energy of −15.7 eV. The result indicates the most thermodynamically favorable structure. Although coordination with three carboxylate groups resulted in slightly weakened binding due to steric hindrance, all calculated configurations exhibited negative binding energies, which confirms that Mn^{2+} can be stably adsorbed by the binder in various coordination environments. Due to this effect, the suppression of Mn^{2+} dissolution was experimentally validated under electrolyte conditions without added Mn salts. Even without external Mn^{2+} additives, the HPC-based cells exhibited a stable voltage profile, indicating that the binder effectively retained Mn^{2+} ions within the electrode and minimized its loss into the electrolyte. Additionally, the practical effectiveness of this binder was demonstrated in thick MnO$_2$ electrodes with a mass loading of 13.3 mg cm^{-2}, where the HPC-based cells retained 97% of their initial capacity after 50 cycles (Fig. 12i). The HPC binder highlights how combining hydrophilicity, metal-ion coordination, and fluorine-free chemistry enables uniform electrochemical reactions and durable cycling even in ultrathick cathodes.

Recent studies have begun to explore various binder modification strategies to enable thick cathode designs in AZIBs. Compared with the extensive research on anodes and electrolytes in AZIB systems, however, binder development remains relatively underexplored. To achieve practical high-energy-density AZIBs, more systematic investigations into binder design are urgently needed. Several important challenges remain to be addressed in future binder research. First, the binder and conductive material content in AZIB electrodes is significantly higher than in LIBs, largely due to the poor intrinsic conductivity of common cathode materials. This often necessitates excessive use of binder and conductive additives, which reduces the proportion of active materials. Therefore, it is essential to develop binders that can provide strong binding strength even at low contents, thereby ensuring sufficient electrochemical stability despite reduced binder loading in the electrode. In parallel, research on multifunctional conductive binders, similar to those actively studied in LIBs, should be pursued to reduce not only the binder content but also the amount of conductive additives in the electrode by providing both adhesion and electronic conductivity. Additionally, further efforts are required to design binders with tailored functional groups that enhance compatibility with conductive additives such as CNTs for thick electrodes. Practical strategies for incorporating these functionalized binders into electrode formulations will be essential for advancing the performance of thick, high-loading AZIB cathodes.

5.3 Engineering strategies involving host and CCs for thick cathodes

Enhancing binder adhesion and constructing thick electrodes are key strategies to minimize inactive regions in cathodes and achieve high energy density as discussed above. However, the intrinsically poor electronic conductivity of most cathode active materials limits these approaches. Even if thick electrodes are successfully fabricated, the proportion of conductive additives in the slurry cannot be significantly reduced, and in some cases, the electrochemical performance of thick electrodes may still fall short compared with their thin counterparts, despite sufficient conductive agent content.[246] Therefore, this section summarizes various approaches beyond binder optimization, including CC modification and electrode structural engineering, that have been explored to enable thick cathodes. These strategies aim to address the limitations of charge transport and maximize the electrochemical utilization of active materials in thick-electrode configurations.

One notable example is the work by Chen *et al.*, who developed a high-mass-loading MnO$_2$ cathode by constructing potassium-ion-stabilized α-MnO$_2$ nanowire forests (K$_{0.133}$MnO$_2$, KMO NWs) directly on carbon cloth using a seed-assisted hydrothermal approach (Fig. 13a).[247] The vertically aligned nanowire architecture provided continuous electron pathways and open ion diffusion channels, effectively overcoming the charge transport limitations typical of thick MnO$_2$ electrodes. In aqueous Zn‖KMO NWs batteries, the vertically aligned nanowire electrode design enabled a high areal capacity of 3.5 mAh cm^{-2} and stable long-term cycling, maintaining 79.2% of its capacity after 1000 cycles, as demonstrated in Fig. 13b. Importantly, the results were achieved without com-
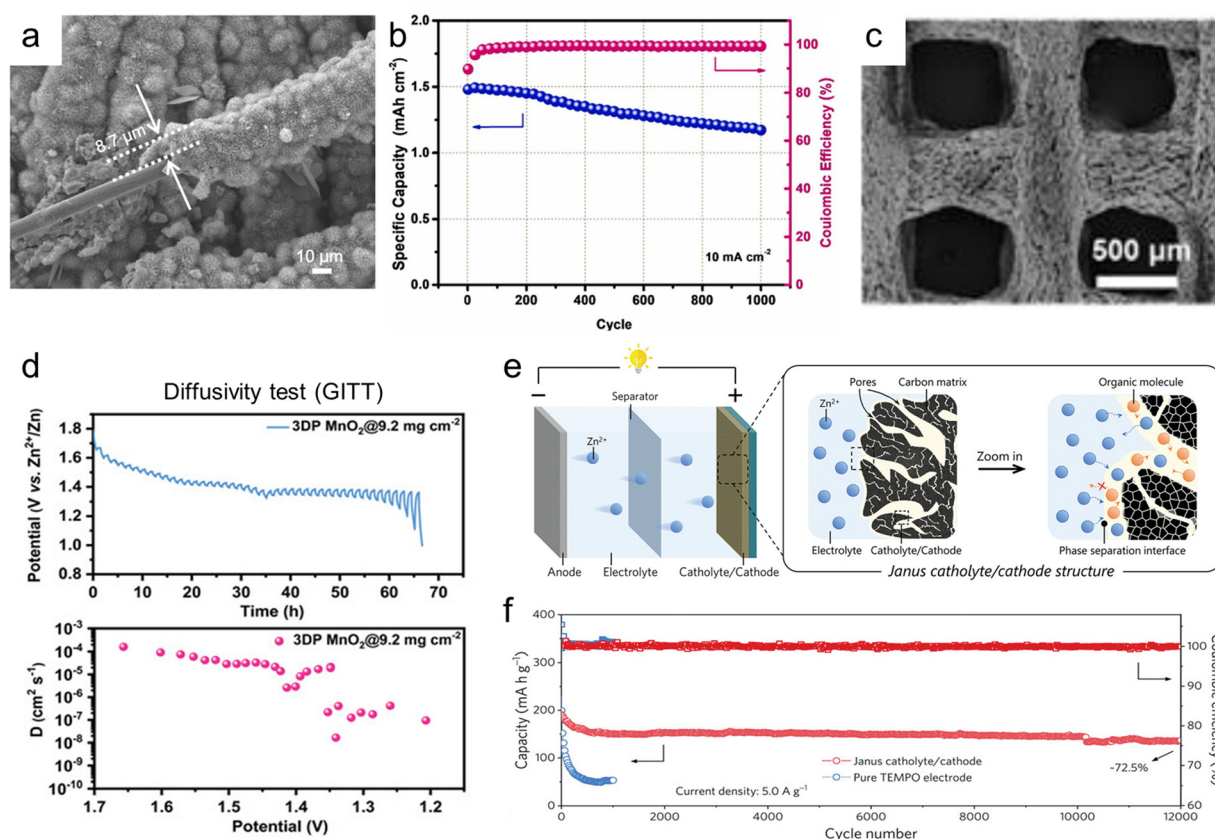
Fig. 13 Electrode-level energy enhancement *via* architecture strategies for thick cathode design. (a) SEM images of KMO NWs. (b) Cycling perform-ance of the Zn‖KMO NWs battery at a current density of 10 mA cm⁻². Reproduced with permission from ref. 247. Copyright 2024, Elsevier. (c) Top-view SEM images of 3DP CMs. (d) GITT profiles and corresponding D values in 3DP MnO_2 electrode at MnO_2 mass loading of 9.2 mg cm⁻² during discharging process. Reproduced with permission from ref. 248. Copyright 2023, Wiley-VCH. (e) Schematic illustration of the working mechanism for rechargeable Zn‖Janus catholyte/cathode cell. (f) Long-term cycling performances and coulombic efficiencies at current densities of 5.0 A g⁻¹ of Janus catholyte/cathode and pure TEMPO electrode. Reproduced with permission from ref. 249. Copyright 2024, Wiley-VCH.

promising rate capability, which underscores the critical role played by the nanowire forest structure in ensuring uniform reaction kinetics across the entire thickness of the electrode.

While conceptually similar to the previous study, which aimed to integrate conductive scaffolds with MnO_2 for thick-electrode design, this work introduced here employs a distinct fabrication approach. Unlike the prior hydrothermal growth of MnO_2 directly on CNT networks, Wu's group utilized electro-chemical deposition to load MnO_2 onto 3D-printed carbon microlattices (3DP CMs) composed of graphene and CNTs (Fig. 13c).[248] 3DP CMs featured a highly conductive, defect-rich, and defect-engineered carbon framework, consequently facilitating uniform MnO_2 deposition with strong interfacial adhesion and reduced overpotentials. 3DP MnO_2 electrodes also featured periodic porous architecture that optimizes elec-tron and ion pathways and surface reactivity, even in high loading cathode. This can be further explained by GITT ana-lysis; as presented in Fig. 13d, 3DP CMs exhibited superior ion diffusion coefficients (10^{-4} to 10^{-8} cm² s⁻¹), attributed to their interconnected porous architecture that facilitates rapid ion transport. This enabled an ultrahigh active material loading of

28.4 mg cm⁻² while maintaining a gravimetric capacity of 283 mAh g⁻¹. The enhanced performance arises from the synergistic effects of defect-induced MnO_2 binding, efficient electron transport within the 3D framework, and facilitated ion diffusion through the ordered porous structure. The two studies underscore the importance of current collector engin-eering in reconciling the trade-off between mass loading and electrochemical performance for practical AZIBs.

The following study features a unique concept and pro-perties that differ from those discussed earlier. This study introduced a new electrode and catholyte configuration to amplify the charge-storage capability, called a Janus catholyte/cathode structure.[249] The unique structure was developed by Zhi's group for aqueous Zn-organic batteries, where redox-active 2,2,6,6-tetramethylpiperidine-1-oxyl (TEMPO) molecules were dissolved in an ionic liquid (EMT-IL) catholyte and con-fined within an activated carbon cathode (Fig. 13e). The acti-vated carbon served as a porous host, physically confining the liquid-phase catholyte within its structure while providing elec-tronic conductivity. This dual-phase structure prevented TEMPO dissolution into the aqueous $ZnSO_4$ electrolyte

through stable liquid–liquid phase separation. The TEMPO-based catholyte mediated a reversible two-electron redox process, substantially enhancing the charge-storage capacity relative to conventional organic electrodes that predominantly operate *via* single-electron transfer pathways. The proposed two-electron transfer allowed for a higher specific capacity of the catholyte phase, and this was one of the key factors enabling the system to achieve an energy density of 425 Wh kg^{-1}. Additionally, the underlying unique mechanism can be further explained as follows. The ionic liquid environment stabilized the reactive intermediates ($TEMPO^+$ and $TEMPO^-$), suppressing side reactions and promoting long-term reversibility. Zn^{2+} ions efficiently migrated across the organic/aqueous interface through a well-tuned solvation structure, where Zn^{2+} coordinated with $TFSI^-$ and TEMPO in the organic phase. This ensured continuous charge balance during the cycle and minimized interfacial resistance. Finally, as shown in Fig. 13f, this system delivered excellent long-term durability, with 72.5% capacity retention over 12 000 cycles at 5 A g^{-1}, and this result underscores its electrochemical resilience under extended cycling and demanding high-rate operating conditions.

Innovative approaches such as 3D porous carbon frameworks, printed microlattices, and chemically modified substrates have successfully improved the structural and mechanical stability of thick electrodes, enabling high mass loading and elevated cycle-life reliability. These works highlight the critical role played by host and CC engineering in overcoming the limitations of thick electrodes. To further maintain mechanical resilience under stress, it is essential to use host and CC materials that provide strong interfacial adhesion with the cathode active materials. During repeated cycles, cathode active materials can experience structural changes or volume fluctuations due to phase transitions and the insertion/extraction of water molecules or ions. Therefore, hosts must offer sufficient mechanical support to maintain electrode integrity under these dynamic conditions. Among recent strategies, coating conductive agents like CNTs with manganese or other active materials has proved effective in maintaining sufficient conductivity even at high mass loading conditions. However, increasing the amount of CNTs inevitably adds to the electrochemically inactive fraction of the electrode in terms of weight and volume. Therefore, while using hosts or 3D current collectors to support thick cathodes is beneficial, it is equally important to pursue approaches that minimize the weight and volume of inactive components, enabling comparable electrochemical performance with less material. Future host and CC designs should aim to achieve this balance, maximizing practical energy density without compromising conductivity or mechanical stability.

6. Novel separator design

While separators serve as physical barriers that prevent direct contact between electrodes, they simultaneously allow ion transport and are essential for sustaining cell operation.[250]

Unlike electrode materials that directly participate in electrochemical reactions, separators do not enhance energy density through electrochemical contribution. Similarly, in contrast to electrolytes that can be engineered to improve voltage stability and thereby increase energy density, separator design does not offer comparable benefits through electrochemical tuning. Nevertheless, since total energy density must reflect the volume and mass of the entire system, separators account for a substantial portion of the cell architecture. Therefore, optimizing separator design remains a valid and necessary strategy for improving the overall energy density of AZIBs.

Conventional polyolefin-based separators used in LIBs, such as polyethylene and polypropylene, are porous polymer membranes with a typical thickness of around 20 μm. Polyolefin membranes exhibit excellent mechanical strength and chemical stability, making polyolefin-based separators well suited for nonaqueous battery systems.[251,252] However, poor wettability with aqueous electrolytes severely restricts the use of these membranes in AZIBs, where efficient Zn^{2+} and H^+ transport is required. Consequently, hydrophilic membranes with superior aqueous affinity like glass fiber (GF) are widely adopted as separators in current AZIB systems.

Although GF membranes offer high porosity and enable efficient electrolyte infiltration and ion conduction, their insufficient mechanical robustness and excessive pore volume fail to effectively mitigate the issues associated with dendritic Zn growth during the cycle. To overcome these challenges, numerous studies have reported the incorporation of materials such as inorganic particles, carbon allotropes, functional polymers, and supramolecules into GF membranes to suppress dendrite formation and enhance operational stability.[253–261] For instance, Liu *et al.* coated the surface of a GF separator with aluminosilicate to enhance its mechanical robustness and regulate ion flux, thereby preventing cell failure caused by internal short circuits.[253] In a separate study, Wu *et al.* introduced polyaniline (PANI) onto the GF membrane *via in situ* monomer polymerization to fabricate a multifunctional separator.[260] The PANI layer helps homogenize the electric field, which suppresses irregular morphology evolution on the electrode surface during cycling and promotes uniform, dendrite-free Zn deposition. As a result, both Zn||Zn symmetric cells and Zn||Cu asymmetric cells incorporating the modified separators demonstrated markedly improved electrochemical performance compared with those based on pristine GF membranes.

However, despite the improved cycling performance achieved through surface modification of GF separators, their thickness remains over ten times greater than that of typical LIB separators, and the density is also substantially higher (2.06 mg cm^{-3} for GF and 0.57 mg cm^{-3} for polypropylene), which ultimately undermines both gravimetric and volumetric energy density. As illustrated in Fig. 14a, combining a high-loading cathode (10 mg cm^{-2}) with a thin Zn foil (20 μm) reveals the disproportionate thickness contribution of the separator in AZIB systems designed for improved energy performance. A conventional GF separator with a thickness of
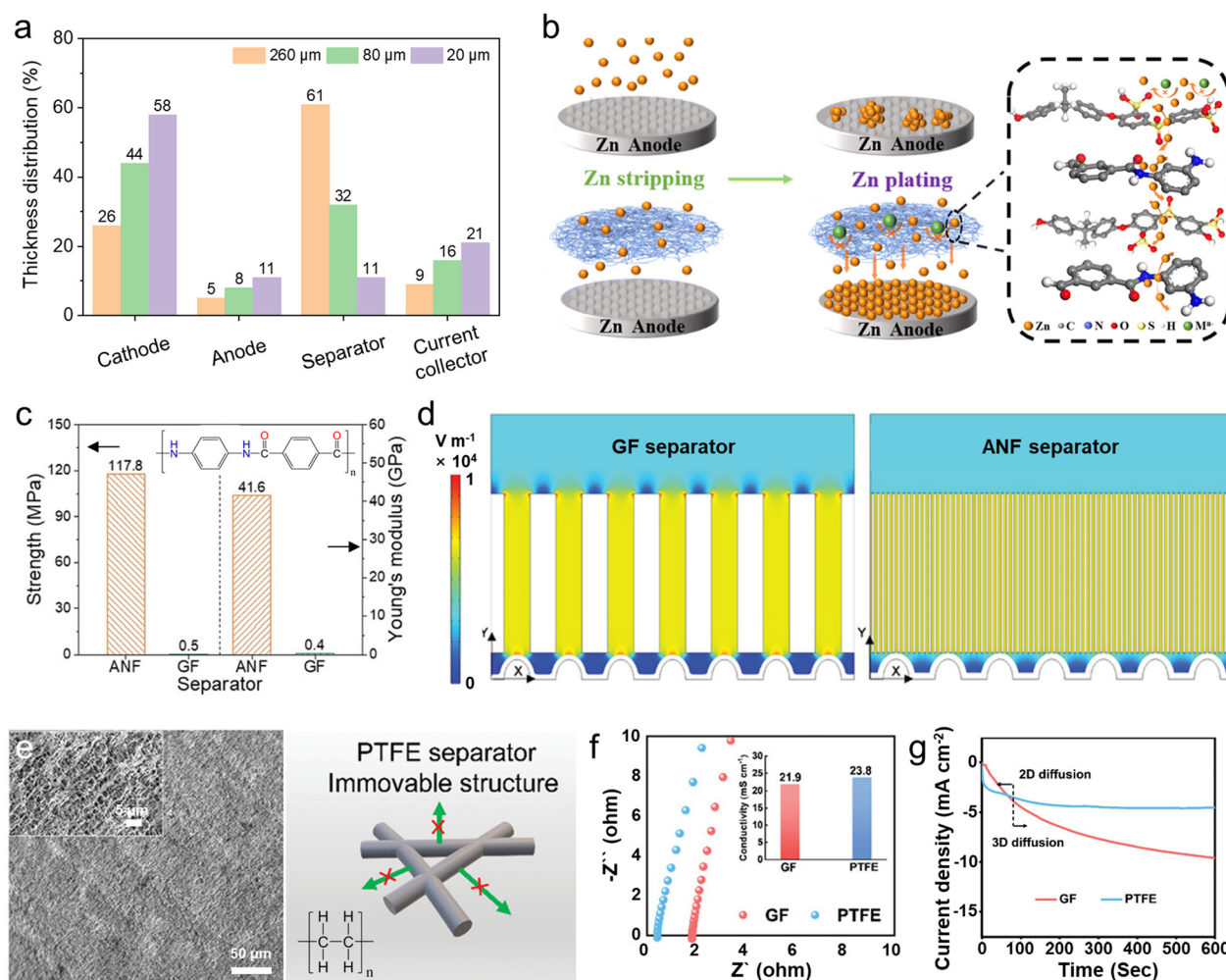
Fig. 14 Separator engineering strategies and electrochemical enhancement enabled by functional polymer membranes. (a) Comparison of the relative thicknesses of AZIB components as a function of separator thickness in the context of high energy density design. (b) Schematic illustration of the ion transport mechanism in AZIBs with the SP separator. Reproduced with permission from ref. 264. Copyright 2022, The Royal Society of Chemistry. (c) Measured tensile strength and Young's modulus of the ANF separator and the GF separator. Inset shows the chemical structure of aramid fiber. (d) Finite element analysis simulation of electric field distributions in cells employing GF and ANF separators. Reproduced with permission from ref. 265. Copyright 2024, Wiley-VCH. (e) SEM micrograph and schematic structure of PTFE separator. (f) Ionic conductivity of GF and PTFE separators. (g) CA curves of Zn||Cu cells with the GF and PTFE separators. Reproduced with permission from ref. 266, Copyright 2024, Wiley-VCH.

260 μm accounts for 60.5% of the total cell thickness, dominating the overall volume composition and limiting the achievable energy density. Reducing the separator thickness to 80 μm dramatically improves the thickness ratio, and further reduction to LIB-level thickness (20 μm) lowers the separator proportion to only 10.5%. In addition, thicker separators require greater electrolyte uptake, which not only increases fabrication cost but also decreases the gravimetric energy density.[262] Moreover, the use of thinner separators improves electrochemical performance through reduced internal resistance and enhanced ion transport, reinforcing the importance of separator miniaturization in advanced AZIBs.[263]

An ideal separator for AZIBs must satisfy the following requirements: (1) minimal thickness to reduce inactive components and increase overall energy density, (2) chemical and electrochemical stability under cell operating conditions, (3) excellent wettability with aqueous electrolytes to ensure smooth ion transport, (4) strong mechanical integrity to prevent internal short circuits triggered by Zn dendrite penetration, and (5) economic and environmental friendliness to minimize waste generation and reduce material cost. However, meeting the above design requirements is particularly challenging due to the intrinsic limitations of the metallic Zn anode. Notably, the irregular and vertically oriented growth of Zn during the cycle often leads to dendrite formation that readily punctures the separator and induces internal short circuits. Consequently, ensuring cell stability while reducing separator thickness remains a key technical hurdle, and this risk continues to limit the practical deployment of thin separators in AZIB systems. For instance, Hu *et al.* developed a nanofiber-

based separator (referred to as SP) by combining poly(*m*-phenylene dicarboxamide) (PMIA) with sulfonated polysulfone (SPSF), aiming to enable selective ion guidance (Fig. 14b).[264] PMIA, known for its excellent mechanical and electrochemical stability, also exhibits strong electrolyte affinity. In particular, the amide groups abundantly present in PMIA serve as hydrogen bonding sites that promote ion transport. Meanwhile, SPSF is a low-cost polymer that provides sulfonate functional groups capable of coordinating Zn^{2+}, thereby contributing to improved anode reversibility. From a structural standpoint, the SP membrane is more than three times thinner than commercial GF separators with a pore diameter ranging from 50 to 200 nm. Despite its thinness, SPSF maintains high mechanical strength, which helps suppress internal short circuits caused by dendrite formation. The membrane consists of a heterogeneous fiber network composed of coarser SPSF fibers and finer PMIA fibers, a structure that enhances electrolyte affinity while simultaneously generating more ion transport channels. Moreover, under aqueous electrolyte conditions, the combined electrostatic interactions of sulfonate and amide groups promote the selective passage of Zn^{2+} and induce uniform metal deposition. As a result, the Zn^{2+} transference number measured using a stainless steel symmetric cell assembled with the SP separator reached 0.74.

Yang *et al.* developed an ultrathin aramid nanofiber (ANF) separator with a thickness of only 5 μm, designed to promote ordered Zn deposition.[265] The ANF membrane features an interwoven network architecture enriched with nanoscale pores, in sharp contrast to conventional GF separators composed of isolated rigid fiber strands that offer limited mechanical durability. Owing to its distinct interwoven structure, the ANF membrane demonstrates high tensile strength and a superior Young's modulus, providing robust resistance to internal short circuits (Fig. 14c). The aramid repeating units possess high polarity, allowing for simultaneous interactions with both cations and anions dissolved in the electrolyte. This dual interaction facilitates Zn^{2+} transfer while suppressing the migration of OTf^-, and thus increases the Zn^{2+} transference number. Specifically, the carbonyl groups in aramid with partial negative charges interact electrostatically with Zn^{2+} and integrate into the solvation shell to transform the local solvation environment into $[Zn(ANF)(H_2O)_5]^{2+}$. The resulting solvation structure improves ion conduction along the membrane and lowers the desolvation energy barrier, accelerating Zn^{2+} transport kinetics. The NH functional groups bearing partial positive charges also participate in electrostatic interactions with OTf^- by anchoring them near the membrane surface and suppressing interfacial polarization. Finite element analysis (FEA) simulations further validated the cooperative effects of ion selectivity and nanoconfinement, revealing that uniformly distributed nanochannels and aligned Zn^{2+} flux help to mitigate the tip effect and reduce electric field inhomogeneity near the anode interface (Fig. 14d). Interestingly, the ANF separator also influenced the crystallographic orientation of Zn deposition. The highest interfacial energy was measured toward the Zn (100) facet, while the weakest interaction occurred at the

(002) facet. Consequently, the energy difference slowed Zn growth along the (002) direction and promoted exposure of the (002) plane, which suppressed dendrite formation and enabled stable anode operation at 80% DOD.

Meanwhile, Yoo's group suggested that beyond material composition and surface energy, engineering membrane microstructures can also produce highly hydrophilic separators.[266] They utilized a PTFE membrane with uniformly distributed nanoscale pores as the separator. Although PTFE is intrinsically hydrophobic due to its high fluorine content and the associated weak intermolecular forces, the authors found that capillary effects induced by the membrane microstructure significantly increased wettability toward aqueous electrolytes. The microstructure-driven improvement also enabled high ionic conductivity, as confirmed by electrolyte contact angle measurements and EIS analysis. In addition, the PTFE membrane exhibits a non-fibrous and mechanically robust framework. As illustrated in Fig. 14e, this immovable porous structure not only reinforces mechanical durability but also blocks Zn from depositing within the internal channels. Theoretically, strong external pressure can restrict Zn surface diffusion by imposing mechanical constraints and suppress dendrite formation. In this context, the enhanced mechanical resilience and immovable pore structure of the PTFE membrane play a key role in regulating vertical Zn growth and preventing dendrite-induced short circuits. Building on these structural advantages, the PTFE-based cell demonstrated lower Zn deposition barriers and faster reaction kinetics (Fig. 14f). Furthermore, CA curves presented in Fig. 14g show rapid current density stabilization in PTFE-based Zn||Cu asymmetric cells. During prolonged Zn deposition, the membrane continued to suppress out-of-plane Zn growth and maintained a smooth surface profile, indicating that two-dimensional diffusion was inhibited without noticeable surface roughening.

Meanwhile, conventional separators exhibit slow degradation rates and raise environmental concerns during both manufacturing and disposal.[267,268] In contrast, separators derived from biomass sources offer improved environmental compatibility and facilitate waste management owing to their inherent degradability.[269,270] Among various biomass materials, cellulose stands out as a particularly promising separator candidate for AZIBs, owing to its strong wettability with aqueous electrolytes, high thermal and electrochemical stability, and excellent biocompatibility and nontoxicity.[271] As an organic compound abundantly found in biomass, cellulose also offers natural degradability, aligning with the goals of environmental sustainability.[272] Zheng *et al.* fabricated a silver nanowire (AgNW)-modified bacterial cellulose (BC) separator *via* a vacuum filtration method.[273] The resulting separator features a Janus-faced architecture, with one side composed of a pure BC layer and the opposite side formed by an AgNW/BC composite. This Janus separator, with a thickness of 29 μm, exhibits excellent electrolyte wettability and ion transport capability, which led to improved rate performance. In detail, the BC layer contains abundant hydroxyl groups that enhance wettability toward aqueous electrolytes, while strong intra-

molecular hydrogen bonding between fibrils contributes to mechanical robustness. In terms of AgNWs, the AgNWs incorporated into the Janus structure help to homogenize the distribution of electric field and further reinforce mechanical strength. In addition, AgNWs and other zincophilic materials serve as ion pumps that facilitate Zn^{2+} diffusion and regulate nucleation behavior, which enables stable anode utilization without dendritic growth. Although the nanofibrous cellulose network enables stable ion conduction and charge transfer due to its favorable structural properties and excellent electrolyte wettability, it suffers from swelling and deformation under aqueous electrolyte conditions, which limits the separator from achieving its designed performance.[274] To overcome this issue and improve electrochemical performance, a Zr–O coated cellulose nanofiber (CNF) separator, denoted as Zr-

CNF, was recently proposed.[275] The authors employed a simple hydrolysis-precipitation method to fabricate a thin Zr^{4+}-coordinated CNF membrane, where Zr^{4+} ions react with carboxylated cellulose to form a cross-linked nanocellulose network during synthesis. Zeta potential measurements revealed that coordination with Zr^{4+} resulted in a more positively charge surface compared with untreated CNF, suggesting the successful formation of Zr–O bonds within the CNF matrix along with a reduction in hydrogen bonding sites. SEM images obtained after immersing the separators in $ZnSO_4$ electrolyte for 3 days revealed that the layer structure of CNF without Zr^{4+} coordination (TCNF) became unevenly loosened due to swelling, whereas the Zr-CNF separator retained its thickness and morphology, clearly demonstrating its anti-swelling property (Fig. 15a). Swelling of the separator not only causes structural
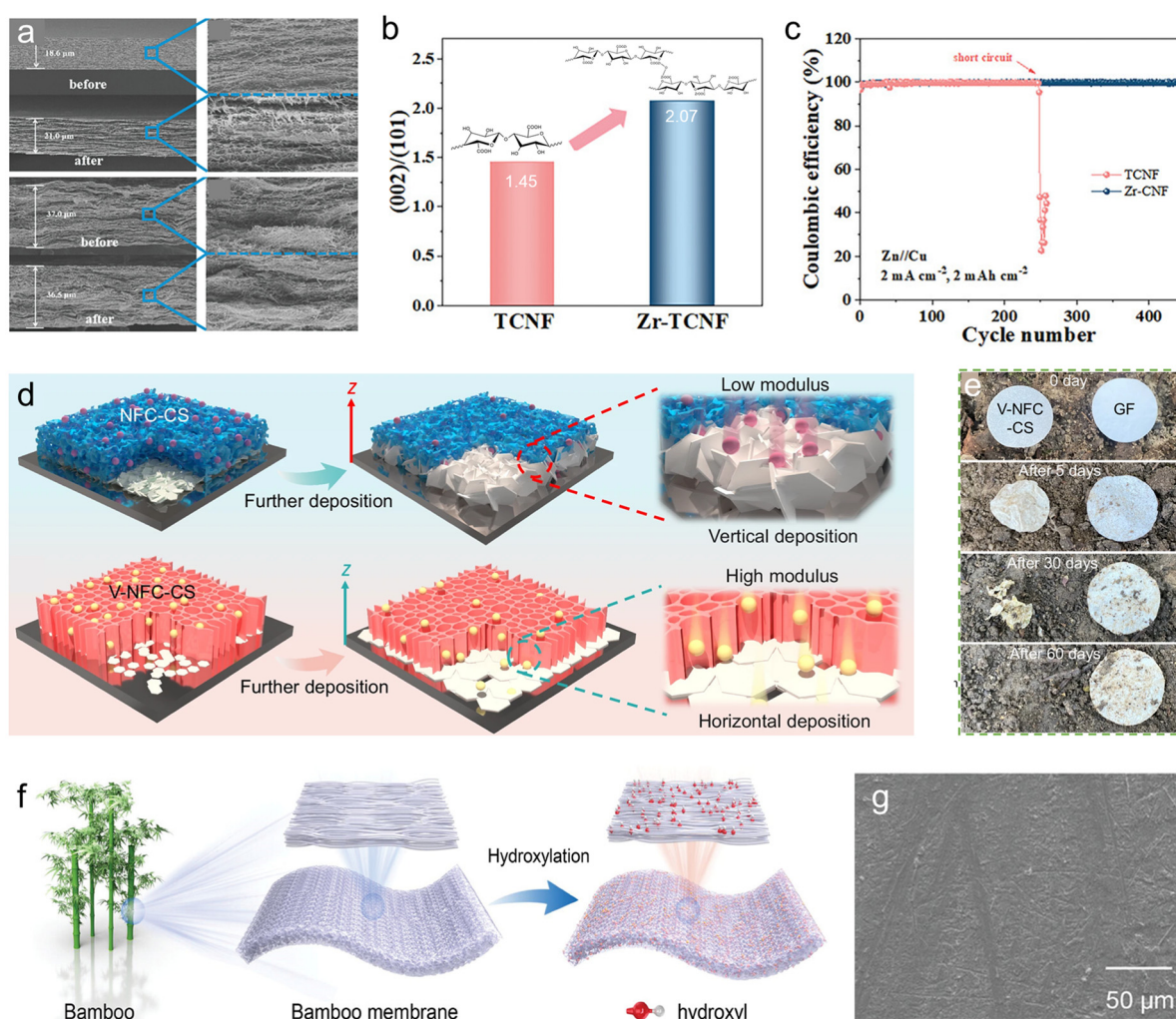

Fig. 15 Eco-friendly separators based on biomass materials for improved electrochemical performance. (a) Cross-sectional SEM images of TCNF (top) and Zr-CNF (bottom) separators before and after electrolyte soaking. (b) Ionic conductivity comparison of TCNF and Zr-CNF separators. (c) Coulombic efficiencies of Zn‖Cu half cells using the Zr-CNF separator at 2 mA cm^{-2} and 2 mAh cm^{-2}. Reproduced with permission from ref. 275. Copyright 2023, Wiley-VCH. (d) Schematic illustration of Zn plating behaviors with NFC-CS (top) and V-NFC-CS (bottom) separators. (e) Photographs of V-NFC-CS and GF separators after soil burial for varying durations. Reproduced with permission from ref. 276. Copyright 2025, Springer Nature. (f) Schematic diagram of the preparation process for the BM separator. (g) SEM image of the Zn anode after 50 cycles at 1 mA cm^{-2} using the BM separator. Reproduced with permission from ref. 277. Copyright 2024, Wiley-VCH.

deformation but also obstructs ion transport pathways, which significantly hampers ionic conduction. The anti-swelling behavior observed in Zr-CNF thus suggests that stable ion conduction can be maintained even under aqueous electrolyte conditions. On one hand, the Zr-based coating layer shields hydrogen bonding interactions within the cellulose nanofibers, which increases porosity and inhibits water molecules from penetrating the internal structure and inducing swelling-related deformation. On the other hand, the dielectric Zr–O layer contributes to electric field homogenization and promotes aligned ion transfer, directing Zn growth along the (002) plane (Fig. 15b). Due to the stable porous structure and uniform electric field distribution provided by Zr-CNF, Zn||Cu asymmetric cells employing the Zr-CNF separator exhibited a lower nucleation barrier and achieved higher Zn plating/stripping coulombic efficiency compared with those with the reference CNF separator, confirming the effectiveness of separator engineering for performance enhancement (Fig. 15c).

Meanwhile, Ma and co-workers explored a structural strategy for separator design to suppress Zn dendrite growth.[276] Increasing the mechanical modulus is generally considered an effective means of inhibiting dendrite formation, even at reduced thickness. Through a freeze-drying process, the authors fabricated a V-NFC-CS separator composed of nanofibrillated cellulose (NFC) and chitosan, achieving a thickness of only 23 μm along with a high modulus of 7.3 GPa. This enhanced mechanical strength effectively inhibited dendrite growth during electrochemical cycling. The V-NFC-CS membrane possesses vertically aligned channels, and its anisotropic framework not only provides superior mechanical properties but also reduces tortuosity, facilitating rapid ion transport. Nanoindentation results confirmed that the V-NFC-CS separator exhibited higher Young's modulus and hardness along the z-axis compared with the NFC/chitosan composite (NFC-CS) membrane with isotropic structure. Due to its lower modulus, the NFC-CS separator is more prone to uncontrolled Zn deposition and insufficient dendrite suppression, which results in the formation of vertically grown dendrites. In contrast, the vertically aligned ion transport pathways in V-NFC-CS help to mitigate polarization of ion concentration and contribute to the stabilization of Zn deposition (Fig. 15d). In addition, the high modulus along the z-axis, attributed to the anisotropic structure, inhibits vertical Zn growth and instead promotes lateral deposition, leading to a dendrite-free morphology. Beyond electrochemical performance, the environmental sustainability of separators is also of growing concern. Conventional polymer-based separators are often non-degradable and contribute to persistent environmental waste. However, the V-NFC-CS membrane underwent complete decomposition after 60 days in soil, demonstrating its biodegradability and highlighting its potential to reduce environmental impact associated with conventional separators (Fig. 15e).

In addition, Jiang's group developed an eco-friendly ultrathin separator using bamboo, a highly renewable biomass, with the aim of reducing carbon emissions.[277] By subjecting the bamboo membrane (BM) to hydrogen peroxide treatment, oxygen-containing functional groups were successfully grafted onto the surface, resulting in abundant hydrogen bonding sites that modulate the population of free water molecules in the electrolyte (Fig. 15f). Moreover, the BM exhibited strong binding interactions with OTf$^-$, leading to an anion-bound effect that enhanced the Zn^{2+} transference number and facilitated more efficient Zn-ion transport. In aqueous electrolyte systems, electrostatic interactions between the bamboo-based separator and the charge transfer interface promoted a uniform distribution of the electric field, which suppressed the tip effect and the resultant irregular Zn deposition. To visually assess the stabilization of the anode through relaxation of the ion concentration gradient, SEM analysis was conducted after 50 cycles at an areal capacity of 1 mAh cm^{-2}. As shown in Fig. 15g, the electrode surface maintained a flat morphology free of dendrites, which was further corroborated by laser confocal scanning microscopy. From a sustainability standpoint, the BM also demonstrated notable environmental benefits due to its biodegradability. Since the BM separator is primarily composed of cellulose, which can naturally degrade in soil, it was completely decomposed after 30 days of burial, becoming integrated into the soil and contributing to the ecological cycle.

To wrap up, preventing vertical Zn growth at the initial nucleation stage is a critical consideration in the design of separators for AZIBs. Due to the poor compatibility of commercial polyolefin separators with aqueous electrolytes, GF membranes have traditionally been employed. In this context, extensive efforts have focused on enhancing anode stability through the modification of GF with diverse functional materials. However, the inherently large thickness and high mass of GF adversely affect the energy density, leading to growing interest in developing ultrathin separators with improved electrochemical performance. In this regard, numerous functional polymer-based membranes have been proposed, exhibiting enhanced mechanical strength, uniform electric field distribution, and regulated ion transport. These features allow such membranes to achieve superior or comparable performance to GF even at significantly reduced thicknesses. Moreover, biomass-derived separators, particularly those based on cellulose, have gained increasing attention due to their mechanical robustness, biodegradability, and eco-friendly characteristics, positioning them as promising candidates for sustainable AZIB systems. Notably, cellulose-based membranes can simultaneously inherit the electrochemical functionalities of engineered polymers, which supports their potential as next-generation separators for high-energy-density applications. Although various separators have been reported that maintain performance with reduced thickness, further advancements can be expected by addressing several pressing challenges. First, scalability is a pivotal concern in practical applications. While fabrication techniques such as vacuum filtration and freeze-drying are effective at the laboratory scale, they often require high processing costs for large-area production and suffer from low productivity. Therefore, despite
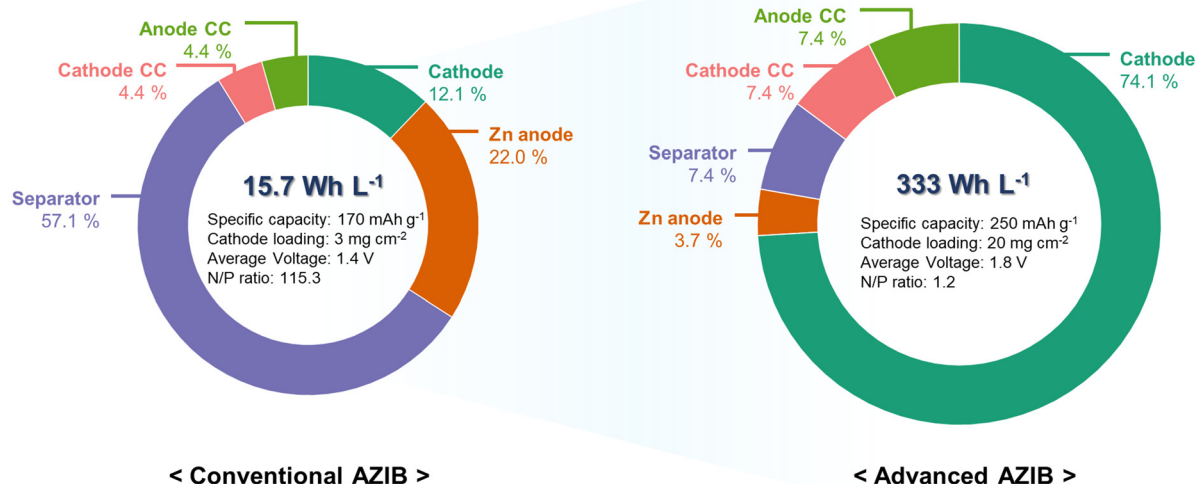
Fig. 16 Comparison of AZIB energy density before and after modification of individual components.

the intrinsic cost competitiveness of the raw materials, to realize economic advantages over conventional separators the field needs scalable and cost-efficient manufacturing strategies. In addition, process complexity should be reduced, since multi-step surface treatments and tight processing windows raise variability and cost in scaled manufacturing. Practical routes should favor simple roll-to-roll-compatible coatings, one-pot chemistries, and in-line quality control for thickness, porosity, and defects to develop commercially available separators. Second, improving the interfacial compatibility between the separator and electrodes represents a key opportunity for performance enhancement. Separators with high affinity toward electrode surfaces facilitate more efficient charge transfer at the interface. More importantly, chemical interactions between the separator and electrode may help to suppress interfacial void formation, which is often exacerbated when pairing with high-capacity cathodes due to gas evolution and irreversible Zn consumption. Addressing these interfacial instabilities could play a vital role in advancing AZIB performance under practical conditions.

7. Conclusion and perspectives

AZIBs have drawn increasing interest as potential replacements for LIBs, supported by their inherent safety, eco-friendly chemistry, and low production cost. However, widespread deployment remains limited due to the relatively low energy density, and closing this gap poses a foundational challenge in advancing next-generation storage technologies. Rather than being determined solely by electrode composition, energy density arises from the interplay of multiple components. A representative comparison of energy density between conventional and fully engineered AZIBs is illus-

trated in Fig. 16, highlighting the substantial gains achievable through system-level optimization.

Typically, aqueous electrolytes exhibit a narrow ESW as a result of severe water decomposition. To suppress gas evolution reactions originating from electrochemical breakdown of water, various modifications have been introduced, including co-solvent blends, molecular additives, and gel-based electrolytes, which aim to regulate solvation dynamics and reduce the activity of uncoordinated water molecules. On the anode side, using excess Zn improves operational lifespan but simultaneously adds electrochemically inactive mass, thereby limiting the attainable energy density. Accordingly, several strategies that promote enhanced anode reversibility and enable deep utilization of Zn foils have been proposed to maintain stable Zn behavior under even extreme conditions. In cathode development, poor binder wettability restricts ion mobility, and the absence of advanced cathode materials further delays progress. Recent studies have explored the use of water-compatible binders to increase loading density and maintain strong contact between active material and electrolyte. Additionally, electrode performance can be elevated by pairing these approaches with high-voltage and capacity-enhanced cathodes. Separator design also remains a significant limiting factor. Currently, GF membranes are typically employed in aqueous battery systems. However, their large thickness and high mass hinder optimized energy density compared with systems incorporating thin, engineered separators. As a result, alternative materials based on multifunctional polymers or bio-derived sources are being investigated to achieve thinner and more sustainable configurations.

The approaches outlined above represent diverse strategies for overcoming the intrinsic energy density limitations of AZIBs. Notably, rather than solely relying on active material optimization to enhance capacity and voltage, addressing

system-level constraints offers a more comprehensive path toward achieving high energy density, which is expected to be a critical step in the development of advanced AZIBs. However, to move beyond material-level improvements and ensure practical viability, additional system-level criteria must also be considered.

1. Although Zn metal foil is currently the most widely adopted anode in AZIBs, exploring alternative systems could further contribute to enhancing energy density. One promising approach is the anode-free configuration, a concept that has been extensively studied in lithium metal batteries, a field that is more mature than AZIB research.[278] Instead of employing metallic Zn or other active anode materials, this strategy utilizes a bare current collector that serves as a host for Zn metal. During cycling, Zn^{2+} are plated onto the substrate in the charge process and subsequently stripped in the discharge process, enabling charge storage without the need for additional anode materials. Such a configuration can exceptionally increase energy density and has therefore garnered attention as a novel direction for next-generation batteries.[279] While anode-free systems offer considerable potential in terms of energy density, ensuring long-term cycling stability remains a critical concern, as the system depends entirely on Zn^{2+} originating from the cathode, without a pre-supplied Zn reservoir. Compared with optimizing conventional Zn metal anodes, implementing anode-free architectures in AZIBs requires more comprehensive efforts across multiple aspects. Most importantly, dendritic Zn growth, already a key issue in traditional Zn anode systems, becomes even more problematic when using standard metal substrates, which lack the ability to regulate Zn nucleation and guide uniform deposition. As a result, the design of substrate materials that facilitate reversible Zn plating and stripping is essential. In addition to substrate engineering, electrolyte design plays a pivotal role in supporting anode-free operation. Electrolytes that promote uniform Zn deposition and maintain interfacial stability are crucial for enabling the practical viability of such systems. Furthermore, the choice of cathode materials must also be reconsidered. Many commonly used cathodes in AZIBs lack pre-intercalated Zn-ions in their pristine state or contain only a limited amount that can be reversibly utilized. Therefore, the development of cathodes capable of delivering sufficient Zn^{2+} reversibility is expected to be another key factor in realizing next-generation anode-free AZIBs.

2. The development of high-mass-loading cathodes is essential for achieving high-energy-density AZIBs. Currently, the conventional wet-processing method, which involves mixing active materials with binders and solvents to form a slurry, is the most commonly employed due to its simplicity. During solvent evaporation, however, the binder and conductive additives tend to migrate toward the electrode surface, which results in weak interfacial adhesion between the current collector and electrode materials and produces nonuniform contact among electrode components.[280] Such microstructural heterogeneity increases internal resistance, impedes charge transport, and degrades electrochemical performance, particularly as electrode thickness increases. In contrast, dry processing, which relies on mechanical mixing followed by roll-to-roll or heat treatment without solvent use, can effectively suppress phase segregation and minimize binder-conductive material decoupling.[281] This method improves interfacial contact and avoids solvent-related issues, thereby enabling stable cycling and extended operational life, even in thick electrode architectures. Moreover, the elimination of solvents offers advantages in terms of cost, safety, and environmental compatibility, which is particularly well aligned with the eco-friendly characteristics of AZIB systems. Nevertheless, suitable binders and optimized protocols for dry-processed electrodes in AZIBs remain insufficiently explored. In particular, PTFE, a commonly adopted binder in dry-processing, often falls short in supporting thick electrodes due to limited electrochemical performance and insufficient mechanical integrity.[282,283] Therefore, developing alternative binders with enhanced electrochemical and mechanical attributes is essential for realizing practical, dry-processed AZIBs with high energy density. Moving beyond functional binders employed in wet-processed systems, future research must address both material innovations and process engineering to establish a scalable and sustainable dry-processing platform for next-generation AZIBs.

3. Recent studies on AZIBs have primarily focused on isolated components, such as high-DOD Zn anodes, high-capacity cathodes, and thin separators. However, realizing practical energy density requires an integrated approach that ensures compatibility across all elements within a cell. Improvements achieved at the material level can be offset by unintended interactions when multiple components are combined. For instance, modified electrolytes may provide high voltage stability, yet they can induce undesirable co-intercalation at the cathode interface, ultimately reducing durability. Additionally, separators optimized for minimal thickness may also exhibit poor compatibility with modified organic-rich electrolytes, which results in incomplete wetting or structural degradation. These mismatches highlight the complexity of interfacial dynamics and underscore the importance of system-level coordination. Moving forward, a holistic design strategy that simultaneously considers electrode architecture, electrolyte formulation, and separator functionality will be essential. A multidisciplinary approach offers a promising pathway to translate component-level advancements into reliable and high-performing AZIBs.

4. Future efforts must continue to explore practical approaches for improving energy density in AZIBs without compromising scalability, cost-effectiveness, or environmental advantages. While strategies involving co-solvents or WiS electrolytes can enhance electrochemical performance, these methods often require large quantities of organic solvents or high salt concentrations, which undermine both economic feasibility and sustainability. Similarly, fabrication techniques such as 3D printing or atomic layer deposition (ALD) introduce process complexity due to equipment limitations and the need for precise nanoscale control, making them difficult to implement on a large scale.[284] Beyond materials and proces-

sing, the use of realistic evaluation metrics is equally important. Rather than focusing exclusively on technical improvements, equal emphasis should be placed on performance assessment criteria. Energy density should not be calculated solely from initial capacity values but should instead reflect stable output over prolonged cycling. In other words, it is essential to evaluate whether the enhanced energy density can be maintained throughout full-cell operation and how long such performance can be sustained during repeated use. At the same time, the resource requirements for constructing high-energy AZIBs must also be considered, including both environmental implications and the complexity of the manufacturing process.

Conflicts of interest

There are no conflicts to declare.

Data availability

No primary research results, software or code have been included and no new data were generated or analysed as part of this review.

Acknowledgements

References

1 S. Wei, R. Sacchi, A. Tukker, S. Suh and B. Steubing, *Energy Environ. Sci.*, 2024, **17**, 2157.

2 J. Zheng, Z. Huang, X. Zhou, B. Scheuer and H. Wang, *Sustain. Cities Soc.*, 2023, **99**, 104976.

3 M. I. Hoffert, *Science*, 2010, **329**, 5997.

4 Y. Wu, W. Shuang, Y. Wang, F. Chen, S. Tang, X.-L. Wu, Z. Bai, L. Yang and J. Zhang, *Electrochem. Energy Rev.*, 2024, **7**, 17.

5 K. Matsumoto, J. Hwang, S. Kaushik, C.-Y. Chen and R. Hagiwara, *Energy Environ. Sci.*, 2019, **12**, 3247.

6 J. Rugolo and M. J. Aziz, *Energy Environ. Sci.*, 2012, **5**, 7151.

7 Z. Hou, L. Zhang, J. Chen, Y. Xiong, X. Zhang and Y. Qian, *Mater. Chem. Front.*, 2021, **5**, 2749.

8 Y. Che, X. Hu, X. Lin, J. Guo and R. Teodorescu, *Energy Environ. Sci.*, 2023, **16**, 338.

9 D. Larcher and J.-M. Tarascon, *Nat. Chem.*, 2015, **7**, 19–29.

10 D. Pulido-Sánchez, I. Capellán-Pérez, C. de Castro and F. Frechoso, *Energy Environ. Sci.*, 2022, **15**, 4872.

11 A. Manthiram, *Nat. Commun.*, 2020, **11**, 1550.

12 T. Kim, W. Song, D.-Y. Son, L. K. Ono and Y. Qi, *J. Mater. Chem. A*, 2019, **7**, 2942.

13 Y. Huang and J. Li, *Adv. Energy Mater.*, 2022, **12**, 2202197.

14 E. A. Olivetti, G. Ceder, G. G. Gaustad and X. Fu, *Joule*, 2017, **1**, 229–243.

15 S. Guan, Q. Peng, X. Guo, Y. Zheng, E. Liao, S. Sun, K. Shin, B. Liu, X. Zhou, C. Zou and Y. Tang, *Chem. Eng. J.*, 2024, **493**, 152864.

16 H. B. Son, M. Shin, W.-J. Song, D.-Y. Han, S. Choi, H. Cha, S. Nam, J. Cho, S. Choi, S. Yoo and S. Park, *Energy Storage Mater.*, 2021, **36**, 355–364.

17 D. Chao, W. Zhou, F. Xie, C. Ye, H. Li, M. Jaroniec and S.-Z. Qiao, *Sci. Adv.*, 2020, **6**, eaba4098.

18 X. Feng, D. Ren and M. Ouyang, *J. Mater. Chem. A*, 2023, **11**, 25236.

19 L.-F. Zhou, T. Du, J.-Y. Li, Y.-S. Wang, H. Gong, Q.-R. Yang, H. Chen, W.-B. Luo and J.-Z. Wang, *Mater. Horiz.*, 2022, **9**, 2722.

20 L. Qin, J. Zhou, M. Sun, X. Yang, X. Shen, C. Yan and T. Qian, *Energy Storage Mater.*, 2025, **74**, 103917.

21 Y. Zhu, G. Liang, X. Cui, X. Liu, H. Zhong, C. Zhi and Y. Yang, *Energy Environ. Sci.*, 2024, **17**, 369.

22 X. Zhou, K. Ma, Q. Zhang, G. Yang and C. Wang, *Nano Res.*, 2022, **15**, 8039–8047.

23 J. Cao, F. Zhao, W. Guan, X. Yang, Q. Zhao, L. Gao, X. Ren, G. Wu and A. Liu, *Small*, 2024, **20**, 202400221.

24 Z. Wang, Z. Ni, J. Chen, Y. Dai, Y. Gao, Q. Zhang, F. Dong, S. Xiong, C. Zhang and J. Feng, *Energy Storage Mater.*, 2025, **75**, 104064.

25 G. R. Pastel, T. P. Pollard, Q. Liu, S. Lavan, Q. Zhu, R. Jiang, L. Ma, J. Connell, O. Borodin, M. A. Schroeder, Z. Zhang and K. Xu, *Joule*, 2024, **8**, 1050–1062.

26 A. Innocenti, D. Bresser, J. Garche and S. Passerini, *Nat. Commun.*, 2024, **15**, 4068.

27 M. Kaya, S. Hussaini and S. Kursunoglu, *Hydrometallurgy*, 2020, **195**, 105362.

28 W. Du, E. H. Ang, Y. Yang, Y. Zhang, M. Ye and C. C. Li, *Energy Environ. Sci.*, 2020, **13**, 3330.

29 Z. Liu, Y. Huang, Y. Huang, Q. Yang, X. Li, Z. Huang and C. Zhi, *Chem. Soc. Rev.*, 2020, **49**, 180.

30 G. Fang, J. Zhou, A. Pan and S. Liang, *ACS Energy Lett.*, 2018, **3**, 2480–2501.

31 C. Nie, G. Wang, D. Wang, M. Wang, X. Gao, Z. Bai, N. Wang, J. Yang, Z. Xing and S. Dou, *Adv. Energy Mater.*, 2023, **13**, 202300606.

32 L. Li, S. Jia, Y. Shi, C. Wang, H. Qiu, Y. Ji, M. Cao and D. Zhang, *Inorg. Chem. Front.*, 2024, **11**, 4485.

33 X. Yu, Z. Li, X. Wu, H. Zhang, Q. Zhao, H. Liang, H. Wang, D. Chao, F. Wang, Y. Qiao, H. Zhou and S.-G. Sun, *Joule*, 2023, **7**, 1145–1175.

34 M. Al-Abbasi, Y. Zhao, H. He, H. Liu, H. Xia, T. Zhu, K. Wang, Z. Xu, H. Wang, W. Zhang, Y. Lai and M. Ge, *Carbon Neutralization*, 2024, **3**, 108–141.

35 M. Wang, Y. Meng, X. Li, J. Qi, A. Li and S. Huang, *Chem. Eng. J.*, 2025, **507**, 160615.

36 X. Guo and G. He, *J. Mater. Chem. A*, 2023, **11**, 11987.

37 W. Feng, Z. Liang, W. Zhou, X. Li, W. Wang, Y. Chi, W. Liu, D. Gengzang, G. Zhang, Q. Chen, P. Wang, W. Chen and S. Zhang, *Dalton Trans.*, 2023, **52**, 7457.

38 M. Wang, Y. Cheng, H. Zhao, J. Gao, J. Li, Y. Wang, J. Qiu, H. Zhang, X. Chen and Y. Wei, *Small*, 2023, **19**, 202302105.

39 N. Wang, H. Wan, J. Duan, X. Wang, L. Tao, J. Zhang and H. Wang, *Mater. Today Adv.*, 2021, **11**, 100149.

40 D. Zhang, L. Miao, Z. Song, X. Zheng, Y. Lv, L. Gan and M. Liu, *Energy Fuels*, 2024, **38**, 12510–12527.

41 Y. Yuan, Z. Li, R. Deng, S. D. Pu, M. Walker, M. Cai, F. Wu, P. G. Bruce and A. W. Robertson, *Energy Environ. Sci.*, 2025, **18**, 5610.

42 S. Liu, R. Zhang, C. Wang, J. Mao, D. Chao, C. Zhang, S. Zhang and Z. Guo, *Angew. Chem.*, 2024, **136**, e202400045.

43 S. W. D. Gourley, R. Brown, B. D. Adams and D. Higgins, *Joule*, 2023, **7**, 1415–1436.

44 R. Borah, F. R. Hughson, J. Johnston and T. Nann, *Mater. Today Adv.*, 2020, **6**, 100046.

45 S. Chen and C. Zhi, *Commun. Chem.*, 2025, **8**, 20.

46 L.-F. Zhou, Y.-J. Gao, T. Du, L.-Y. Liu, Y.-S. Wang, H. Jia and J.-Z. Wang, *Cell Rep. Phys. Sci.*, 2025, **6**, 102565.

47 T. P. Plateau, G. Boyer and J. Park, *Adv. Sci.*, 2025, **12**, 202413444.

48 K. Fu, X. Li, K. Sun, Z. Zhang, H. Yang, L. Gong, G. Qin, D. Hu, T. Li and P. Tan, *Adv. Funct. Mater.*, 2024, **34**, 202409623.

49 C. Hou, L. Du, Y. Li, M. Guo, J. Zhou and S. Qiao, *iScience*, 2023, **26**, 106464.

50 Z. Zhang, T. Zeng, Y. Lai, M. Jia and J. Li, *J. Power Sources*, 2014, **247**, 1–8.

51 B. Deng, X. He, P. Du, W. Zhao, Y. Long, Z. Zhang, H. Liu, K. Huang and H. Wu, *Adv. Sci.*, 2024, **11**, 202408544.

52 D. M. D. Babiker, Z. R. Usha, C. Wan, Y. Zhao, W. Deng, H. Yang, Y. Tan, X. Chen and L. Li, *J. Energy Storage*, 2023, **73**, 108888.

53 J. Y. Kim and D. Y. Lim, *Energies*, 2010, **3**, 866–885.

54 S. Lee, J. Hwang, W.-J. Song and S. Park, *Batteries Supercaps*, 2022, **5**, e202200237.

55 J. Yan, E. H. Ang, Y. Yang, Y. Zhang, M. Ye, W. Du and C. C. Li, *Adv. Funct. Mater.*, 2021, **31**, 2010213.

56 Y. Ran, F. Dong, S. Sun and Y. Lei, *Adv. Energy Mater.*, 2025, DOI: 10.1002/aenm.202406139.

57 D. Selvakumaran, A. Pan, S. Liang and G. Cao, *J. Mater. Chem. A*, 2019, **7**, 18209–18236.

58 A. Kim, Y. Park, J. Choi, S.-H. Yu and K. W. Nam, *ACS Appl. Energy Mater.*, 2025, **8**, 6806–6828.

59 M. J. Alawi, H. Gamal, M. Rashad, M. O. Alziyadi and M. S. Shalaby, *J. Alloys Compd.*, 2025, **1012**, 178455.

60 L. Tang, H. Peng, J. Kang, H. Chen, M. Zhang, Y. Liu, D. H. Kim, Y. Liu and Z. Lin, *Chem. Soc. Rev.*, 2024, **53**, 4877–4925.

61 X. Chen and H. Yu, *ChemElectroChem*, 2024, **11**, e202400444.

62 H. Zhang, X. Liu, H. Li, I. Hasa and S. Passerini, *Angew. Chem., Int. Ed.*, 2021, **60**, 598–616.

63 A. Wang, S. Kadam, H. Li, S. Shi and Y. Qi, *Npj Comput. Mater.*, 2018, **4**, 15.

64 X. Gao, H. Dong, C. J. Carmalt and G. He, *ChemElectroChem*, 2023, **10**, e202300200.

65 R. L. Streng, S. Reiser, A. Senyshyn, S. Wager, J. Sterzinger, P. Schneider, D. Gryc, M. Z. Hussain and A. S. Bandarenka, *Adv. Sci.*, 2025, **12**, 202417587.

66 P. Kulkarni, H. K. Beere, M. Jalalah, M. Alsaiari, R. G. Balakrishna, F. A. Harraz and D. Ghosh, *J. Electroanal. Chem.*, 2022, **924**, 116851.

67 J. Heo, D. Dong, Z. Wang, F. Chen and C. Wang, *Joule*, 2025, **9**, 101844.

68 Z. Li and A. W. Robertson, *Battery Energy*, 2023, **2**, 20220029.

69 S. Chen, R. Lan, J. Humphreys and S. Tao, *Energy Storage Mater.*, 2020, **28**, 205–215.

70 P. Cui, T. Wang, Z. Wang, H. Geng, P. Song, F. Hu, J. You and K. Zhu, *Chem. Eng. J.*, 2024, **500**, 156971.

71 Y. Xie, J. Huang, T. Kong, X. Zhou, K. Wu, X. Liu, J. Yi, L. Xing and Y. Xia, *Energy Storage Mater.*, 2023, **56**, 218–226.

72 S. Bai, Z. Huang, G. Liang, R. Yang, D. Liu, W. Wen, X. Jin, C. Zhi and X. Wang, *Adv. Sci.*, 2024, **11**, 2304549.

73 D. R. Kumar, P. M. Shafi, R. Karthik, G. Dhakal, S.-H. Kim, M. Kim and J.-J. Shim, *J. Mol. Liq.*, 2022, **367**, 120399.

74 C. Zhang, J. Holoubek, X. Wu, A. Daniyar, L. Zhu, C. Chen, D. P. Leonard, I. A. Rodríguez-Pérez, J.-X. Jiang, C. Fang and X. Ji, *Chem. Commun.*, 2018, **54**, 14097.

75 L. Zhang, I. A. Rodríguez-Pérez, H. Jiang, C. Zhang, D. P. Leonard, Q. Guo, W. Wang, S. Han, L. Wang and X. Ji, *Adv. Funct. Mater.*, 2019, **29**, 1902653.

76 H. Jiang, L. Tang, Y. Fu, S. Wang, S. K. Sandstrom, A. M. Scida, G. Li, D. Hoang, J. J. Hong, N.-C. Chiu, K. C. Stylianou, W. F. Stickle, D. Wang, J. Li, P. A. Greaney, C. Fang and X. Ji, *Nat. Sustain.*, 2023, **6**, 806–815.

77 F. Ming, Y. Zhu, G. Huang, A.-H. Emwas, H. Liang, Y. Cui and H. N. Alshareef, *J. Am. Chem. Soc.*, 2022, **144**, 7160–7170.

78 P. Hei, Y. Sai, L. Yu, Y. Lin, B. Li, G. Hu, W. Wu, J. Wang, X. Sun, X.-X. Liu and Y. Song, *J. Am. Chem. Soc.*, 2025, **147**, 27802–27811.

79 Z. Wu, Y. Li, A. Amardeep, Y. Shao, Y. Zhang, J. Zou, L. Wang, J. Xu, D. Kasprzak, E. J. Hansen and J. Liu, *Angew. Chem., Int. Ed.*, 2024, **63**, e202402206.

80 S. Yang, G. Wu, J. Zhang, Y. Guo, K. Xue, Y. Zhang, Y. Zhu, T. Li, X. Zhang and L. Zhou, *Adv. Sci.*, 2024, **11**, 2403513.

81 F. Liu, J. Jiang, G. Li, T. Song, Y. Pei, X. Wang, X. Wu, L. Chen, Q. Deng and B. Long, *J. Energy Storage*, 2024, **99**, 113354.

82 X. Yang, S. Sun and K. Huang, *J. Mater. Inf.*, 2025, **5**, 16.

83 L. Miao, R. Wang, W. Xin, L. Zhang, Y. Geng, H. Peng, Z. Yan, D. Jiang, Z. Qian and Z. Zhu, *Energy Storage Mater.*, 2022, **49**, 445–453.

84 S. Li, Y. Zhong, J. Huang, G. Lai, L. Li, L. Jiang, X. Xu, B. Lu, Y. Liu and J. Zhou, *Energy Environ. Sci.*, 2025, **18**, 2599.

85 Q. Li, D. Luo, Q. Ma, Z. Zheng, S. Li, Y. Xie, L. Xue, M. Lin, Y. Nie, G. Feng, H. Dou, J. Chen, X. Wang and Z. Chen, *Energy Environ. Sci.*, 2024, **18**, 1489.

86 Y. Wang, Z. Wang, W. K. Pang, W. Lie, J. A. Yuwono, G. Liang, S. Liu, A. M. D'Angelo, J. Deng, Y. Fan, K. Davey, B. Li and Z. Guo, *Nat. Commun.*, 2023, **14**, 2720.

87 E. L. Smith, A. P. Abbott and K. S. Ryder, *Chem. Rev.*, 2014, **114**, 11060–11082.

88 B. B. Hansen, S. Spittle, B. Chen, D. Poe, Y. Zhang, J. M. Klein, A. Horton, L. Adhikari, T. Zelovich, B. W. Doherty, B. Gurkan, E. J. Maginn, A. Ragauskas, M. Dadmun, T. A. Zawodzinski, G. A. Baker, M. E. Tuckerman, R. F. Savinell and J. R. Sangoro, *Chem. Rev.*, 2021, **121**, 1232–1285.

89 C. Li, R. Kingsbury, A. S. Thind, A. Shyamsunder, T. T. Fister, R. F. Klie, K. A. Persson and L. F. Nazar, *Nat. Commun.*, 2023, **14**, 3067.

90 Y. Zhong, X. Xie, Z. Zeng, B. Lu, G. Chen and J. Zhou, *Angew. Chem., Int. Ed.*, 2023, **62**, e202310577.

91 R. Chen, C. Zhang, J. Li, Z. Du, F. Guo, W. Zhang, Y. Dai, W. Zong, X. Gao, J. Zhu, Y. Zhao, X. Wang and G. He, *Energy Environ. Sci.*, 2023, **16**, 2540.

92 X. Bai, M. Sun, J. Yang, B. Deng, K. Yang, B. Huang, W. Hu and X. Pu, *Energy Environ. Sci.*, 2024, **17**, 7330.

93 S. Zhang, Y. Sun, X. Zeng, J. Yang, J. Wang and Y. NuLi, *Nano Energy*, 2024, **132**, 110307.

94 J. Shi, L. Zhang, K. Niu, M. Wang, Q. Chen, L. Wen, Y. Ma, J. Su, Z. Li, Y. Yue and Y. Gao, *Adv. Energy Mater.*, 2024, **14**, 2401006.

95 I. C. Pellini, N. Pianta, D. Callegari, G. Conte, R. Lorenzi, C. Simari, M. De Bonis, S. Leonardi, Z. Jusys, J. C. Espinosa-Angeles, D. Bresser, P. Mustarelli and R. Ruffo, *Electrochim. Acta*, 2025, **537**, 146903.

96 Y. Wang, T. Ou, Y. Dong, L. Chen, Y. Huang, D. Sun, W. Qiang, X. Pei, Y. Li and Y. Tan, *Adv. Mater.*, 2024, **36**, 2311009.

97 F. Ding, W. Xu, G. L. Graff, J. Zhang, M. L. Sushko, X. Chen, Y. Shao, M. H. Engelhard, Z. Nie, J. Xiao, X. Liu, P. V. Sushko, J. Liu and J.-G. Zhang, *J. Am. Chem. Soc.*, 2013, **135**, 4450–4456.

98 Y. Lin, Y. Li, Z. Mai, G. Yang and C. Wang, *Adv. Energy Mater.*, 2023, **13**, 2301999.

99 H. Tian, J.-L. Yang, Y. Deng, W. Tang, R. Liu, C. Xu, P. Han and H. J. Fan, *Adv. Energy Mater.*, 2023, **13**, 2202603.

100 C. Huang, X. Zhao, S. Liu, Y. Hao, Q. Tang, A. Hu, Z. Liu and X. Chen, *Adv. Mater.*, 2021, **33**, 2100445.

101 R. Deng, Z. He, F. Chu, J. Lei, Y. Cheng, Y. Zhou and F. Wu, *Nat. Commun.*, 2023, **14**, 4981.

102 W. Chen, Z. Xie, H. Chen and X. Wang, *ACS Appl. Mater. Interfaces*, 2024, **16**, 30580–30588.

103 S. M. Modarresi-Saryazdi, V. Haddadi-Asl and M. Salami-Kalajahi, *J. Biomed. Mater. Res., Part A*, 2018, **106**, 302–348.

104 P. Sun, L. Ma, W. Zhou, M. Qiu, Z. Wang, D. Chao and W. Mai, *Angew. Chem., Int. Ed.*, 2021, **60**, 18247–18255.

105 H. Liu, Z. Xin, B. Cao, Z. Xu, B. Xu, Q. Zhu, J.-L. Yang, B. Zhang and H. J. Fan, *Adv. Funct. Mater.*, 2024, **34**, 2309840.

106 J. Li, Z. Guo, J. Wu, Z. Zheng, Z. Yu, F. She, L. Lai, H. Li, Y. Chen and L. Wei, *Adv. Energy Mater.*, 2023, **13**, 2301743.

107 B. Niu, Z. Li, D. Luo, X. Ma, Q. Yang, Y.-E. Liu, X. Yu, X. He, Y. Qiao and X. Wang, *Energy Environ. Sci.*, 2023, **16**, 1662.

108 J. Yang, C. Weng, P. Sun, Y. Yin, M. Xu, L. Pan and J. Li, *Coord. Chem. Rev.*, 2025, **530**, 216475.

109 I. M. De Cachinho Cordeiro, A. Li, B. Lin, D. X. Ma, L. Xu, A. L.-S. Eh and W. Wang, *Batteries*, 2023, **9**, 343.

110 R. Puttaswamy, Z. Tian, H. Lee, D. Y. Kim, A. Le Mong and D. Kim, *J. Mater. Chem. A*, 2023, **11**, 14075.

111 Y. Wang, Q. Li, H. Hong, S. Yang, R. Zhang, X. Wang, X. Jin, B. Xiong, S. Bai and C. Zhi, *Nat. Commun.*, 2023, **14**, 3890.

112 J. Chattopadhyay, T. S. Pathak and D. M. F. Santos, *Polymers*, 2023, **15**, 3907.

113 E. H. Schacht, *J. Phys.: Conf. Ser.*, 2004, **3**, 22.

114 A. R. C. Salih, H. M. U. Farooqi, H. Amin, P. R. Karn, N. Meghani and S. Nagendran, *Futur. J. Pharm. Sci.*, 2024, **10**, 63.

115 G. Li, Z. Zhao, S. Zhang, L. Sun, M. Li, J. A. Yuwono, J. Mao, J. Hao, J. Vongsvivut, L. Xing, C.-X. Zhao and Z. Guo, *Nat. Commun.*, 2023, **14**, 6526.

116 T. Wei, Y. Ren, Z. Li, X. Zhang, D. Ji and L. Hu, *Chem. Eng. J.*, 2022, **434**, 134646.

117 S. Chen, Y. Chen, X. Mu, P. Wang, L. Miao, S. Tanemura and H. Cai, *Sustainable Mater. Technol.*, 2023, **36**, e00635.

118 Q. Nian, X. Luo, D. Ruan, Y. Li, B.-Q. Xiong, Z. Cui, Z. Wang, Q. Dong, J. Fan, J. Jiang, J. Ma, Z. Ma, D. Wang and X. Ren, *Nat. Commun.*, 2024, **15**, 4303.

119 X. Zhou, T. Ruan, J. Xu, C. Li, S. Huang, J. Zhou, S. Lu, R. Song and R. Li, *RSC Adv.*, 2024, **14**, 23023.

120 P. Wang, B. Sun, X. Wei, L. Yang and H. Wu, *Chem. Eng. J.*, 2023, **455**, 140827.

121 Y. Liu, J. Hu, Q. Lu, M. Hantusch, H. Zhang, Z. Qu, H. Tang, H. Dong, O. G. Schmidt, R. Holze and M. Zhu, *Energy Storage Mater.*, 2022, **47**, 98–104.

122 T. Li, S. Yan, H. Dong, Y. Zheng, K. Ming, Y. Chen, H. Li, G. Li, Z. He, W. Li, Q. Wang, X. Song, J. Liu, E. H. Ang and Y. Wang, *J. Energy Chem.*, 2024, **97**, 1–11.

123 Q. Gao, Z. Chen, J. Feng, X. Zhou, Z. Wan, L. Zhang, H. Gu, L. Sheng, P. Yao, F. R. Wang and Z. Hao, *Green Chem.*, 2025, **27**, 3990.

124 X. Guo, S. Zhang, H. Hong, S. Wang, J. Zhu and C. Zhi, *iScience*, 2025, **28**, 111751.

125 S. Lee, G. Song, S. Kim, D.-Y. Han, J. H. Park, S. Cho, H. B. Son, G. Kim, S. J. Kang and S. Park, *Cell Rep. Phys. Sci.*, 2022, **3**, 101070.

126 L. Yang, Q. Ma, Y. Yin, D. Luo, Y. Shen, H. Dou, N. Zhu, R. Feng, Y. Kong, A. Yu, B. Cheng, X. Wang and Z. Chen, *Nano Energy*, 2023, **117**, 108799.

127 X. Wang, X. Li, H. Fan and L. Ma, *Nanomicro Lett.*, 2022, **14**, 205.

128 Y. Meng, M. Wang, J. Wang, X. Huang, X. Zhou, M. Sajid, Z. Xie, R. Luo, Z. Zhu, Z. Zhang, N. A. Khan, Y. Wang, Z. Li and W. Chen, *Nat. Commun.*, 2024, **15**, 8431.

129 X. Cai, W. Tian, Z. Zhang, Y. Sun, L. Yang, H. Mu, C. Lian and H. Qiu, *Adv. Mater.*, 2024, **36**, 2307727.

130 J. Jang, J. Chun and C. Jo, *Energy Storage Mater.*, 2023, **62**, 102948.

131 Y. Wang, T. Guo, J. Yin, Z. Tian, Y. Ma, Z. Liu, Y. Zhu and H. N. Alshareef, *Adv. Mater.*, 2022, **34**, 2106937.

132 Y. Shi, L. Li, C. Wang, S. Jia, W. Liu, M. Cao, Y. Ji and D. Zhang, *J. Energy Storage*, 2024, **80**, 110101.

133 Y. Wang, H. Sun, N. Li, K. Chen, X. Yang, H. Liu, G. Zheng, J. Liu, Z. Wu, L. Zhai and L. Mi, *ACS Appl. Energy Mater.*, 2022, **5**, 2375–2383.

134 D. Ma, F. Li, K. Ouyang, Q. Chen, J. Zhao, M. Chen, M. Yang, Y. Wang, J. Chen, H. Mi, C. He and P. Zhang, *Nat. Commun.*, 2025, **16**, 4817.

135 J. Yang, R. Zhao, Y. Wang, Y. Bai and C. Wu, *Energy Mater. Adv.*, 2022, **2022**, 9809626.

136 Q. Li, H. Wang, H. Yu, M. Fu, W. Liu, Q. Zhao, S. Huang, L. Zhou, W. Wei, X. Ji, Y. Chen and L. Chen, *Adv. Funct. Mater.*, 2023, **33**, 2303466.

137 K. Zhao, C. Wang, Y. Yu, M. Yan, Q. Wei, P. He, Y. Dong, Z. Zhang, X. Wang and L. Mai, *Adv. Mater. Interfaces*, 2018, **5**, 1800848.

138 Y. Mu, T. Zhou, D. Li, W. Liu, P. Jiang, L. Chen, H. Zhou and G. Ge, *Chem. Eng. J.*, 2022, **430**, 132839.

139 W. Li, Q. Zhang, Z. Yang, H. Ji, T. Wu, H. Wang, Z. Cai, C. Xie, Y. Li and H. Wang, *Small*, 2022, **18**, 2205667.

140 J. Li, H. Liang, Y. Long, X. Yu, J. Li, N. Li, J. Hang, J. Wang and Z. Yang, *J. Energy Chem.*, 2024, **98**, 12–23.

141 J. Li, Z. Kong, X. Liu, B. Zheng, Q. H. Fan, E. Garratt, T. Schuelke, K. Wang, H. Xu and H. Jin, *InfoMat*, 2021, **3**, 1333–1363.

142 L.-L. Zhao, S. Zhao, N. Zhang, P.-F. Wang, Z.-L. Liu, Y. Xie, J. Shu and T.-F. Yi, *Energy Storage Mater.*, 2024, **71**, 103628.

143 Z. Han, C. Zhang, Q. Lin, Y. Zhang, Y. Deng, J. Han, D. Wu, F. Kang, Q.-H. Yang and W. Lv, *Small Methods*, 2021, **5**, 2001035.

144 X. Zhang, C. Li, G. Qu, C. Wang, S. Zhao, T. Wang, N. Li, X. Li and X. Xu, *SmartMat*, 2024, **5**, e1212.

145 H. Gan, J. Wu, R. Li, B. Huang and H. Liu, *Energy Storage Mater.*, 2022, **47**, 602–610.

146 Y. Wang, C. Chen, A. Xu, J. Lv, M. Huang, T. Ren, J. Bai, H. Wang and X. Liu, *Adv. Energy Mater.*, 2025, **15**, 2404071.

147 C. Yang, P. Woottapanit, S. Geng, R. Chanajaree, K. Lolupiman, W. Limphirat, X. Zhang and J. Qin, *ACS Energy Lett.*, 2025, **10**, 337–344.

148 B.-K. Cho, S.-H. Huh, S. H. Kim, S. Yu, J.-S. Bae, J.-K. Yoo and S.-H. Yu, *Carbon Energy*, 2024, **6**, e441.

149 H. Yu, D. Chen, X. Ni, P. Qing, C. Yan, W. Wei, J. Ma, X. Ji, Y. Chen and L. Chen, *Energy Environ. Sci.*, 2023, **16**, 2684.

150 R. Chen, W. Zhang, Q. Huang, C. Guan, W. Zong, Y. Dai, Z. Du, Z. Zhang, J. Li, F. Guo, X. Gao, H. Dong, J. Zhu, X. Wang and G. He, *Nanomicro Lett.*, 2023, **15**, 81.

151 M. Huang, X. Yuan, J. Gan, F. Ji, F. Wang, M. Pan, W. Huang, L. Li and P. Huang, *Int. J. Electrochem. Sci.*, 2022, **17**, 221250.

152 W. Yang, R. Zhu, G. Wu, Y. Yang, H. Yang and E. Yoo, *Energy Storage Mater.*, 2024, **65**, 103153.

153 K. Wang, T. Qiu, L. Lin, X.-X. Liu and X. Sun, *Energy Storage Mater.*, 2023, **54**, 366–373.

154 A. M. Haregewoin, A. S. Wotango and B.-J. Hwang, *Energy Environ. Sci.*, 2016, **9**, 1955.

155 H. Zhang, G. G. Eshetu, X. Judez, C. Li, L. M. Rodriguez-Martínez and M. Armand, *Angew. Chem., Int. Ed.*, 2018, **57**, 15002–15027.

156 M. Kim, S.-J. Shin, J. Lee, Y. Park, Y. Kim, H. Kim and J. W. Choi, *Angew. Chem., Int. Ed.*, 2022, **61**, e202211589.

157 W. Zhang, Y. Dai, R. Chen, Z. Xu, J. Li, W. Zong, H. Li, Z. Li, Z. Zhang, J. Zhu, F. Guo, X. Gao, Z. Du, J. Chen, T. Wang, G. He and I. P. Parkin, *Angew. Chem., Int. Ed.*, 2023, **62**, e202212695.

158 X. Guo, Z. Zhang, J. Li, N. Luo, G.-L. Chai, T. S. Miller, F. Lai, P. Shearing, D. J. L. Brett, D. Han, Z. Weng, G. He and I. P. Parkin, *ACS Energy Lett.*, 2021, **6**, 395–403.

159 S. Yang, K. Xue, J. Zhang, Y. Guo, G. Wu, C. Li, C. Xia, Y. Zhang, Y. Chen and L. Zhou, *Energy Storage Mater.*, 2023, **62**, 102929.

160 P. Wang, X. Xie, Z. Xing, X. Chen, G. Fang, B. Lu, J. Zhou, S. Liang and H. J. Fan, *Adv. Energy Mater.*, 2021, **11**, 2101158.

161 R. Zhao, H. Wang, H. Du, Y. Yang, Z. Gao, L. Qie and Y. Huang, *Nat. Commun.*, 2022, **13**, 3252.

162 J. M. Wang, L. Zhang, C. Zhang and J. Q. Zhang, *J. Power Sources*, 2001, **102**, 139–143.

163 Z. Hu, F. Zhang, F. Wu, H. Wang, A. Zhou, Y. Chen, T. Xue, R. Chen and L. Li, *Energy Environ. Sci.*, 2024, **17**, 4794.

164 A. Bayaguud, X. Luo, Y. Fu and C. Zhu, *ACS Energy Lett.*, 2020, **5**, 3012–3020.

165 Y. Zhou, X. Ni, B. Hao, X. Zhou, C. Yan, J. Zhou and T. Qian, *Energy Storage Mater.*, 2024, **66**, 103227.

166 X. Wei, Y. Mu, J. Chen, Y. Zhou, Y. Chu, L. Yang, C. Huang, T. Xue, L. Zang, C. Yang and L. Zeng, *Energy Storage Mater.*, 2025, **75**, 104026.

167 X. Li, Z. Chen, P. Ruan, X. Hu, B. Lu, X. Yuan, S. Tian and J. Zhou, *Nanoscale*, 2024, **16**, 2923.

168 X. Ren, G. Chen, P. Chang, S. Ju and Y. Wu, *Energy Environ. Sci.*, 2025, **18**, 1867.

169 G. Zeng, Q. Sun, S. Horta, P. R. Martínez-Alanis, P. Wu, J. Li, S. Wang, M. Ibáñez, Y. Tian, L. Ci and A. Cabot, *Energy Environ. Sci.*, 2025, **18**, 1683.

170 L. Wang, H. Shen, W. Sun, T. Zheng, H. Li, J. Yan, L. Ding, Z. Sun, J. Sun and C. Li, *J. Energy Chem.*, 2024, **98**, 114–122.

171 Y. Li, L. Liu, H. Zhang, H. Wang, Z. Sun, Z. Zhang, W. Pang, S. Omanovic, S. Sun, X. Chen and H. Song, *Adv. Funct. Mater.*, 2025, **35**, 2410855.

172 Q. Wu, J. Huang, J. Zhang, S. Yang, Y. Li, F. Luo, Y. You, Y. Li, H. Xie and Y. Chen, *Angew. Chem., Int. Ed.*, 2024, **63**, e202319051.

173 Z. Zheng, X. Zhong, Q. Zhang, M. Zhang, L. Dai, X. Xiao, J. Xu, M. Jiao, B. Wang, H. Li, Y. Jia, R. Mao and G. Zhou, *Nat. Commun.*, 2024, **15**, 753.

174 J. Ji, Z. Zhu, H. Du, X. Qi, J. Yao, H. Wan, H. Wang, L. Qie and Y. Huang, *Adv. Mater.*, 2023, **35**, 2211961.

175 J. Cao, X. Wang, S. Qian, D. Zhang, D. Luo, L. Zhang, J. Qin, X. Zhang, X. Yang and J. Lu, *Adv. Mater.*, 2024, **36**, 2410947.

176 D. Xu, B. Chen, X. Ren, C. Han, Z. Chang, A. Pan and H. Zhou, *Energy Environ. Sci.*, 2023, **17**, 642.

177 X. Zhang, J.-P. Hu, N. Fu, W.-B. Zhou, B. Liu, Q. Deng and X.-W. Wu, *InfoMat*, 2022, **4**, e12306.

178 J. Yang, B. Yin, Y. Sun, H. Pan, W. Sun, B. Jia, S. Zhang and T. Ma, *Nanomicro Lett.*, 2022, **14**, 42.

179 T. Chen, Y. Wang, Y. Yang, F. Huang, M. Zhu, B. T. W. Ang and J. M. Xue, *Adv. Funct. Mater.*, 2021, **31**, 2101607.

180 H. B. Jeong, Y.-W. Kim, G. Kim, D. Mohan, P.-R. Cha and J. Hong, *Small Struct.*, 2025, **6**, 2500111.

181 M. Cui, Y. Xiao, L. Kang, W. Du, Y. Gao, X. Sun, Y. Zhou, X. Li, H. Li, F. Jiang and C. Zhi, *ACS Appl. Energy Mater.*, 2019, **2**, 6490–6496.

182 L. Jiang, Y. Chai, D. Ji, L. Li, L. Li, B. Lu, D. Li and J. Zhou, *Green Energy Environ.*, 2025, **10**, 382–389.

183 X. Xu, S. Li, H. Yan, J. Du, S. Yang and B. Li, *J. Energy Storage*, 2023, **72**, 108625.

184 Y. Hu, Z. Min, G. Zhu, Y. Zhang, Y. Pei, C. Chen, Y. Sun, G. Liang and H.-M. Cheng, *Nat. Commun.*, 2025, **16**, 3255.

185 X. Zhang, C. Qu, X. Zhang, X. Peng, Y. Qiu, Y. Su, J. Zeng, Z. Liu, X. Liu, W. Qi, H. Wang and F. Xu, *Adv. Energy Mater.*, 2024, **14**, 2401139.

186 X. Tian, Q. Zhao, M. Zhou, X. Huang, Y. Sun, X. Duan, L. Zhang, H. Li, D. Su, B. Jia and T. Ma, *Adv. Mater.*, 2024, **36**, 2400237.

187 J. Yin, Y. Wang, Y. Zhu, J. Jin, C. Chen, Y. Yuan, Z. Bayhan, N. Salah, N. A. Alhebshi, W. Zhang, U. Schwingenschlögl and H. N. Alshareef, *Nano Energy*, 2022, **99**, 107331.

188 A. Li, H. Chen, Q. Tian, M. Yang, H. Ma, M. Chen, X. Han, J. Chen, D. Ma and P. Zhang, *Chem. Eng. J.*, 2024, **489**, 151542.

189 M. Liu, W. Yuan, X. Qu, X. Ru, X. Li, T. Wang, X. Wang, Y. Wang, Y. Liu and N. Zhang, *Energy Environ. Sci.*, 2024, **17**, 9611.

190 B. Fu, G. Liu, Y. Zhang, Z. Liu, X. Xie, G. Fang and S. Liang, *ACS Energy Lett.*, 2024, **9**, 3292–3307.

191 Q. Li, N. Li and C. Zhi, *Nano Lett.*, 2024, **24**, 4055–4063.

192 Z. Yang, Q. Zhang, W. Li, C. Xie, T. Wu, C. Hu, Y. Tang and H. Wang, *Angew. Chem., Int. Ed.*, 2023, **62**, e202215306.

193 J. Li, Z. Cheng, Z. Li and Y. Huang, *Mater. Horiz.*, 2023, **10**, 2436.

194 Z. Xu, Y. Li, G. Li, H. Zhang and X. Wang, *Matter*, 2023, **6**, 3075–3086.

195 L. Yan, Q. Zhai, S. Zhang, Z. Li, Q. Kang, X. Gao, C. Jin, T. Liu, T. Ma and Z. Lin, *Adv. Energy Mater.*, 2024, **14**, 2401328.

196 H. Chen, W. Zhang, S. Yi, Z. Su, Z. Zhao, Y. Zhang, B. Niu and D. Long, *Energy Environ. Sci.*, 2024, **17**, 3146.

197 M. Zhang, P. Yu, K. Xiong, Y. Wang, Y. Liu and Y. Liang, *Adv. Mater.*, 2022, **34**, 2200860.

198 W. Du, S. Huang, Y. Zhang, M. Ye and C. C. Li, *Energy Storage Mater.*, 2022, **45**, 465–473.

199 P. Lei, J. Cheng, X. Wang, R. Zheng, J. Zhang, X. Wang, M. Yang and B. Wang, *Nano Energy*, 2025, **141**, 111090.

200 Y. Wu, Y. Zhang, Y. Ma, J. D. Howe, H. Yang, P. Chen, S. Aluri and N. Liu, *Adv. Energy Mater.*, 2018, **8**, 182470.

201 P. Chen, Y. Wu, Y. Zhang, T.-H. Wu, Y. Ma, C. Pelkowski, H. Yang, Y. Zhang, X. Hu and N. Liu, *J. Mater. Chem. A*, 2018, **6**, 21933–21940.

202 Y. Zhang, Y. Wu, W. You, M. Tian, P.-W. Huang, Y. Zhang, Z. Sun, Y. Ma, T. Hao and N. Liu, *Nano Lett.*, 2020, **20**, 4700–4707.

203 J. Chen, X. Geng, C. Wang, X. Hou, H. Wang, Q. Rong, N. Sun, W. Liu, L. Hu, X. Fu, J. Lei, Z. Liu and X. He, *J. Mater. Chem. A*, 2024, **12**, 11038.

204 T. Zhou, L. Zhu, L. Xie, Q. Han, X. Yang, L. Chen, G. Wang and X. Cao, *J. Colloid Interface Sci.*, 2022, **605**, 828–850.

205 X. Ke, L. Li, S. Wang, A. Wang, Z. Jiang, F. R. Wang, C. Kuai and Y. Guo, *Next Energy*, 2024, **2**, 100095.

206 J. Wang, L. Szabo, D. Madhav, I. Ferreira and V. Vandeginste, *Energy Storage Mater.*, 2023, **63**, 103015.

207 M. H. Alfaruqi, J. Gim, S. Kim, J. Song, J. Jo, S. Kim, V. Mathew and J. Kim, *J. Power Sources*, 2015, **288**, 320–327.

208 S. Islam, M. H. Alfaruqi, V. Mathew, J. Song, S. Kim, S. Kim, J. Jo, J. P. Baboo, D. T. Pham, D. Y. Putro, Y.-K. Sun and J. Kim, *J. Mater. Chem. A*, 2017, **5**, 23299.

209 C. Wang, Y. Zeng, X. Xiao, S. Wu, G. Zhong, K. Xu, Z. Wei, W. Su and X. Lu, *J. Energy Chem.*, 2020, **43**, 182–187.

210 Z. Tang, W. Chen, Z. Lyu and Q. Chen, *Energy Mater. Adv.*, 2022, **2022**, 9765710.

211 W. Zhao, Q. Kong, X. Wu, X. An, J. Zhang, X. Liu and W. Yao, *Appl. Surf. Sci.*, 2022, **605**, 154685.

212 J. Li, L. Li, H. Shi, Z. Zhong, X. Niu, P. Zeng, Z. Long, X. Chen, J. Peng, Z. Luo, X. Wang and S. Liang, *ACS Sustainable Chem. Eng.*, 2020, **8**, 10673–10681.

213 W. Yu, Y. Liu, L. Liu, X. Yang, Y. Han and P. Tan, *J. Energy Storage*, 2022, **45**, 103744.

214 M. Chen, S.-C. Zhang, Z.-G. Zou, S.-L. Zhong, W.-Q. Ling, J. Geng, F.-A. Liang, X.-X. Peng, Y. Gao and F.-G. Yu, *Rare Met.*, 2023, **42**, 2868–2905.

215 T. Wei, Q. Li, G. Yang and C. Wang, *J. Mater. Chem. A*, 2018, **6**, 8006.

216 P. Li, L. Shao, P. Wang, X. Zheng, H. Yu, S. Qian, M. Shui, N. Long and J. Shu, *Electrochim. Acta*, 2015, **180**, 120–128.

217 H. K. Razzaq, C.-C. Yang, M. N. Mustafa, A. Numan and M. Khalid, *Prog. Mater. Sci.*, 2025, **151**, 101424.

218 Y. Wang, Q. Li, J. Xiong, L. Yu, Q. Li, Y. Lv, K. K. Abdalla, R. Wang, X. Li, Y. Zhao and X. Sun, *EcoEnergy*, 2024, **2**, 652–678.

219 G. Yang, Q. Li, K. Ma, C. Hong and C. Wang, *J. Mater. Chem. A*, 2020, **8**, 8084.

220 Q. Yang, X. Li, Z. Chen, Z. Huang and C. Zhi, *Acc. Mater. Res.*, 2022, **3**, 78–88.

221 A. M. Ortiz-Ortiz, A. J. Gayle, J. Wang, H. R. Faustyn, D. Penley, C. Sherwood, A. Tuteja and N. P. Dasgupta, *ACS Appl. Eng. Mater.*, 2023, **1**, 1583–1592.

222 F. Wang, K. Xu and C. Wang, *Nat. Sustain.*, 2022, **5**, 818–819.

223 D. Kundu, B. D. Adams, V. Duffort, S. H. Vajargah and L. F. Nazar, *Nat. Energy*, 2016, **1**, 16119.

224 Y. Li, J. Zhao, Q. Hu, T. Hao, H. Cao, X. Huang, Y. Liu, Y. Zhang, D. Lin, Y. Tang and Y. Cai, *Mat. Today Energy*, 2022, **29**, 101095.

225 S. Javed, G. Suo, L. Habib, C. Lin, J. Li, X. Hou, X. Ye, Y. Yang and S. Ding, *J. Energy Storage*, 2025, **118**, 116271.

226 Y. Li, X. Li, M. Xie, X. Liao, X. He, Q. Zheng, K.-H. Lam and D. Lin, *J. Colloid Interface Sci.*, 2025, **696**, 137888.

227 J. Wang, Z. Hu, Y. Qi, C. Han, K. Zhang and W. Li, *J. Mater. Sci. Technol.*, 2025, **221**, 302–320.

228 L.-L. Zhao, Y.-H. Zhao, Y.-M. Wu, P.-F. Wang, Z.-L. Liu, Q.-Y. Zhang, J. Shu and T.-F. Yi, *Energy Storage Mater.*, 2025, **78**, 104299.

229 W. Xu and Y. Wang, *Nanomicro Lett.*, 2019, **11**, 90.

230 Z. Lin, H.-Y. Shi, L. Lin, X. Yang, W. Wu and X. Sun, *Nat. Commun.*, 2021, **12**, 4424.

231 H. Cui, L. Ma, Z. Huang, Z. Chen and C. Zhi, *SmartMat*, 2022, **3**, 565–581.

232 Y. Katsuyama, C. Ooka, R. Zhu, R. Iimura, M. Matsui, R. B. Kaner, I. Honma and H. Kobayashi, *Adv. Funct. Mater.*, 2024, **34**, 2405551.

233 M. Zhang, X. Zhang, Q. Dong, S. Zhang, Z. Xu, Z. Hou and Y. Qian, *Adv. Funct. Mater.*, 2023, **33**, 2213187.

234 G. Yang, Z. Liang, Q. Li, Y. Li, F. Tian and C. Wang, *ACS Energy Lett.*, 2023, **8**, 4085–4095.

235 J. Li and H. Liang, *Energy Mater.*, 2024, **4**, 400033.

236 D. Li, Y. Guo, C. Zhang, X. Chen, W. Zhang, S. Mei and C.-J. Yao, *Nanomicro Lett.*, 2024, **16**, 194.

237 J. Yan, B. Wang, Y. Tang, W. Du, M. Ye, Y. Zhang, Z. Wen, X. Liu and C. C. Li, *Angew. Chem.*, 2024, **136**, e202400121.

238 J. Park, A. M. Houser and S. Zhang, *Adv. Mater.*, 2024, **36**, 2409946.

239 N. Wang, Z. Guo, Z. Ni, J. Xu, X. Qiu, J. Ma, P. Wei and Y. Wang, *Angew. Chem., Int. Ed.*, 2021, **60**, 20826–20832.

240 J. Yoon, J. Lee, H. Kim, J. Kim and H.-J. Jin, *Polymers*, 2024, **16**, 254.

241 Y. Cai, C. Liu, Z. Yu, W. Ma, Q. Jin, R. Du, B. Qian, X. Jin, H. Wu, Q. Zhang and X. Jia, *Adv. Sci.*, 2023, **10**, 2205590.

242 W. Jang, S. Kim, Y. Kang, T. Yim and T.-H. Kim, *Chem. Eng. J.*, 2023, **469**, 143949.

243 X. Feng, X. Gao, X. Zhou, M. Li, H. Ji, Y. Liu, K. Liu, D. Qin, Y. Feng and X. Zhang, *ACS Sustainable Chem. Eng.*, 2025, **13**, 1316–1326.

244 J. Lee, H. Lee, C. Bak, Y. Hong, D. Joung, J. B. Ko, Y. M. Lee and C. Kim, *Nanomicro Lett.*, 2023, **15**, 97.

245 S. Choi, J. K. Seo, H. Park, J. H. Park, S. W. Kim, S. W. Shin, J. A. Bang, K.-N. Jung and B. G. Kim, *Adv. Funct. Mater.*, 2025, **35**, 2417179.

246 K.-Y. Park, J.-W. Park, W. M. Seong, K. Yoon, T.-H. Hwang, K.-H. Ko, J.-H. Han, Y. Jaedong and K. Kang, *J. Power Sources*, 2020, **468**, 228369.

247 Q. Chen, J. Li, C. Liao, W. Liang, X. Lou, Z. Liu, J. Zhang, Y. Tang, L. Mai, L. Zhou and K. Amine, *Nano Energy*, 2024, **126**, 109607.

248 H. Yang, Y. Wan, K. Sun, M. Zhang, C. Wang, Z. He, Q. Li, N. Wang, Y. Zhang, H. Hu and M. Wu, *Adv. Funct. Mater.*, 2023, **33**, 2215076.

249 H. Hong, Y. Wang, Z. Wei, X. Yang, Z. Wu, X. Guo, A. Chen, S. Zhang, S. Wang, Q. Li, S. Li, D. Zhang, Q. Xiong and C. Zhi, *Adv. Mater.*, 2024, **36**, 2410209.

250 B. Niu, D. Luo, X. He and X. Wang, *Chem. – Eur. J.*, 2024, **30**, e202402689.

251 N. Lingappan, W. Lee, S. Passerini and M. Pecht, *Renewable Sustainable Energy Rev.*, 2023, **187**, 113726.

252 S. C. Mun and J. H. Won, *Crystals*, 2021, **11**, 1013.

253 S. Liu, Q. Han, C. He, Z. Xu, P. Huang, L. Cai, H. Chen, H. Zheng, Y. Zhou, M. Wang, H. Tian, W.-Q. Han and H. Ying, *ACS Nano*, 2024, **18**, 25880–25892.

254 S. Liu, C. Hu, L. Yang, H. Ji, F. Peng, J. Zou, Q. Zhang, Y. Tang, H. Wang and Y. Li, *Chem. Commun.*, 2025, **61**, 10391.

255 G. Lin, X. Zhou, L. Liu, H. Li, D. Huang, J. Liu, J. Li and Z. Wei, *RSC Adv.*, 2023, **13**, 6453.

256 B. Wu, P. Wang, H. Yang, Y. Liang, W. Ni, G. Xu, X. Wei and L. Yang, *J. Power Sources*, 2023, **580**, 233323.

257 C. Li, Z. Sun, T. Yang, L. Yu, N. Wei, Z. Tian, J. Cai, J. Lv, Y. Shao, M. H. Rümmeli, J. Sun and Z. Liu, *Adv. Mater.*, 2020, **32**, 2003425.

258 S. Nan, W. Wei, X. Su, Q. Zhang, L. Qian, Y. Dong and R. He, *Chem. Eng. J.*, 2025, **504**, 158634.

259 F. Wu, F. Du, P. Ruan, G. Cai, Y. Chen, X. Yin, L. Ma, R. Yin, W. Shi, W. Liu, J. Zhou and X. Cao, *J. Mater. Chem. A*, 2023, **11**, 11254.

260 H. Zhang, L. Zhang, M. Wang, K. Li, A. Zhang, H. Wang, J. Wu, S. Lin, D. Li, C. Song and X. Guo, *Ind. Eng. Chem. Res.*, 2025, **64**, 4330–4341.

261 T. Liu, J. Hong, J. Wang, Y. Xu and Y. Wang, *Energy Storage Mater.*, 2022, **45**, 1074–1083.

262 G.-L. Zhu, Y.-Y. He, Y.-L. Deng, M. Wang, X.-Y. Liu, L.-P. Wang and J. Gao, *J. Electrochem. Soc.*, 2021, **168**, 110545.

263 J. Ahn, M. Kim, J. Seo, S. Yoon and K. Y. Cho, *J. Power Sources*, 2023, **566**, 232931.

264 W. Hu, J. Ju, Y. Zhang, W. Tan, N. Deng, W. Liu, W. Kang and B. Cheng, *J. Mater. Chem. A*, 2022, **10**, 24761.

265 L. Yang, Y.-J. Zhu, H.-P. Yu, Z.-Y. Wang, L. Cheng, D.-D. Li, J. Tao, G. He and H. Li, *Adv. Energy Mater.*, 2024, **14**, 2401858.

266 G. Wu, R. Zhu, W. Yang, Y. Yang, J. Okagaki, Z. Lu, J. Sun, H. Yang and E. Yoo, *Adv. Funct. Mater.*, 2024, **34**, 2316619.

267 Y. Pan, S. Chou, H. K. Liu and S. X. Dou, *Natl. Sci. Rev.*, 2017, **4**, 917–933.

268 Y. Xia, L. Wang, X. Li, T. Liao, J. Zhai, X. Wang and K. Huo, *Battery Energy*, 2024, **3**, 20240015.

269 T. Zhang, L. Zhang, F. Wang, Y. Wang, T. He, T. Zhang and F. Ran, *J. Energy Storage*, 2024, **101**, 113834.

270 S. Ahankari, D. Lasrado and R. Subramaniam, *Mater. Adv.*, 2022, **3**, 1472.

271 Z. Xue, D. Zhu, M. Shan, H. Wang, J. Zhang, G. Cui, Z. Hu, K. C. Gordon, G. Xu and M. Zhu, *Nano Today*, 2024, **55**, 102175.

272 X. Sun, Y. Zhou, D. Li, K. Zhao, L. Wang, P. Tan, H. Dong, Y. Wang and J. Liang, *Carbon Energy*, 2024, **6**, e539.

273 Z. Zheng, S. Guo, M. Yan, Y. Luo and F. Cao, *Adv. Mater.*, 2023, **35**, 2304667.

274 Y. Xu, Y. Xu, H. Chen, M. Gao, X. Yue and Y. Ni, *Carbohydr. Polym.*, 2022, **294**, 119830.

275 S. Yang, Y. X. Zhang, Y. Zhang, J. Deng, N. Chen, S. Xie, Y. Ma and Z. Wang, *Adv. Funct. Mater.*, 2023, **33**, 2304280.

276 H. Ma, H. Chen, M. Chen, A. Li, X. Han, D. Ma, P. Zhang and J. Chen, *Nat. Commun.*, 2025, **16**, 1014.

277 J. Ma, X. Shi, Z. Wang, L. Zhou, X. Liu, X. Lu and Z. Jiang, *Adv. Mater.*, 2024, **36**, 2406429.

278 S. Huo, L. Wang, B. Su, W. Xue, Y. Wang, H. Zhang, M. Li, J. Qiu, H. Xu and X. He, *Adv. Mater.*, 2024, **36**, 2411757.

279 C.-Y. Park, J. Kim, W.-G. Lim and J. Lee, *Exploration*, 2024, **4**, 20210255.

280 N. Kumano, Y. Yamaguchi, Y. Akimoto, A. Ohshima, H. Nakamura and M. Yamamura, *J. Power Sources*, 2024, **591**, 233883.

281 J. Choi, S. Moon, D. Lee, S. Han, S. Yang, D. S. Jung, J. Joo and P. J. Kim, *Chem. Eng. J.*, 2025, **519**, 165044.

282 S. Han, E.-H. Noh, S. Chae, K. Kwon, J. Lee, J.-S. Woo, S. Park, J. W. Lee, P. J. Kim, T. Song, W.-J. Kwak and J. Choi, *J. Energy Storage*, 2024, **96**, 112693.

283 K.-E. Sung, I. Hwang, J. Choi, S.-K. Jung and J. Yoon, *Chem. Eng. J.*, 2025, **511**, 161789.

284 Y. Feng, R. Tao, K. Livingston, J. Sharma, D. A. Cullen, Y. Lu, W. Steenman, M. Groner, A. Dameron, G. Polizos and J. Li, *J. Energy Storage*, 2024, **100**, 113711.